ABSTRACT OF THE DISSERTATION

Tuning of Spin Dependent Reflection at Ferromagnet/GaAs Interfaces

by

Yan Li

Doctor of Philosophy, Graduate Program in Physics
University of California, Riverside, August 2010
Dr. Roland Kawakami, Chairperson

Semiconductor spintronics aims to integrate memory and logic functions by utilizing the electron's spin degree of freedom in addition to its charge. The building blocks for semiconductor spintronic devices are the ferromagnet (FM)/semiconductor hybrid structures, where the interface plays the key role in spin injection and detection. My graduate research focuses on exploring spin dependent properties of FM/GaAs hybrid structures by ultrafast optics and the tuning of spin polarization through interface modification. In Fe/MgO/GaAs structures, the ultrathin MgO interlayer at the interface causes an unexpected sign reversal in spin dependent reflection, despite being a nonmagnetic insulator. We find that the interfacial bonding with Mg is responsible for the sign reversal. In the Fe_3O_4/GaAs system, we observed oscillatory spin polarization and magneto-optic Kerr effect with respect to Fe_3O_4 film thickness, which we attribute to the formation of spin-polarized quantum well states.

Table of contents

List of Figures

Chapter I

Introduction

Electron spin, discovered in the Stern-Gerlach experiment [1], is one of the fundamental characteristics of electrons. The research area about how to utilize spin degree of freedom in electronics is referred as “spintronics” or “magnetoelectronics” [2, 3]. The scientific achievements in this area have already contributed to our daily lives, and one must have experienced the rapid advancement in computer technology in the last decade, where the hard-disk improvement benefited from the discovery of giant magnetoresistance (GMR) [4, 5]. In early 1990s, the hard-disk information was stored in the magnetization of grains in the disk media and detected by anisotropic magnetoresistance (AMR) effect, which was at the order of 1% [6]. The discovery of the GMR effect increased the density of data storage by more than a hundred fold. The major breakthrough was the use of highly sensitive magnetoresistive read heads. It consists of a sandwich structure: two ferromagnetic layers separated by a non-magnetic layer; one ferromagnetic layer is pinned and the other is free to switch for sensing the magnetic field flux from the recording medium. When the magnetizations of the two layers align parallel, the resistance is low, reading as “0” state; when the two align antiparallel, the resistance of the junction is high, as “1” state. The relative change of the resistance is magnetoresistance (MR), about 30% at room temperature [7]. Later a modified version,

magnetic tunnel junction (MTJ) improved the efficiency even more by replacing the non-magnetic metal with an insulating tunnel barrier, especially MgO [8, 9], and the MR is as high as 600% at RT [10]. Nowadays you can easily get a 3.5” hard disk of 1 TB, with the MgO-based MTJ read head.

The above historical progress of area density of hard disk drive has been relied on the research of metal spintronics [6], mostly dealing with magnetic multilayer systems. This type of device has important applications in memories (e.g. magnetoresistive random access memory), but they do not amplify signals. Spintronic devices made from semiconductors in principle provide access to electrical control of magnetism and spin current, thus multi-functions on a single device. More importantly, they can be easily integrated with traditional semiconductor technology.

1.1 Semiconductor spintronics

Conventional semiconductor devices manipulate charge transport through doping, electrical gate and band offset. A field effect transistor is the basic component for any complicated circuits or devices. With the advancement in semiconductor technology, the size of the transistor is getting smaller, and the switching speed is getting faster. The number of transistors per unit area increases exponentially with time, which is well described by Moore’s law [11]. We can anticipate that there is a limit for miniaturization of the transistors due to quantum tunneling or even more fundamentally, the atomic distance in a semiconductor [11]. So there is a call for new mechanisms of operation, and one promising route is the utilization of electron’s spin degree of freedom in addition to its charge [2, 3, 12, 13].

Introducing spins into semiconductor has the following advantages: (1) The spin coherence time is long with optimal doping, e.g. the spin coherence time in n-GaAs can be as long as 100 ns at low temperature in zero magnetic field [14], in contrast to very shot spin lifetime in metals. (2) Possible electrical control of magnetism and spin.

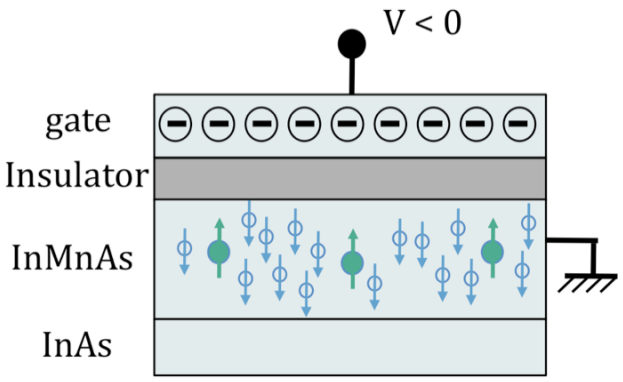

FIG 1.1 Electric field control of hole-mediated magnetism in InMnAs. Under negative gate voltage, the induced hole carriers in InMnAs makes it ferromagnetic; under positive gate voltage, the hole concentration is very low, so the semiconductor is paramagnetic.

Magnetism of ferromagnetic semiconductor is hole concentration mediated, thus could be controlled through gate voltage [15] (FIG 1.1). Spin precession without magnetic field could also be realized based on spin-orbit coupling [16, 17]. (3) Optical means accessible. Coupling of spin and circularly polarized light enables spin dynamics study [14], optical spin injection and manipulation [18], and detection of spins by photoluminescence [19], etc. Semiconductor spintronics aims to combine storage, logic and communication functions on a single chip [12]. The advantages include non-volatile, high speed, and low power consumption.

A prototype spin transistor device was first proposed by Datta and Das [20], and it requires spin injection, manipulation and detection, as shown in FIG 1.2. The conducting

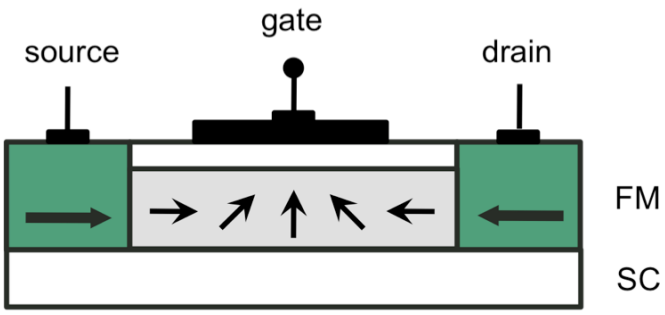

FIG 1.2 Datta-Das spin transistor. The source and drain electrodes are made of ferromagnetic material (green). The source electrode emits spin polarized electrons, then the electrons pass through a 2d electron gas channel (grey) controlled by the gate voltage for spin precession, and finally detected by the drain electrode. Depending on the alignment of spins after reaching the drain, the source-drain current is modulated by the gate voltage.

channel is a 2d electron gas formed at InAlAs/InGaAs interfaces. The geometry is very similar to the conventional MOSFET, but the source and drain electrodes are made of ferromagnetic material, so that the source-drain current depends on the orientation of spins injected and the change of spin orientation during transport. The manipulation is based on Rashba spin-orbit coupling with the control of electrical gate. With the gate voltage on, the electrical field produces an effective magnetic field for the electrons, so the electron spin would precess. Until now, there have been many device proposals [20-23] and vast amount of effort on realizing these devices. Significant progress has been made in spin injection into semiconductors from magnetic metal [19, 24] and diluted

magnetic semiconductors [25, 26]. However, most of the device proposals are still waiting for experimental demonstration, as well as practical circuit and system designs utilizing spin degree of freedom.

1.1.1 Spin injection (creation)

Spin injection (or creation) is the prerequisite for spin transistor device. Although intuitively, one would assume that by driving electrons carriers from ferromagnetic metal to semiconductor would give spin-polarized current, and the ohmic contact work for this purpose. Intensive experimental studies failed in spin injection until 2000, researchers realize the conductivity mismatch problem [27, 28], which is the mismatch between the spin-dependent but low resistance in the FM and much high spin-independent resistance of the semiconductor. Although the spin polarization in FM is high, it reduces to almost zero in the semiconductor. This problem could be solved by inserting a spin dependent tunnel barrier [29, 30], where the spin polarization of the tunneling current depends on the density of states of the FM, or development of ferromagnetic semiconductor [25, 31] to avoid the conductivity mismatch. With this theoretical guide, spin injection from FM into semiconductors have been realized on GaAs [24, 32], Si [33-35], Graphene [36], and etc. Al_2O_3 [33, 34, 37, 38] and MgO [32, 39] are typically chosen as tunnel barrier materials, and MgO has higher spin polarization in resistance than Al_2O_3 [30]. Especially, successful injections into Si and graphene have also been realized at room temperature, more promising for near future application in electronics. As an alternative method for spin creation, spin extraction is an inverse process to spin injection, where electrons flow from semiconductor to FM, leaving a spin imbalance in semiconductor [40, 41].

Ferromagnetic semiconductors are promising spin injectors (and detectors) because of the good resistance matching with the semiconductor channel, and offer the potential to spintronic devices "all in one material". Here I only focus on $III_{1-x}Mn_xAs$ type ferromagnetic semiconductors, which have been studied the most and best understood. Ferromagnetism in semiconductor was first discovered in $In_{1-x}Mn_xAs$ [42] and $Ga_{1-x}Mn_xAs$ [43] by Ohno *et al.* in 1990's. It is generally accepted that substitutional Mn ions provide localized spin and also act as acceptors, and the concentration of holes can mediate the ferromagnetic coupling between two Mn spins [44]. Hybridization between Mn *d* orbitals and valence band orbitals, mainly on neighboring As sites, leads to an antiferromagnetic interaction between the hole spin and the Mn spin. For a simple picture, the RKKY interaction gives ferromagnetic ordering of the Mn spins, mediated by induced spin polarization of itinerant holes [44]. Experimentally, the electrical control of magnetism (Curie temperature and coercivity) has been demonstrated by applying gate voltage to change the hole concentration [15, 45]; light irradiation also changes the magnetic properties of ferromagnetic semiconductor [46]. For practical applications, the Curie temperature (T_C) of the III-V ferromagnetic semiconductor needs to be increased, since it is usually below 200 K [47]. Zener model predicted that T_C in $Ga_{1-x}Mn_xAs$ could be increased by increasing the hole concentration with Mn doping [44], and this prediction stimulated a big effort on increasing T_C [47-49]. It turns out that the more Mn doping is compensated by donors, so the T_C saturates for x > 5% [50]. GaN and ZnO, predicted to have T_C above room temperature [44], have also been widely explored and exhibit T_C above RT [51, 52], as well as Ge [53].

While the key element in semiconductor spintronics is the population imbalance between spin up and spin down electrons, which usually relies on magnetic materials as sources of spin polarization, a completely new frame of generating spin imbalance in semiconductors without magnetic material is based on spin-orbit interaction, i.e. spin hall effect (SHE) [54, 55]. The spin-orbit interaction in a nonmagnetic semiconductor or metal causes spin-asymmetric scattering of conduction electrons through the side jump and skew scattering mechanisms [54]. When a charge current flows in an electric field, the spin-up and spin-down electrons are deflected sideways in the opposite directions, inducing a transverse spin current (SHE); when a spin current flows (spin diffusion through non-local injection or other means), the spin-up and spin-down electrons are deflected in the same direction as they actually move in opposite directions, inducing a net charge current in the transverse direction (inverse SHE). Experimentally, both SHE [56, 57] and inverse SHE [58] have been observed using nonlocal geometry electronic devices in metals. The origin of SHE in metals is generally extrinsic, which is related to impurities and scattering. The bringing up of intrinsic SHE in semiconductors [59] leaded to a hot theoretical debate, because the intrinsic SHE is in principle dissipationless and much larger than extrinsic SHE, but there were issues such as disorder effect. Experiments of detecting SHE is challenging because of the weak signal in most cases. Kato et al. observed spin accumulation in n-GaAs by Kerr rotation imaging [60], Wunderlich et al. observed SHE in p-GaAs by circularly polarized photoluminescence [61]. They attributed the origin of SHE to extrinsic and intrinsic mechanisms, respectively. The experimental studies on spin-Hall insulators (topological insulators),

band insulators with nonzero SHE (e.g. HgTe), are currently at frontiers in condensed matter physics too [62, 63].

1.1.2 Spin manipulation

Spin manipulation or spin transport is the next step after spin injection into semiconductors. Spin precession in magnetic field is a very direct way of manipulation. In a lateral spin valve device, the application of a perpendicular magnetic field causes spin precession so that the spin accumulation at the detector electrode changes as a function of magnetic field, which is also known as the Hanle effect [64, 65]. Spin manipulation electrically has more profound significance in terms of integrated circuits. Spin-orbit coupling is usually the basic principle behind electrical control of spins, and the manipulation could be viewed as an effective magnetic field for electrons.

Spin-orbit coupling is one of the fundamental interactions of electron spin in semiconductors, which is a relativistic effect, as shown in FIG 1.3. The orbital motion of an electron in lab frame transforms to nucleus motion in electron's frame, thus generates a current and a magnetic field according to the Biot-Savart law. In general, any kind of Hamiltonian inversion symmetry breaking gives spin-splitting and an effective magnetic field for electrons. The electrical manipulation of spins works by generating spin-splitting in various ways. There are typically two kinds inversion symmetry breaking considered: structural inversion asymmetry (the Rashbs effect) and bulk inversion asymmetry (Dresselhaus k^3 spin splitting in bulk zinc-blende crystals). The Rashba spin-orbit coupling is described by $H_R = \alpha\vec{\sigma}\bullet(\vec{k}\times\vec{E})$, where $\vec{\sigma}$ is the Pauli operator, $\vec{k}$ is the wavevector (moment) of the electron, and $\vec{E}$ is the electric field built in or applied by

gate voltage, along film growth direction. The Dresselhaus term is $H_{ss} = \hbar\vec{\Omega}(\vec{k})\bullet\vec{\sigma}/2$,

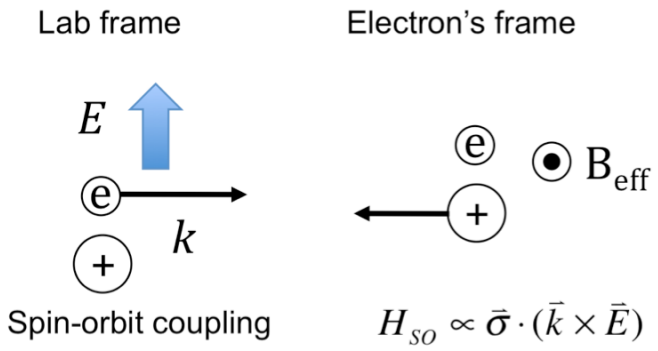

FIG 1.3 Spin-orbit coupling in the view of reference frame change.

where $\vec{\Omega}(\vec{k})$ is the precession vector perpendicular to $\vec{k}$ and with magnitude proportional to k^3. The spin splitting presents only for $\vec{k}$ along the <110> axes (no splitting along <111> or <100> axes). The orientation of $\vec{\Omega}(\vec{k})$ with respect to $\vec{k}$ changes when the direction of $\vec{k}$ changes between [110] and $[1\bar{1}0]$ of the zinc-blende structure semiconductor.

The Datta-Das spin transistor employs the Rashba effect for spin manipulation [20]. As the electrons flow from the injector to the detector, they possess momentum perpendicular to the electric field, so the Rashba effect produces an effective magnetic field, which makes the spins to precess as they pass through the semiconductor channel. When the spins reach the detector electrode (drain), the orientation relative to the magnetization of the detector determines the source-drain current. If they align parallel to the magnetization of the detector, the source-drain current is the maximum; if they align antiparallel to the magnetization of the detector, the source-drain current is the minimum.

So as the gate voltage changes, the strength of the Rashba term changes, and source-drain current oscillates as a function of gate voltage because the spin precession makes the spins reaching the detector alternate between parallel and antiparallel. In fact, full electrical spin field effect transistor with electrical manipulation is not a trivial experiment, only been demonstrated recently [66].

Application of strain can modify both the structural inversion asymmetry term and the bulk inversion asymmetry term. The potential energy gradient resulting from strain gradient along the film normal direction plays the role of electrical field in the Rashba effect. Uniform strain is reflected in the bulk inversion asymmetry term. Ref. [16, 17] presented methods of spin precession without magnetic field in strained GaAs. In the former method, GaAs on AlGaAs without the supporting substrate curves following AlGaAs layer thus get strained when the supporting substrate is etched away, and the author observed spin precession in zero magnetic field detected by time-resolved and spatially-resolved Faraday rotation. The application of perpendicular external field and electric field shifts the resonant amplification peaks (Section 1.2) as like there is an internal magnetic field, which is the source of spin precession in zero field. Crooker et al. applies uniaxial strain along [110] or $[1\bar{1}0]$ on the GaAs sample, and describes the effect of strain by strain Hamiltonian, whose form is similar to the Rashba Hamiltonian for electrons moving in-plane. The strain induced effective magnetic field is linearly proportional to *k*. Strains along <100> axes do not induce spin-orbit coupling.

1.1.3 Spin detection

Spin detection in a device is also crucial. In an electrical device, a commonly used method is the Johnson-Silsbee spin-charge coupling [64]. A ferromagnet electrode in contact with the semiconductor placed outside of the charge current loop detects the spin polarization due to diffusion by the spin dependent electric-chemical potential. It is a process inverse to the spin injection. The nonequilibrium spin population give rises to an electrical current and voltage from the nonmagnetic semiconductor to ferromagnet electrode, where in spin injection an electrical current from ferromagnetic metal to semiconductor gives spin polarization. Because of the geometry, this method is also called non-local spin valve. In contrast, a local spin valve is a two-terminal device and a direct demonstration of spin injection. However, the detection of MR is complicated by anisotropic MR and Hall effects, which contribute to a relatively large background resistance [67]. Complimentary to the non-local four terminal detection and the local two terminal detection, three terminal method is also adopted, where you measure the voltage drop across the injector/semiconductor junction [35, 38, 68]. The requirement of this method is less than the non-local measurement, since no spin transport is required. Apart from the electrical detection, optical means are accessible for direct bandgap semiconductors, and the optical means are highly sensitive and direct measurement. When an electron and a hole combine, a photon is emitted with circular polarization that depends on the spin state of the electron and hole. By measuring the circular polarization of the electroluminescence (EL), the spin polarization of the carriers is determined. When the EL is measured as a function of perpendicular magnetic field, the resulting curve decays with field (Hanle curve) because of spin precession and mixing, and the

Lorentzian lineshape can give information about spin lifetime [69]. The spin polarization accumulation in semiconductor could also be measured and also spatially imaged by Kerr/Faraday rotation measurement [60, 70, 71]. With the optical Kerr rotation technique, spin Hall effect was first observed in semiconductor, spin injection and accumulation were imaged in lateral spin transport devices [70] and in cross section [71], which resolved spin distribution in the semiconductor in depth.

1.1.4 Single spin: the ultimate limit

In addition to the developing of spin transistor scheme, one ambitious goal for semiconductor spintronics is quantum computation with electron spins. Single spins in diamonds [72] and semiconductor quantum dots [73] have been measured and manipulation of single spins by ultrafast optical pulses were also explored [74, 75]. Electron spin coherence time for an ensemble of spins is typically on the order of ns [76, 77], due to inhomogeneous broadening, the intrinsic spin coherence for an individual spin can be quite long, which makes it suitable for quantum computation. The spin-echo technique (i.e. Hahn spin-echo sequence, $(\pi/2) - \pi - (\pi/2)$ rotations) refocuses/restores spin information so that the operation of spins are possible before the information is lost. While in typical semiconductor, such as GaAs, Si, the operation of single spin requires low temperature, nitrogen-vacancy centers in diamond show spin lifetimes exceedingly long at room temperature. There are other advantages of this system: weak spin-orbit coupling, little hyperfine coupling, and fewer lattice vibrations due to the strong bonding of diamond. This single spin regime is also of fundamental interest as truly quantum-mechanical system.

1.2 Spin coherence in semiconductors

A lot of spin dependent phenomena in semiconductor are characterized by spin lifetimes T_1 and T_2, the longitudinal and transverse spin lifetimes, respectively. T_1 is the relaxation time of a state of spin imbalance to equilibrium; T_2 is the relaxation time of phase coherence between two states, as shown in FIG 1.4. The transverse spin coherence time T_2 is direct relevance to coherent spintronic devices, such as spin manipulation,

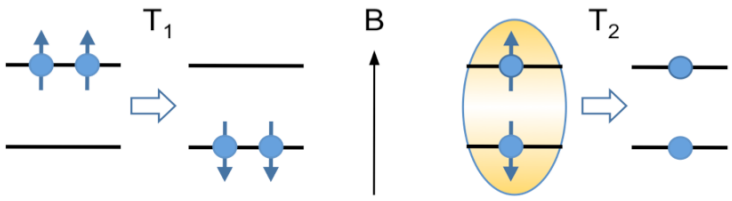

FIG 1.4 Longitudinal and transverse spin lifetimes, T_1 and T_2. The relaxation of nonequilibrium (higher energy) to equilibrium (lower energy) is characterized by T_1. The decay of phase coherence between two spin states is characterized by T_2, and no change in energy is involved.

transport and storage. The aim is to make spin coherence long enough to allow all the operations before the information is lost. In principle, T_2 is the spin coherence time for single spin; in practice, an ensemble of electron spins are easier to measure. For ensemble of spins, the spin decoherence includes inhomogeneous spin precession, so T_2^* is used for transverse spin lifetime.

In direct band gap semiconductors, the spin coherence is measured by the powerful time-resolved Faraday/Kerr rotation spectroscopy [78]. In this measurement, the spins are oriented optically by the pump beam, normal to the applied magnetic field.

The spin state could be viewed as a superposition of spin-up and spin-down states; in a classical picture, the spin precesses about the magnetic field at Larmor frequency determined by the Zeeman splitting energy. The probe beam measures the spin projection along the beam path, the initial spin direction. The decay of spin precession represents the decoherence process. In GaAs, the spin coherence time is as long as 100 ns [14] at an optimal doping and the coherent spin packets can be dragged over hundreds of micrometers [79]. These initial results gave us good hope that the electron spins are promising candidate for future quantum computation. In semiconductor heterostructures and nanostructures, more interesting phenomena arise, e.g. the ferromagnetic imprinting of nuclear spins due to the adjacent ferromagnet layer [80]. A lot of basic physics questions can be studied by optical means in semiconductor, and conclusion can be applied to applications in electronic devices.

1.2.1 Spin coherence in bulk and film semiconductors

The most well studied semiconductor for spin coherence is GaAs. The systematic study of spin lifetime T_2^* (transverse, for ensemble of spins) dependence on doping density in n-type bulk GaAs showed that the optimal doping for longest spin lifetime is ~ $1\times10^{16}/cm^3$, and the according spin lifetime is over 100 ns at 5 K [14]. The spin lifetime is so long that it is longer that the laser pulse repetition time or the typical time delay one can set up in an experiment. In this case, the “resonant spin amplification” technique is especially useful and gives accurate measurement of the spin lifetime. The resonant spin amplification is a result of spin precession from successive pump pulses matching in phase, in an applied magnetic field. So at a fixed time delay, the signal exhibit resonant

peaks as a function of magnetic field, separated evenly. The sharper the resonant peak, the longer the spin lifetime. As a function of carrier density, the spin lifetime increases abruptly at very low doping, exhibit maximum spin lifetime at $n = 1\times10^{16}/cm^3$ (the metal-insulator transition point), and decreases steadily thereafter.

The spin relaxation in the n-GaAs may come from spin-orbit scattering of phonons or impurities (the Elliot-Yafet (EY) mechanism), or precession about random internal magnetic fields (the Dyakanov-Perel (DP) mechanism). For the EY mechanism, the spin relaxation rate is proportional to the momentum scattering rate. For the DP mechanism, the broadening accumulates between two collisions, so the spin relaxation rate is inversely proportional to the momentum scattering rate. The DP mechanism dominates for high doping (n = $1\times10^{18}/cm^3$, $3\times10^{18}/cm^3$[14]), and the spin relaxation has little temperature dependence. The temperature dependent study of T_2^* for the doping of $1\times10^{16}/cm^3$, spin scattering processes in different temperature regimes were identified. In p-type GaAs, the electron-hole spin scattering could play a significant role at low temperatures, which is the Bir-Aronov-Pikus (BAP) mechanism.

The TRFR technique has also been employed to study spin coherence in other semiconductors, ZnSe [81], GaN [82], and ZnO [83]. Spin coherence in these materials persist up to room temperature, despite the fact that there are a lot of defects.

1.2.2 Spin coherence in semiconductor heterostructures

One of the interesting semiconductor heterostructures is the ferromagnet/semiconductor structure, in which ferromagnetic imprinting of nuclear spin [80] and spontaneous spin polarization in semiconductor by ferromagnetic proximity

polarization [84] has been discovered. The effect of the ferromagnet layer here is not the fringe fields or direct exchange interactions, but spin dependent reflection at the FM/semiconductor interface. More about this topic is presented in section 1.3.2.

1.2.3 Spin coherence in quantum dots

As the dimension of the system continues to reduce, in the case of quantum dots, the quantum confinement plays a more significant role in spin coherence. Synthesis of mono dispersed QDs (mainly II-VI group semiconductors) by chemical method has been mastered [85], as well as the self assembly of QDs. The special properties of QDs, such as the size tunable bandgap, localization of carriers, provide new possibilities to spintronics applications. In general, the spin lifetime is much longer than the same condition bulk semiconductor, because the spin scattering mechanisms are reduced when energy levels are highly quantized [86]. Spin dynamics has been measured up to room temperature in chemically synthesized CdSe QDs by Gupta et al. [76, 77]. Multiple precession frequencies were observed as signatures of electron and exciton spins, with different g-factors. The spin relaxation is dominated by inhomogeneous broadening effect from size distribution of the QDs. The spin lifetimes drop dramatically with application of magnetic field.

Single spin in semiconductors is considered the limit for miniaturization of magnetic information storage, and also a solid-state system for quantum computation. QDs, or in combination with gate control, provide an approach to single spin system. The number of carriers could be well characterized by photoluminescence, where the narrow bandwith peaks in PL is the characteristics of single electron charge. Single electron spin

confined in GaAs QDs can be optically initialized, manipulated, and readout [18, 75]. Time-resolved Kerr rotation works on single spin the same way as on bulk and film GaAs, and the only difference is that the focal spot size on the sample is much smaller (~ 1 μm diameter or less), as well as the Kerr rotation signal. In Mikkelsen's work, a third beam is employed for optical tipping by optical Stark effect [87]. An intense circularly polarized pulse creates a magnetic filed along the beam propagation direction, and the magnetic field in the very short time duration turns the orientation of the single spin. The physical system for single spin could also be atomic impurities, such as Mn acceptors in GaAs quantum wells [88] and nitrogen-vacancy color centers in diamond [72].

1.2.4 Spin noise spectroscopy

The above mentioned technique, TRFR, has been extensively utilized to study spin dynamics in semiconductors, and produced a lot of valuable and in-depth results. The pump-probe Faraday rotation [14] and time-resolved photoluminescence spectroscopy [89], are both commonly encountered as very successful optical techniques. In both methods, optical excitation drives the system away from equilibrium and then the time evolution is detected, which can be viewed as perturbative. In contrast, spin noise spectroscopy is a non-perturbative technique that measures the stochastic spin orientation of carriers in equilibrium with off resonance Faraday rotation (energy below bandgap) [90]. For a system of non-interacting spins, like lightly n-doped GaAs, the spin fluctuation scales with $\sqrt{N}$ (N is the number of spins), even in zero magnetic field. In a static magnetic field, the precession of the random spin fluctuation displays in spin noise

spectrum as a magnetic resonance peak, which yields information about g-factor and spin dynamics.

This technique has superior advantages over the traditional pump-probe method, because it reveals the real spin lifetime without perturbation. Optical excitation inevitably creates hot carriers and holes. The creation of hot carriers is perturbing at very low temperatures, because the carrier cooling becomes very slow. In addition, the excited free electrons can disturb the spin dynamics of localized carriers. The creation of holes is also perturbing since holes lead to spin relaxation by the Bir-Aronov-Pikus (BAP) mechanism. The BAP mechanism is especially strong at low temperatures and cannot be corrected easily. In pump-probe Faraday rotation measurement, the electron spin dynamics can in principle be probed after the photo-excited holes have recombined. In practice, this is usually not true since the radiative life time of holes becomes very long for low hole densities. The spin noise spectroscopy has been applied to study alkali atomic gases [90], bulk GaAs [91, 92], GaAs quantum wells [93], and InGaAs quantum dots assembly [94]. As the spectrum analyzing technique has advanced, the probed volume, from gases to QDs, has shrunk significantly. In the quantum-mechanical limit of single spin, the spin noise measurement would provide access to new physics of single spin interaction with environment, intrinsic spin dynamics excluding the inhomogeneous broadening effect.

1.3 Ferromagnet/semiconductor heterostructures for spintronics

As I showed earlier, ferromagnet/semiconductor heterostructures are the building blocks for semiconductor spintronics. They serve as spin injector and detector in a typical spin transistor [20], and could also be electrical gate for spin manipulation [21, 22]. The

most important semiconductor systems in application are GaAs (AlGaAs) and Si, in which there has been significant progress towards spintronic devices in the last ten years. In this mix, graphene is a zero gap semiconductor and spin injection into graphene has also been realized.

1.3.1 Spin injection into semiconductors from ferromagnetic metals

The conductivity mismatch is the major issue for spin injection from ferromagnetic metals to semiconductors [27]. Theoretical model by several groups treated this issue and provided solution [28, 29]: a spin-dependent interfacial barrier between the FM and the semiconductor. Two criteria must be satisfied: (1) The interfacial barrier is spin selective. (2) The interfacial resistance dominates in the FM/tunnel barrier/semiconductor heterostructures. A tunnel barrier could be realized either by tailoring the naturally formed Schottky barrier or simply incorporating an insulating material, such as Al_2O_3, in the structure. In the following paragraphs, we explicitly explain application of both methods in spin injection into GaAs and Si.

GaAs was the earliest material studied for spin injection. Theoretical work showed that the Fe/GaAs heterostructures are perfect for spin injection because of the matching symmetries and energies for majority spin bands [95, 96], ignoring the fact that the band bending extends into GaAs for ~ 100 nm. In the real system, the spin polarization was found to be significantly dropped due to disorder, so the effort was focused on engineering the interfacial barrier, including Schottky barrier and discrete insulating barrier. However, the symmetry matching is important and works experimentally for Fe/MgO tunnel barrier.

The detection of spin injection in GaAs employs electroluminescence (a light-emitting diode structure) mostly in the early stage. The optical polarization of the emitted light ($P_{\text{circ}} = \frac{I(\sigma+) - I(\sigma-)}{I(\sigma+) + I(\sigma-)}$) directly relates to the spin polarization of the electrons ($P_{\text{spin}} = \frac{n_{\uparrow} - n_{\downarrow}}{n_{\uparrow} + n_{\downarrow}}$) before recombination, based on the selection rules. For a bulk-like recombination region, $P_{\text{spin}} = 2P_{\text{circ}}$; in a quantum well, the degeneracy of light and heavy hole bands is lifted, only the heavy hole states participate, thus $P_{\text{spin}} = P_{\text{circ}}$ [97]. Together with the Hanle effect, spin lifetimes are also determined. The measurement geometry could be surface emitting or edge emitting, depending on the orientation of the injected electron spins. The Faraday geometry with surface emitting is usually performed for analysis of heavy hole exciton in a quantum well. Edge-emission geometry is also used for analyzing the light hole exciton in a quantum well, or the heavy hole exciton in a bulk-like recombination region. One important factor that affects the measured P_{circ} is the radiative lifetime τ_{r}. If the spin lifetime is much longer than τ_{r}, the effect is negligible, but this is not the case. The initial carrier spin polarization P_0 right after entering the region of recombination is related to both lifetimes by $P_0 = P_{\text{spin}}(1 + \tau_{\text{r}} / \tau_{\text{s}})$ [69], for the case of QW. In addition, propagation of light through the FM layer induces circular polarization due to the magnetic circular dichroism [37], so this effect should be excluded in analysis.

Spin injection into GaAs has been done using both tailored Schottky barrier [19, 24, 68], and insulating Al_2O_3 [37, 38, 98] and MgO [32] barriers. The first work

demonstrated spin injection in Fe/GaAs (2%) was through Schottky barrier tunneling, and did not engineer the barrier shape [99]. The depletion width of a naturally formed Schottky barrier depends on the doping concentration of the semiconductor, which is generally too large for tunneling spin injection. For example, the depletion width is on the order of 100 nm for n-type doping of $10^{17}/cm^{-3}$ (see simulation in Section 2.4.2), and 40 nm for n ~ $10^{18}/cm^{-3}$ in GaAs. By gradient doping, the Schottky barrier width is tailored for minimized depletion width while keeping the doping of semiconductor channel region low for long spin lifetimes. Specifically, heavily doped surface region reduces the depletion width significantly, and the gradient doping profile avoids the dip after the Schottky barrier. This approach has been successful in achieving large electrical spin injection from Fe epitaxial layer into GaAs (or AlGaAs), detected by EL, and non-local spin valve method. Work by Hanbicki et al. realized spin injection into AlGaAs/GaAs, detected by EL, with a spin polarization of 32% [19]. The current-voltage characteristics were examined to assure that the dominant transport mechanism is tunneling, using the Rowell criteria. Work by Lou et al. demonstrated full electrical spin injection, transport and detection in a lateral geometry, detected by the non-local spin valve [24]. Non-local spin accumulation, together with the Hanle effect, demonstrated spin injection and transport unambiguously. The bias voltage dependence of non-local voltage showed a sign change, and Kerr rotation measurement gave the same result. Crooker et al. also observed the mysterious sign reversal of spin accumulation in the lateral spin valve device [70]. This sign change was later explained by Dery et al. with bounded state at the interface in spin extraction scheme [41], and by Chantis et al. with the model of

interfacial resonant states [100]. Crooker et al. also showed that the sensitivity of the Fe/GaAs detector with Schottky tunnel barrier has strong bias dependence (voltage across the detector Fe/GaAs junction), and even sign change [101]. More importantly, the temperature of growth and annealing affect the interfacial atomic structure, thus the spin injection and transport efficiency, as shown in Ref. [102, 103].

Insulating barrier provides a rectangular potential barrier and introduce an additional interface. It is important to make the barrier layer flat, pinhole-free to achieve tunneling, and as a benefit it works as a spin filter because of spin-dependent barrier resistance. Several groups showed successful spin injection into GaAs with Al_2O_3 tunnel barrier [37, 98, 104]. van't Erve et al. achieved spin injection of 40% from Fe to AlGaAs at 5 K. The electrical efficiency is not as good as using Schottky tunnel barrier, and this problem should be alleviated by the same surface doping of reducing the Schottky barrier thickness. Following the big success of MgO based tunnel junction [9], MgO tunnel barrier was also found to improve the spin injection efficiency in Fe/MgO/GaAs heterostructures [32]. However, the improvement is not as dramatic as in the tunnel junction. All these spin injection has been determined by luminescence. The spin polarization in injection drops as the temperature increases. Because of the extra interface of insulator/GaAs, it introduces complexity in the tunneling process too. The $Fe/Al_2O_3/GaAs$ involves amorphous oxide layer and polycrystalline Fe film. Tran et al. [38] proposed in their measurement, in $Co/Al_2O_3/GaAs$, an intermediate tunneling step through some localized states at the oxide/GaAs interface should account for observed bias dependence in three-terminal, voltage across the injector junction measurement.

The successful spin injection into Si started 2007. Methods of spin injection include hot electron transport [33], tunneling spin injection [34, 35, 39]. In Appelbaum's work, hot electron transport contributes to the observed spin valve effect (85 K), where both the spin injection and detection utilizes hot electron states in ferromagnets for filtering. The hot electrons are injected from Al through Al_2O_3 barrier to CoFe for spin filtering. The spin polarized hot electrons transport through the thick Si, and the polarization of the conduction electrons in Si is detected by a second hot electron spin filtering electrode, by measuring the collection current. Obvious spin valve signal was observed and spin precession up to 3π in transverse magnetic field were detected. The drawback of this method is the low electrical efficiency. With a large emitter current (~ mA), only small fraction of it (~ nA) contributes to the hot electron spin polarized current and gets detected as the collection current. At about the same time, spin injection through $Fe/Al_2O_3/Si$ was also showed to work by detection of electroluminescence in n-i-p Si heterostructures, and the spin polarization of injection was estimated to be ~30% at 5 K. The EL process in Si is phonon assisted, so the phonons carry away some spin angular momentum of the initial injected electrons, thus the EL measurement underestimates the injected electron spin polarization. And another factor affects the measured circular polarization of luminescence is the very long radiative lifetime in indirect bandgap semiconductors. The radiative lifetime τ_r is much longer than the spin lifetime, so the measured circularly polarization is again lower than the real injected spin polarization. However, the indirect bandgap of Si and complicity of analysis restrict the application of EL for spin polarization detection.

Dash et al. [35] achieved spin injection into Si with NiFe/Al_2O_3/Si tunneling contact at room temperature, detected with three terminal method, the injector and the detector electrode are the same one. Hanle curves were measured from low temperature to room temperature. Low work function material Cs was used to lower the Schottky barrier height, and results are compared to those without Cs. With Cs (no Schottky barrier, the spin injection has less temperature dependence than the spin injection through Al_2O_3 and Schottky barrier without Cs, which shows a big increase at low temperature. The spin lifetime increases at low temperature for spin injection with Cs, and decreases for spin injection without Cs. The author proposed that the temperature dependence of tunneling spin injection through Al_2O_3 and Schottky barrier is due to the two-step tunneling mechanism, and the intermediate states are probably localized states at oxide/Si interface. Removing the Schottky barrier with Cs makes the interface directly couple to the bulk Si. They also observed hole spin injection/accumulation using p-Si. The spin lifetime is similar to that of electrons. One thing to note is that the three-terminal detection does not require spin transport. Sasaki et al. [39] demonstrated spin injection with Fe/MgO/Si tunneling contact and transport by the non-local spin valve up to 120 K. The authors claimed that the device was very robust that injection current dependence of non-local voltage does not change after a large injection current (2.5 mA, 2.5×21 μm contact area) was applied.

Furthermore, successful spin injection into carbon nanotubes and graphene has also been realized [36]. Because of the low spin-orbit coupling and hyperfine interactions, the spin lifetime is expected to be long in carbon-based materials. Special properties of

graphene, such as high mobility, gate tunable carrier concentration and type, makes it attractive for electronics, including spintronic applications. Tombros et al. demonstrated spin injection through Al_2O_3 tunnel barrier and spin transport in single layer graphene at room temperature, in both electron and hole transport region, controlled with electrical gate. Following this work, more aspects have been explored, including anisotropic spin relaxation [105], spin drift effects [106], and bias dependence of spin injection [107, 108].

1.3.2 Ferromagnetic proximity polarization, spin extraction

While the FM/semiconductor structures were originally developed for spin injection [19, 99], the discovery of ferromagnetic proximity polarization (FPP) through ultrafast optical experiments [80, 84] has motivated theoretical proposals for novel devices that exploit spin-dependent reflection [21, 22]. Subsequent studies on biased FM/SC structures have directly measured spin accumulation arising from spin-dependent

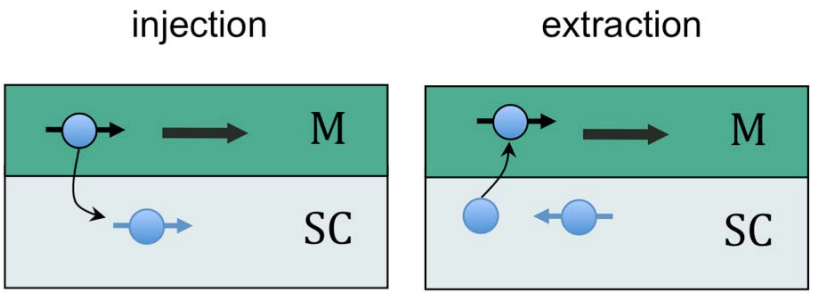

FIG 1.5 Spin injection and extraction. Injection: the carriers flow from ferromagnetic metal to semiconductor, and spin polarized carriers are injected into the semiconductor. Extraction: carriers flow from semiconductor to ferromagnetic metal, and leave a spin imbalance in the semiconductor.

reflection [70, 109]. FIG 1.5 shows the comparison of spin injection and spin extraction. In spin extraction, the electrons, which would participate in the spin transport, are

restricted in the semiconductor.

In Kawakami et al.'s work [80], the nuclear spins of GaAs are found to be aligned with the magnetization of GaMnAs (or MnAs) in GaMnAs(MnAs)/GaAs heterostructures. The spin precession frequency in the FM/GaAs heterostructure differs from that of the bare GaAs, the reference sample. The difference is due to an effective magnetic filed generated by nuclear spins via hyperfine interaction. Explicitly, the precession frequency is $\nu_L = \frac{g\mu_B}{h}(B_{\text{app}} + B_{\text{n}})$, where the B_{n} is the extra magnetic field from the nuclear spins. Nuclear field B_{n} scales with $\langle I \rangle$, the average nuclear spins. In the time-resolved Faraday rotation measurement, the spin precession frequency changes over time (starting at the sample is exposed to the laser irradiation), and it saturates in ~20 min. In steady state, the average nuclear spin was estimated to be 13%. The direct evidence for the nuclear spin polarization in GaAs was the all-optical nuclear magnetic resonance data, where the isotopes of Ga and As peaks were identified. Strong dependence of B_{n} on the pump intensity and temperature is the characteristics of dynamic nuclear polarization (DNP).

Following the above mentioned work, Epstein et al. [84] found that the nuclear spins are from DNP by the spontaneous (< 50 ps) electron spin polarization in the FM/GaAs heterostructures, and the ferromagnetic imprinting of nuclear spins is determined by the direction of the spontaneous electron spin orientation, rather than the magnetization direction. The spontaneous electron spin polarization is produced by spin dependent reflection at the FM/GaAs interface, which is the ferromagnetic proximity polarization (FPP). Furthermore, the FPP spin polarizations in MnAs/GaAs and Fe/GaAs

are opposite. The MnAs/GaAs gives electron spin polarization antiparallel to the magnetization and nuclear field in the same direction as the applied field, whereas the Fe/GaAs gives electron spin polarization parallel to the magnetization and nuclear field opposite to the applied field. In Fe/GaAs, the very strong negative nuclear field even quenches the electron-spin precession. In addition, bias voltage were found to be able to modulate the strength of FPP effect and nuclear field [110], but no sign change was observed with bias.

1.3.3 Importance of FM/Semiconductor interfaces

A central issue for spin creation and detection is the spin dependent transport through interfaces, i.e. spin dependent transmission and reflection at the interface. Spin dependent reflection is an important process, because the electrons in semiconductor experience spin dependent reflection when in contact with magnetic electrode, at injector and detector, or during transport. Spin extraction, can be directly used as a way of spin creation. While for both processes, the physics of FM/semiconductor interface is of fundamental interest.

There are existing examples of sign change in MR with interface modification. In Co/tunnel barrier/LSMO junctions, the sign of MR depends on the tunnel barrier whether Al_2O_3 or STO, which was interpreted as changing of electronic structure due to interfacial bonding between the FM and barrier [111]. In Co/Al_2O_3/Co MTJs, the sign of spin polarization could be reversed by inserting a Ru monolayer in between the Co electrode and Al_2O_3 tunnel barrier, which is attributed to modification of the local density of states at the interface [112].

In Fe/GaAs Schottky tunnel barrier heterostructures, the spin injection and detection are both found to be dependent on the bias voltage and the interfacial structures [24, 70, 102, 103]. Sign change have been observed from time to time. Schultz et al. did systematic study of influence of Fe growth temperature and post annealing on the spin injection efficiency, detected with EL. A sign change was observed with the growth temperature of Fe, and the mechanism was proposed to be changes in local spin polarization due to other phases formed at the Fe/GaAs interface. Very recent work of temperature dependence study of non-local spin accumulation showed that the post annealing changes the spin-transfer efficiency at the injector and detector electrodes [103]. In addition, the presence of oxide barrier in principle provides a large spin-dependent resistance, but also complicates the tunneling process [35, 38], which requires more study in the future.

1.4 This thesis

We utilize optical method of ferromagnetic proximity polarization (FPP) to study spin dependent reflection in FM/GaAs heterostructures. All growth conditions or modification of the FM/GaAs interfaces would change the spin dependent process and influence the spin injection/extraction or detection efficiencies. FPP is a method probes the property of interest directly, and also useful for engineering the interface for best performance. The spin dependent transmission and reflection depends on the properties of the interfaces in two aspects, intrinsic and extrinsic properties. Here the “intrinsic” and “extrinsic” are borrowed from the interfacial resistance. “Intrinsic” properties are related

to the electronic structure of each material; “extrinsic” properties are related to disorders, such as roughness, interfacial phase from interdiffusion.

This thesis is constructed as follows: In chapter 2, the experiment techniques and related background will be described in details. There are two main measurement techniques, ferromagnetic proximity polarization (FPP) and the FPP induced dynamic nuclear polarization. Both measurements are based on time-resolved Faraday rotation (TRFR) in ferromagnet/GaAs heterostructures. FPP is an optical analogue to spin extraction: optically excited electrons in semiconductor get polarized as electron wave experiences spin dependent transmission and reflection when passing through the ferromagnet/semiconductor interface. By monitoring the spin dynamics, the spontaneous spin polarization generated by FPP effect is revealed. The heterostructures are fabricated by molecular beam epitaxy. In chapter 3 and chapter 4, I will present study of Fe/MgO/GaAs and Fe_3O_4/GaAs systems with ultrafast optics measurement of FPP. In both systems, interesting spin dependent phenomena were observed with thickness change of interlayer or FM layer, and tuning of spin dependent reflection was realized by interface modification.

References:

[1] J. J. Sakurai, *Modern quantum mechanics* (Addison-Wesley, Redwood City, California, 1985), p. 474.

[2] S. A. Wolf *et al.*, Science **294**, 1488 (2001).

[3] D. D. Awschalom, N. Samarth, and D. Loss, *Semiconductor Spintronics and Quantum Computation* (Springler-Verlag, Berlin, 2002), p. 315.

[4] M. N. Baibich *et al.*, Phys. Rev. Lett. **61**, 2472 (1988).

[5] G. Binasch *et al.*, Physical Review B **39**, 4828 (1989).

[6] C. Chappert, A. Fert, and F. N. Van Dau, Nat Mater **6**, 813 (2007).

[7] G. A. Prinz, Science **282**, 1660 (1998).

[8] S. S. P. Parkin *et al.*, Nature Materials **3**, 862 (2004).

[9] S. Yuasa *et al.*, Nature Materials **3**, 868 (2004).

[10] S. Ikeda *et al.*, Applied Physics Letters **93**, 082508 (2008).

[11] S. E. Thompson, and S. Parthasarathy, Materials Today **9**, 20 (2006).

[12] D. D. Awschalom, and M. E. Flatte, Nature Phys. **3**, 153 (2007).

[13] I. Zutic, J. Fabian, and S. Das Sarma, Reviews of Modern Physics **76**, 323 (2004).

[14] J. M. Kikkawa, and D. D. Awschalom, Phys. Rev. Lett. **80**, 4313 (1998).

[15] H. Ohno *et al.*, Nature **408**, 944 (2000).

[16] Y. Kato *et al.*, Nature **427**, 50 (2004).

[17] S. A. Crooker, and D. L. Smith, Physical Review Letters **94**, 236601 (2005).

[18] M. H. Mikkelsen *et al.*, Nat Phys **3**, 770 (2007).

[19] A. T. Hanbicki *et al.*, Applied Physics Letters **82**, 4092 (2003).

[20] S. Datta, and B. Das, Appl. Phys. Lett. **56**, 665 (1990).

[21] C. Ciuti, J. P. McGuire, and L. J. Sham, Applied Physics Letters **81**, 4781 (2002).

[22] H. Dery *et al.*, Nature **447**, 573 (2007).

[23] B. Behin-Aein *et al.*, Nat Nano **5**, 266 (2010).

[24] X. Lou *et al.*, Nature Phys. **3**, 197 (2007).

[25] R. Fiederling *et al.*, Nature **402**, 787 (1999).

[26] Y. Ohno *et al.*, Nature **402**, 790 (1999).

[27] G. Schmidt *et al.*, Phys. Rev. B **62**, 4790(R) (2000).

[28] A. Fert, and H. Jaffres, Phys. Rev. B **64**, 184420 (2001).

[29] E. I. Rashba, Phys. Rev. B **62**, 16267(R) (2000).

[30] W. H. Butler *et al.*, Phys. Rev. B **63**, 054416 (2001).

[31] H. Ohno, Science **281**, 951 (1998).

[32] X. Jiang *et al.*, Phys. Rev. Lett. **94**, 056601 (2005).

[33] I. Appelbaum, B. Huang, and D. J. Monsma, nature **447**, 295 (2007).

[34] B. T. Jonker *et al.*, Nature physics **3**, 542 (2007).

[35] S. P. Dash *et al.*, Nature **462**, 491 (2009).

[36] N. Tombros *et al.*, nature, 571 (2007).

[37] V. F. Motsnyi *et al.*, Applied Physics Letters **81**, 265 (2002).

[38] M. Tran *et al.*, Physical Review Letters **102**, 036601 (2009).

[39] T. Sasaki *et al.*, App. Phys. Expr. **2**, 053003 (2009).

[40] A. M. Bratkovsky, and V. V. Osipov, Journal of Applied Physics **96**, 4525 (2004).

[41] H. Dery, and L. J. Sham, Phys. Rev. Lett. **98**, 046602 (2007).

[42] H. Ohno *et al.*, Phys. Rev. Lett. **68**, 2664 (1992).

[43] H. Ohno *et al.*, Appl. Phys. Lett. **69**, 363 (1996).

[44] T. Dietl *et al.*, Science **287**, 1019 (2000).

[45] D. Chiba, F. Matsukura, and H. Ohno, Applied Physics Letters **89**, 162505 (2006).

[46] S. Koshihara *et al.*, Physical Review Letters **78**, 4617 (1997).

[47] T. Jungwirth *et al.*, Phys. Rev. B **72**, 165204 (2005).

[48] K. C. Ku *et al.*, Applied Physics Letters **82**, 2302 (2003).

[49] A. H. MacDonald, P. Schiffer, and N. Samarth, Nat Mater **4**, 195 (2005).

[50] S. J. Potashnik *et al.*, Physical Review B **66**, 012408 (2002).

[51] M. L. Reed *et al.*, Applied Physics Letters **79**, 3473 (2001).

[52] K. R. Kittilstved *et al.*, Physical Review Letters **97**, 037203 (2006).

[53] M. Jamet *et al.*, Nat Mater **5**, 653 (2006).

[54] J. E. Hirsch, Physical Review Letters **83**, 1834 (1999).

[55] J. Sinova *et al.*, Physical Review Letters **92**, 126603 (2004).

[56] S. O. Valenzuela, and M. Tinkham, Nature **442**, 176 (2006).

[57] T. Seki *et al.*, Nat Mater **7**, 125 (2008).

[58] T. Kimura *et al.*, Physical Review Letters **98**, 156601 (2007).

[59] S. Murakami, N. Nagaosa, and S.-C. Zhang, Science **301**, 1348 (2003).

[60] Y. K. Kato *et al.*, Science **306**, 1910 (2004).

[61] J. Wunderlich *et al.*, Physical Review Letters **94**, 047204 (2005).

[62] B. A. Bernevig, T. L. Hughes, and S.-C. Zhang, Science **314**, 1757 (2006).

[63] M. Konig *et al.*, Science **318**, 766 (2007).

[64] M. Johnson, and R. H. Silsbee, Physical Review Letters **55**, 1790 (1985).

[65] F. J. Jedema *et al.*, Nature **416**, 713 (2002).

[66] H. C. Koo *et al.*, Science **325**, 1515 (2009).

[67] F. J. Jedema *et al.*, Physical Review B **67**, 085319 (2003).

[68] X. Lou *et al.*, Physical Review Letters **96**, 176603 (2006).

[69] F. Meier, and B. P. Zachachrenya, *Optical Orientation, Modern Problems in Condensed Matter Science* (North-Holland, Amsterdam, 1984), Vol. 8.

[70] S. A. Crooker *et al.*, Science **309**, 2191 (2005).

[71] P. Kotissek *et al.*, Nat Phys **3**, 872 (2007).

[72] R. J. Epstein *et al.*, Nat Phys **1**, 94 (2005).

[73] J. Berezovsky *et al.*, Science **314**, 1916 (2006).

[74] J. Berezovsky *et al.*, Science **320**, 349 (2008).

[75] D. Press *et al.*, Nature Photonics **4**, 367 (2010).

[76] J. A. Gupta *et al.*, Physical Review B **59**, R10421 (1999).

[77] J. A. Gupta *et al.*, Physical Review B **66**, 125307 (2002).

[78] J. J. Baumberg, and D. D. Awachalom, Phys. Rev. Lett. **72**, 717 (1994).

[79] J. M. Kikkawa, and D. D. Awschalom, Nature **397**, 139 (1999).

[80] R. K. Kawakami *et al.*, Science **294**, 131 (2001).

[81] J. M. Kikkawa *et al.*, Science **277**, 1284 (1997).

[82] B. Beschoten *et al.*, Physical Review B **63**, 121202 (2001).

[83] S. Ghosh *et al.*, Applied Physics Letters **86**, 232507 (2005).

[84] R. J. Epstein *et al.*, Phys. Rev. B **65**, 121202 (2002).

[85] C. B. Murray, D. J. Norris, and M. G. Bawendi, Journal of the American Chemical Society **115**, 8706 (1993).

[86] M. Paillard *et al.*, Physical Review Letters **86**, 1634 (2001).

[87] J. A. Gupta *et al.*, Science **292**, 2458 (2001).

[88] R. C. Myers *et al.*, Nat Mater **7**, 203 (2008).

[89] M. Oestreich *et al.*, Semicond. Sci. Technol. **17**, 285 (2002).

[90] S. A. Crooker *et al.*, Nature **431**, 49 (2004).

[91] M. Oestreich *et al.*, Physical Review Letters **95**, 216603 (2005).

[92] S. A. Crooker, L. Cheng, and D. L. Smith, Physical Review B **79**, 035208 (2009).

[93] G. M. Muller *et al.*, Physical Review Letters **101**, 206601 (2008).

[94] S. A. Crooker *et al.*, Physical Review Letters **104**, 036601 (2010).

[95] J. M. MacLaren *et al.*, Physical Review B **59**, 5470 (1999).

[96] O. Wunnicke *et al.*, Physical Review B **65**, 241306 (2002).

[97] B. T. Jonker *et al.*, Physical Review B **62**, 8180 (2000).

[98] O. M. J. van 't Erve *et al.*, Applied Physics Letters **84**, 4334 (2004).

[99] H. J. Zhu *et al.*, Physical Review Letters **87**, 016601 (2001).

[100] A. N. Chantis *et al.*, Physical Review Letters **99**, 196603 (2007).

[101] S. A. Crooker *et al.*, Physical Review B **80**, 041305 (2009).

[102] B. D. Schultz *et al.*, Physical Review B **80**, 201309 (2009).

[103] G. Salis *et al.*, Physical Review B **81**, 205323 (2010).

[104] T. Manago, and H. Akinaga, Applied Physics Letters **81**, 694 (2002).

[105] N. Tombros *et al.*, Physical Review Letters **101**, 046601 (2008).

[106] C. Jozsa *et al.*, Physical Review Letters **100**, 236603 (2008).

[107] C. Jozsa *et al.*, Physical Review B **79**, 081402 (2009).

[108] W. Han *et al.*, Physical Review Letters **102**, 137205 (2009).

[109] J. Stephens *et al.*, Physical Review Letters **93**, 097602 (2004).

[110] R. J. Epstein *et al.*, Physical Review B **68**, 041305 (2003).

[111] J. M. De Teresa *et al.*, Science **286**, 507 (1999).

[112] P. LeClair *et al.*, Physical Review B **64**, 100406 (2001).

Chapter II

Experimental Techniques and Background

In this thesis, ultrafast optics techniques are employed to study ferromagnet/semiconductor heterostructures, especially spin dependent reflection at the interfaces. Ferromagnetic proximity polarization (FPP) is a spontaneous electron spin polarization induced in the semiconductor layer in adjacent to a ferromagnetic layer, where the electron carriers are excited by linearly polarized light, and the spin dynamics are measured in a pump-probe scheme. A related effect is the ferromagnetic imprinting of nuclear spins in these structures: nuclear spins are dynamically polarized by electron spins through hyperfine interaction, and the nuclear spins act back to electron spin dynamics by creating an effective magnetic field to electrons. These two measurement techniques have their own advantages, and are complimentary in certain aspects, which will be specified in details later in this and next chapters. The FM/SC heterostructures are fabricated by molecular beam epitaxy (MBE). For the two systems of interest, Fe/MgO/GaAs and Fe_3O_4/GaAs, oxide materials are crucial for the successful realization of high quality interfaces. I use reactive MBE growth method for both MgO and Fe_3O_4 on GaAs(001). In the following text, the optics measurement techniques, molecular beam epitaxy and related background will be introduced.

2.1 Time-resolved Faraday rotation (TRFR)

TRFR is an optical pump-probe technique for measuring electron spin dynamics

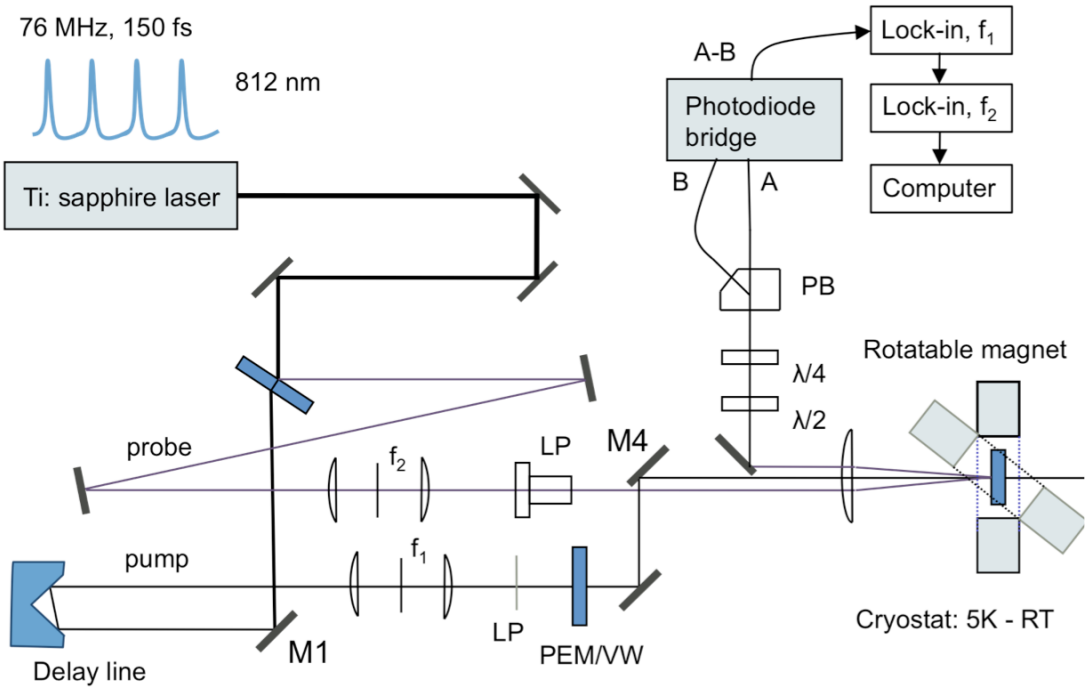

FIG 2.1 Optics setup for time-resolved Kerr (Faraday) rotation. The Faraday rotation measurement setup is the same, except for measuring the transmitted probe beam. The abbreviations in the figure stand for the following: LP (linear polarizer), PEM (photo elastic modulator), VW (variable wave plate), λ/2 (half wave plate), λ/4 (quarter wave plate), PB (polarizing beam splitter). Mechanical choppers are used for modulating the pump and probe beam intensities between on and off with frequencies f_1 and f_2.

in a variety of semiconductors, usually direct bandgap semiconductors [1-4]. This thesis will be mainly on GaAs heterostructures, so I just talk about the case of GaAs. The laser source is a wavelength tunable Ti:sapphire laser that generates ultrashot pulses (~150 ps) at a repetition rate of 76 MHz. The wavelength is tuned to the bandgap of GaAs, 812nm.

A beam splitter divides the beam into two sub-beams as pump and probe beams. As shown in FIG 2.1, the pump beam goes through a delay line with mechanical control, which allows continuously varying the path length. The probe beam path is longer than that for pump beam path by Δl, thus delayed by time $\Delta t = \Delta l/c$, where c is the speed of light. The pump beam is either circularly polarized or linearly polarized, and here we use circularly polarized case as an example to explain the TRFR measurement. The linearly polarized pump beam will be discussed in next section 2.2. The circularly polarized pump

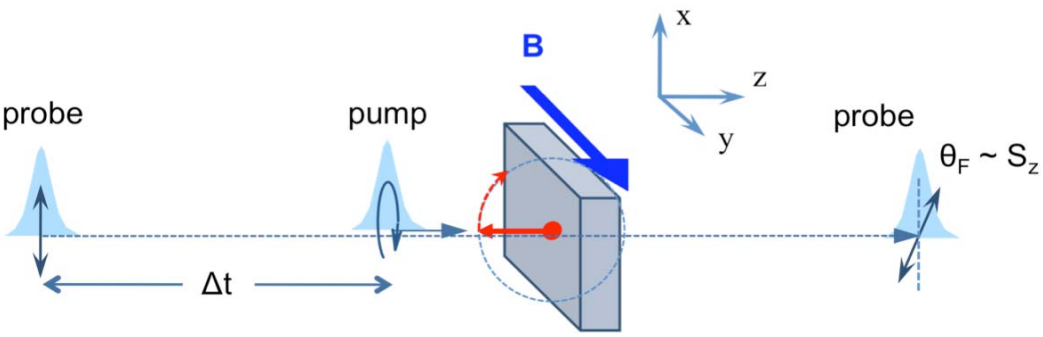

FIG 2.2 Measurement geometry of TRFR. The pump and probe beams are incident on the sample normally, along the *z*-axis. Magnetic field is applied perpendicular to the light propagation direction, along *y*-axis. The spin precession about the magnetic field, in the *xz*-plane. The pump beam is circularly polarized and excite electron spins in the semiconductor. The probe beam is delayed by Δt, linearly polarized. After it passes through the sample, the polarization plane rotates by θ_F, which is proportional to spin polarization along the *z*-axis.

pulse excites spin-polarized carriers in the semiconductor (FIG 2.2), based on optical selection rules (details in 2.1.1). A linearly polarized probe beam measures the electron spin polarization along the beam path by Faraday rotation (transmission geometry, FIG 2.2) or Kerr rotation (reflection geometry, the case of FIG 2.1). A balanced photodiode

bridge and lock-in's are used to analyze the Faraday rotation signal. As you vary the time delay Δt, the electron spin polarization changing as a function of time will be recorded. The typical TRFR scan in zero magnetic filed is shown in FIG 2.3 (a). When a magnetic

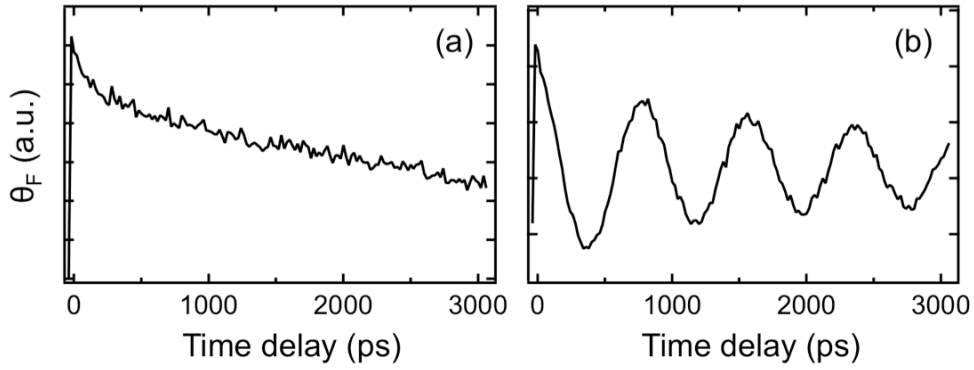

FIG 2.3 Typical TRFR scan curves at (a) zero field and (b) 2100 G measured on GaAs film.

field is applied perpendicular to the initial spin polarization, the electron spins precess with Larmor frequency $v_L = g\mu_B B / h$, where g is the electron g-factor (g = -0.44 for GaAs at T = 5 K), μ_B is the Bohr magneton, and h is Planck's constant. One typical TRFR scan in magnetic field is shown in FIG 2.3 (b). The signal can be expressed as $\theta_F = Ae^{-\Delta t/T_2^*}\cos(v_L \Delta t) + O$, where T_2^* is the transverse spin lifetime, A is the oscillation amplitude, and O is a background offset. From the scans, we can fit the curves and get the spin lifetimes. When the measurement is performed reflection geometry, it is referred as time-resolved Kerr rotation (TRKR). Details about setting up the measurement are in Appendix A.

This technique has revealed very long spin lifetimes in bulk GaAs [1], much longer than the carrier recombination time. FIG 2.4 explains how the spins persist for so long as four stages. First, before excitation, there are equal populations of spin up and

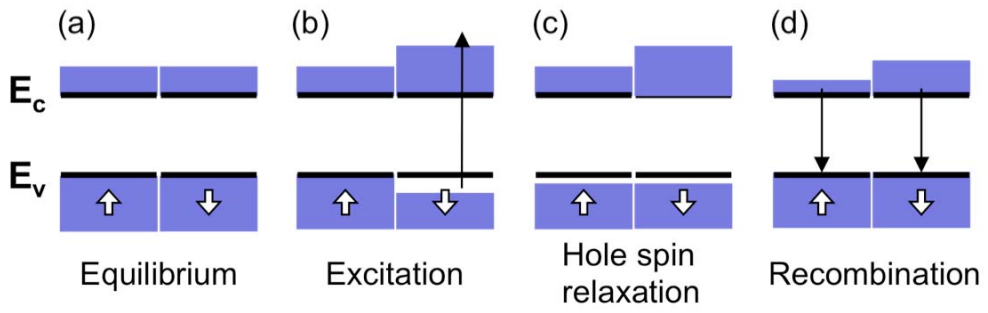

FIG 2.4 Schematic band population of majority and minority electrons in different stages of measurement. After a long time until the electron spin relaxes, the state comes back to 'equilibrium'.

spin down electrons, with zero net spin. Second, excitation by circularly polarized pump beam creates spin imbalances in the conduction band and valence band. Third, the hole spins relaxes very fast (< 1 ps) [5], and the electron spin in the conduction band remains. Last, after the recombination of electrons and holes, the electron spin decreases but the left spin imbalance persist for a long time. The relaxation mechanisms are mainly spin-orbit scattering with phonons and/or impurities, or inhomogeneous precession.

2.1.1 Optical spin orientation (pump)

The optical orientation is closely related to the band structure of GaAs, and the important bands for (001) direction are shown in FIG. 2.5. The band gap is E_g = 1.52 eV at T = 0 K, and the spin-orbit splitting is Δ_{so} = 0.34 eV. The excitation (or recombination)

probabilities are obtained by calculating the matrix element of $\langle i|X \pm iY|f\rangle$, where the i and f are initial and final states of the transition, "+" and "-" signs correspond to right circularly polarized light σ^+ and left circularly polarized light σ^-. The results are summarized as the selection rule depicted in Fig. 2.5. The states are represented by

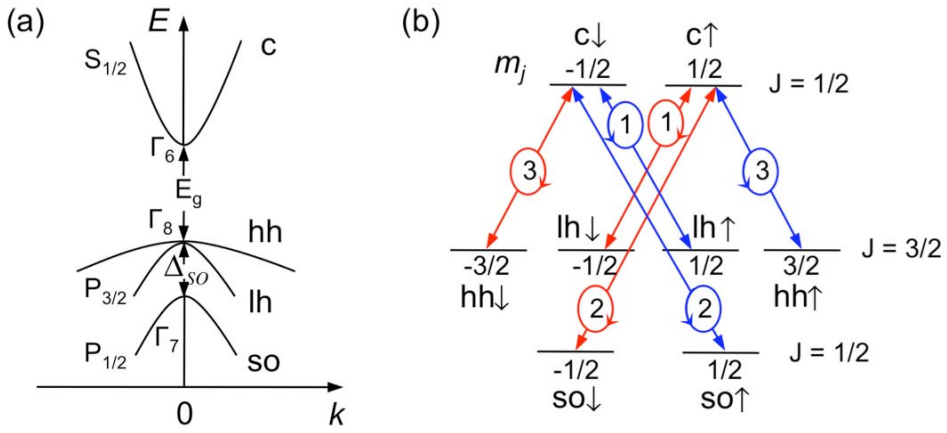

FIG 2.5 Interband transitions in GaAs: (a) Schematic band diagram of GaAs near the center of the Brillouin zone. "c, hh, lh, and so" denote conduction band, valence heavy hole, valence light hole and spin-orbit split-off subbands, respectively. (b) Selection rules and relative intensities of interband transitions between the m_j sublevels for circularly polarized light.

quantum numbers of the total angular momentum J (orbital + spin angular momentum) and its projection onto the z-axis m_j: $|J, m_j\rangle$. The relative transition probabilities are indicated as the circled numbers, and arrows on the circles indicate the helicity of light.

For right circularly polarized light with energy $\hbar\omega$ between E_g and $E_g + \Delta_{SO}$, the excitation only involve light and heavy hole subbands. It is easy to get the spin

polarization of the excitation $P = \frac{n_\uparrow - n_\downarrow}{n_\uparrow + n_\downarrow} = \frac{1-3}{1+3} = -\frac{1}{2}$, where $n_\uparrow$ ($n_\downarrow$) denotes the density of electrons polarized parallel (antiparallel) to the direction of light propagation. The negative sign means that the excited spin polarization is antiparallel to the direction of light propagation. With excitation energy $\hbar\omega$ much larger than $E_g + \Delta_{SO}$, similar analysis can find that the electrons will not be spin polarized (P = 0), because the spin-split off bands cancel off the spin polarization. In other words, the spin-selectivity of the transitions is due to the spin-orbit splitting of the valence band. A thorough description of optical orientation can be found in Ref. [6].

The typical laser power we use is in the order of 1 mW, so the excitation density N_{ex} (5×10^{16}/cm^3, estimate calculation in Appendix B) is of the same order as the doping density n (7×10^{16}/cm^3). Increased excitation density degrades transverse spin lifetime T_2^* in nondegenerate samples, so the low excitation power is generally good for long spin lifetime. However, the study of this thesis does not focus on spin dynamics, but the spin dependent reflection of carriers at the FM/GaAs interface, so relatively large intensity is favorable for collective measurement. The wavelength we use is 812nm (1.527 eV), which is right above the bandgap of GaAs, so it does not affect the free electron spin lifetime.

2.1.2 Faraday rotation basics

The Faraday effect is a magneto-optical effect that the polarization plane of a linearly polarized light beam rotates by θ_F when passing through a longitudinal magnetic

field or a medium with internal magnetization. Macroscopically, it results from the difference in indices of refraction for left- and right-circularly polarized light, $\theta_F(\omega) = \frac{\omega d}{2c}(\eta_- - \eta_+)$, where ω is the frequency of light, d is the thickness of the medium and c is the speed of light. The magnitude of Faraday rotation is proportional to the magnetization of the medium.

In the TRFR measurement, the circularly polarized pump beam creates a spin imbalance in the conduction band of GaAs, as shown in FIG 2.4 (b) and FIG 2.6 (a). Due to the perturbation of pump beam, the absorption of the probe beam show difference

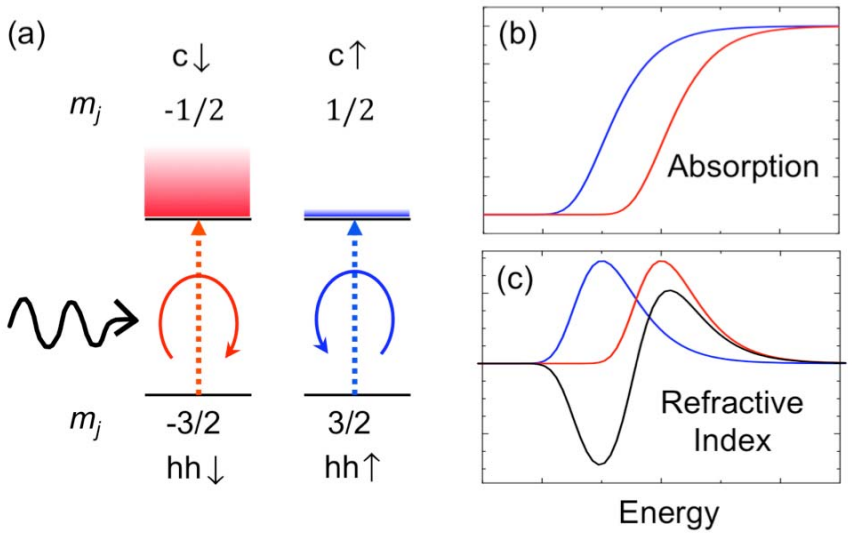

FIG 2.6 Principle of probing of spin imbalance by Faraday rotation. (a) Schematic optical excitation (b) The absorption spectra for right (red) and left (blue) circularly polarized light. (c) The according refractive index dispersion. Red and blue are for right and left circularly polarized light, respectively. The difference (η_+ - η_-) is represented by the black curve.

between right circularly polarized light and left circularly polarized light at certain energy, as shown in FIG 2.6 (a) and (b). In FIG 2.6 (a), only transitions from heavy-hole bands to conduction bands are labeled, since the transition probability dominates. Absorptions of right and left-circularly polarized light are associated to transitions to spin down and spin up states in the conduction band. Again, the spin-orbit splitting is necessary for the detection of spin polarization in GaAs. Applying the Kramers–Kronig relations, the indices of refraction for RCP light (red curve) and LCP light (blue curve) are obtained, as shown in FIG 2.6 (c). The difference of the two is the black curve, which exhibits a sign change with energy. This energy dependence is observed in our experiments all the time, consistent with other work [7], and adopted as a reference to identify the two maximums. We usually choose the higher energy maximum (812 nm) for the purpose of more effective excitation, since we use the same wavelength for the pump beam.

2.2 Ferromagnetic proximity polarization

Ferromagnetic proximity polarization (FPP) is the spontaneous spin polarization of optically injected unpolarized electrons by interaction with a FM/GaAs interface. The FPP occurs within the first 50 ps after the optical excitation. Measuring the spin dynamics of the reflected electrons (time after 50 ps) by time-resolved Faraday rotation (TRFR) reveals the initial electron spin. The FPP measurement is different from typical TRFR measurements that employ a circularly-polarized pump pulse to generate spin polarized electrons in the GaAs. In those studies, the focus is usually on the spin dependent properties of the GaAs such as the electron spin dynamics, spin relaxation in

GaAs, spin manipulation, etc. In the FPP measurement, the focus is on what happens at

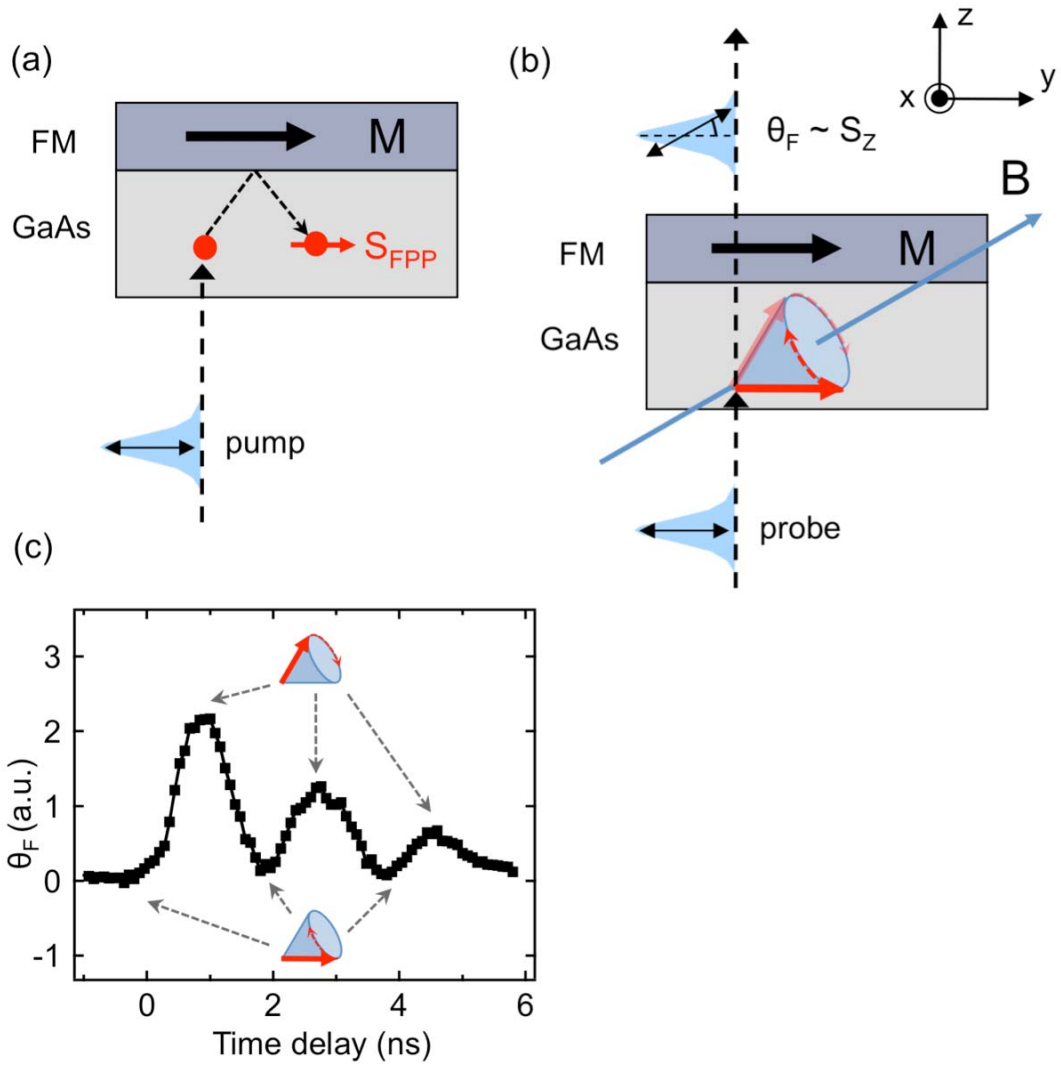

FIG 2.7 (a) Ferromagnetic proximity polarization effect. Unpolarized electron carriers are excited by optical linearly polarized pump pulse. Spontaneous electron spin is generated due to spin dependent transmission and reflection at the ferromagnet/GaAs interface. The electron spin aligns along the magnetization axis of the ferromagnet layer. (b) Ultrafast optics measurement of ferromagnetic proximity polarization. (c) A typical time delay scan. By monitoring the spin dynamics, the initial spin polarization S_{FPP} is determined.

the FM/GaAs interface, and the electron spin dynamics in GaAs (up to 7 ns) is utilized as a tool to measure the spin dependent reflection at zero time (< 50 ps).

The measurement of FPP is illustrated in FIG 2.7 (a) and (b). The pump and probe beams have normal incidence (*z*-axis), and the applied magnetic field B_{app} is tilted out of the film plane by an angle $\alpha = 30°$ (in the *y*-*z* plane). B_{app} is set to 900 G and we assume that the magnetization remains in the film plane (*x*-*y*) due to magnetic shape anisotropy. With a linearly polarized pump beam, unpolarized electrons are excited in the GaAs layer. Due to spin dependent Fermi velocity of the ferromagnet layer, the electron wave experience a spin dependent transmission and reflection at the FM/GaAs interface, thus generate a spontaneous spin polarization S_0^{FPP}, oriented along the magnetization axis in the GaAs layer. We adopt a sign convention that S_0^{FPP} is positive (negative) when the initial spin is parallel (antiparallel) to the magnetization $\boldsymbol{M}$. The B_{app} induces spin precession about a cone (FIG 2.7b) to generate a *z*-component of spin, and the dynamics is measured by a time-delayed, linearly-polarized probe pulse via Faraday rotation ($\theta_F \propto S_z$) of the polarization axis. The pump-probe intensity ratio is ~15 and the average pump intensity is 600 W/cm^2 (the FPP signal scales linearly with the pump intensity in the range of 1000 W/cm^2). Quantitatively, the spin dynamics for this population includes both a transverse component (with lifetime T_2^*) and a longitudinal component (with lifetime T_1), and the TRFR signal is given by:

$$S_z = S_0^{FPP}\left(\hat{m}\cdot\hat{e}_y\right)\sin\alpha\cos\alpha\left[\exp\left(-\Delta t/T_1\right)-\cos\left(2\pi\nu\Delta t\right)\exp\left(-\Delta t/T_2^*\right)\right] \quad (2.1)$$

where $\nu = -\nu_L = -g\mu_B B_{app} / h$ is the Larmor precession frequency, g is the g-factor of GaAs ($g \approx -0.44$), μ_B is the Bohr magneton, h is Planck's constant, Δt is the pump-probe time delay, and $\hat{m}$ is the unit vector of the magnetization. Because the transformation ($B_{app} \rightarrow -B_{app}$, $\boldsymbol{M} \rightarrow -\boldsymbol{M}$) yields $S_z(\Delta t) \rightarrow -S_z(\Delta t)$, we perform TRFR scans for positive and negative B_{app} and subtract the two curves to eliminate background signals unrelated to FPP. A typical time delay scan of the z-component electron spin is shown in FIG 2.7 (c). At zero time, the electron spin is in-plane, and the $\theta_F \propto S_z$ is zero; as it precesses and gradually goes out-of-plane, the θ_F increases to maximum; with further precession, the spin turns in-plane again, corresponding to a minimum in the time delay scan curve. The sign and magnitude of the spin precession signal is directly related to the value of S_{FPP}, which is of primary interest in our measurement. Quantitatively, the value of S_{FPP} is obtained by fitting the TRFR data with equation (2.1).

The possibility that the TRFR signal originates from precession of the FM magnetization is excluded by the following tests. First, we measure the wavelength dependence of the TRFR signal. A signal from electron spin in GaAs will reduce quickly as the wavelength is tuned away from the band gap, while a signal from the FM magnetization will not. Second, we measure the precession frequency as a function of magnetic field. For electron spin precession in GaAs, the frequency increases linearly with the field and the proportionality constant should yield $|g| = 0.44$. For magnetization precession, the frequency is determined by a combination of the applied magnetic field and anisotropy field, which is not linear with the applied field. Third, we lower the temperature down to 5 K to verify the FPP phenomena by observing the resulting

ferromagnetic imprinting of nuclear spins. We have performed all these tests to verify that the TRFR signal originates from electron spin precession in the GaAs, as opposed to magnetization precession of the FM.

2.2.1 Theory of FPP

There are mainly two theory papers on the FPP effect, one based on general scattering of the electron spin density matrix [8] and the other on time-dependent interaction between the conduction-band electrons and the ferromagnet in a ‘‘fireball-afterglow’’ scenario [9]. The latter model gives clear picture about the physical processes happening in the time domain: the FPP takes place in tens of picoseconds after the pump beam incidence, in which the excited electron carriers interact with the FM/semiconductor interface (the “fireball” regime), and the excited holes helps for the electrons to overcome the Schottky barrier. The interaction turns off with hole vanishing, and the spin dynamics continues with a relatively long lifetime, which is the “afterglow” regime. The interaction is modeled as spin dependent current flow across FM/semiconductor interface and a rising time of the FPP effect could be estimated (35 ps), consistent with the experiment.

The former model captures the major physical processes and factors that affect the magnitude of the FPP effect in an intuitive way. As shown in FIG 2.8, the FM/Schottky barrier/GaAs structure system is treated as one dimensional tunnel barrier potential. The spin dependent reflection coefficients $r_{\pm}$ (+ sign for majority, - sign for minority) are expressed as:

$$r_{\pm} = \frac{e^{2k_b a}(i\upsilon_{\pm}^{fm} - \upsilon_b)(i\upsilon_x + \upsilon_b) - (i\upsilon_{\pm}^{fm} + \upsilon_b)(i\upsilon_x - \upsilon_b)}{e^{2k_b a}(i\upsilon_{\pm}^{fm} - \upsilon_b)(i\upsilon_x - \upsilon_b) - (i\upsilon_{\pm}^{fm} + \upsilon_b)(i\upsilon_x + \upsilon_b)} \qquad (2.2)$$

where a is the approximated square barrier thickness, $\upsilon_{\pm}^{fm}$ is the Fermi velocity of the majority/minority band in the FM, k_b is the evanescent wave vector in the barrier region and $\upsilon_b = \hbar k_b / m_s$ (m_s is the effective electron mass in semiconductor). The FM is simplified by two parabolic bands, $\upsilon_+^{fm} = \sqrt{2E_F / m_{fm}}$ and $\upsilon_-^{fm} = \sqrt{2(E_F - \Delta)/ m_{fm}}$, where m_{fm} is the effective electron mass in FM, Δ is exchange splitting. In this case, $\upsilon_+ > \upsilon_-$, e.g. Fe. The real Schottky barrier should be the bent potential $V(x)$ with

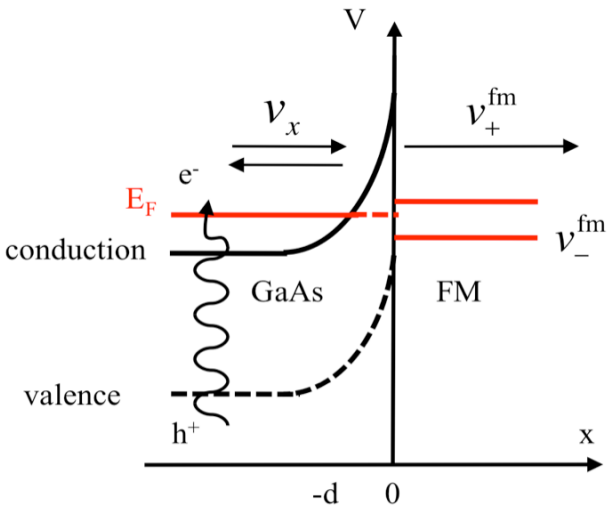

FIG 2.8 Band alignment of ferromagnet/GaAs heterostructures. The reflection and transmission for majority and minority electrons are different due to the spin dependent Fermi velocities in the ferromagnet.

depletion length $d \approx \sqrt{\varepsilon_0 U_b / (2\pi n e^2)}$, where ε_0 is the dielectric constant. The above equation could be deduced by solving the electron wavefunctions of the three regions, same as the quantum mechanics textbook problem. The detailed calculation of reflection coefficient is in Appendix C. The spin dependent reflection is represented by $|r_{-,k}|^2 - |r_{+,k}|^2$, which is a function of doping and barrier height. When $|r_{-,k}|^2 - |r_{+,k}|^2 >$ (<) 0, the minority (majority) electrons get reflected more effectively, the electron spins are parallel (antiparallel) to the magnetization of FM (***M***), corresponding to positive (negative) FPP.

The representative results from Ref. [8] are shown in FIG 2.9. The parameters

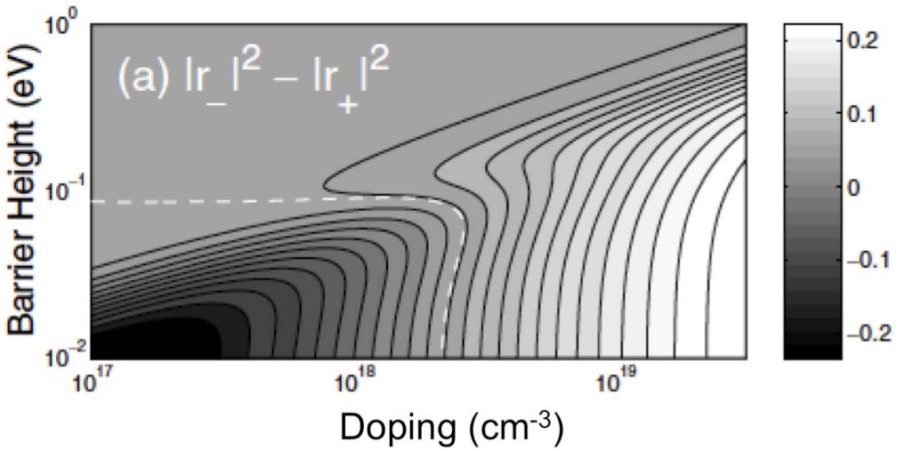

FIG 2.9 Contours of the spin reflection asymmetry as a function of the semiconductor doping *n* and the Schottky barrier height U_b. This quantity changes sign at the white dashed line. Reprint from Ref. [8], Figure 2a.

used are: v_+^{fm} = 9.4×10^{7}cm/s, v_-^{fm} = 4.6×10^{7}cm/s (corresponding to E_F=2.5 eV, Δ = 1.9 eV). The main results could be summarized as the following (Table 2.1):

For $v_+^{fm} > v_-^{fm}$ (e.g. Fe)		
Low barrier:	Fermi velocity matching	* High barrier: tunneling
Minority (low doping)	Majority (high doping)	Majority e^- has higher tunneling probability

Table 2.1 Summary of FPP calculation result as a function of barrier height and carrier concentration.

For low barrier height and low doping, the minority Fermi velocity of FM matches better with the semiconductor, so the transmission of minority is more than majority spins. When the doping is increased, the Fermi velocity of semiconductor increases, and matches better with majority at some level, which causes the sign change as function of doping concentration at low barrier height. In the case of high tunnel barrier, the tunneling is the dominant transmission mechanism, so the majority spins get transmitted more.

The factors that determine the sign of FPP are: spin dependent Fermi wavevectors of the FM layer, Schottky barrier height and thickness, carrier concentration. Other factors, non-ideal conditions should also be critical, such as the interfacial bonding, local DOS at the Fermi level.

2.2.2 Difference between FPP and electrical extraction/injection

We claim that the FPP effect is an optical analogue to electrical spin extraction, but there are also differences between FPP and electrical extraction and injection. In electrical extraction and injection, electrons involved are those close to the Fermi level and far from the Schottky barrier; in optical FPP process, the electrons are created

everywhere in the semiconductor, including the barrier region. Electrons excited near the FM/GaAs interface see a much lower and thinner Schottky barrier than electrons away from the interface (FIG 2.8). The tunneling probability is an exponential function of the Schottky barrier height and thickness, so the electrons excited close to the interface contribute to the FPP effect more significantly, although the measured effect is the average of all electrons with different barrier heights.

Reference [10] modeled the case for electrons excited optically, where the distribution of electrons in the space charge region is homogeneous, and the laser bandwidth was assumed to be ~10 meV. The calculated spin reflection coefficient difference $|r_-|^2 - |r_+|^2$ as a function of doping and Schottky barrier height at zero bias is displayed in FIG 2.10. Comparing to the simple model with single Schottky barrier

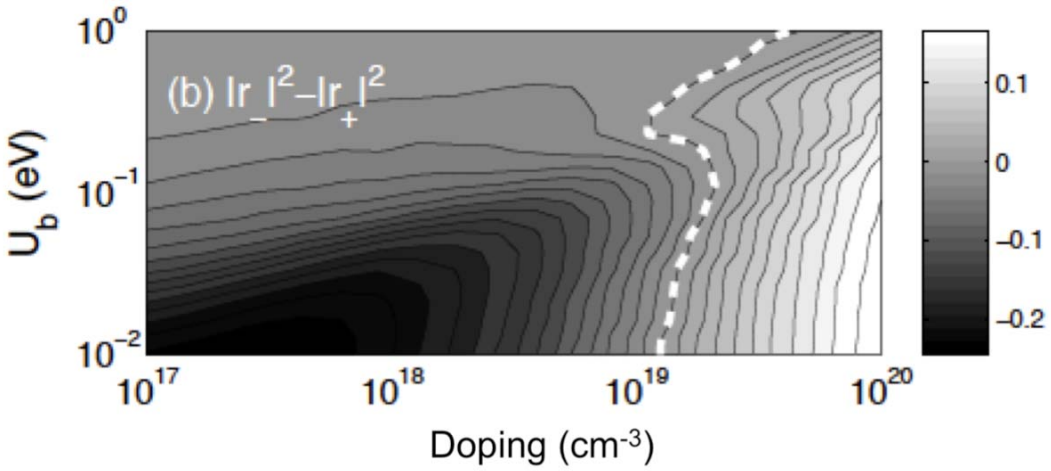

FIG 2.10 The spin reflection asymmetry as a function of the semiconductor doping n and the Schottky barrier height U_b, considering the effect of optical excitation. Reprint from Ref. [10], Figure II.7 (b).

height and thickness, the major change is that the sign change of FPP with barrier height for low doping region disappears. When the Schottky barrier is low, the change induced by optical excitation other than electrically driven injection is small, because the electrons close or far from the barrier are not too much different. While if the Schottky barrier is high, electrons distributed in the semiconductor layer see very different barrier heights. Regarding the electron spin lifetime, electrons excited high in the barrier region has no background electron density, so that it might be shorter than electrons further away from the FM/GaAs interface.

Another special effect of optical excitation is the screening of the Schottky barrier [9]. Photoexcited holes are strongly attracted by the barrier, thereby dragging electrons with them and screen the barrier. This happens at the moment of pump beam pulse excite carriers in semiconductor, before recombination of electrons and holes. So in the very shot time period of generating initial spin polarization by FPP, the electrons may feel a lower barrier height.

2.3 Ferromagnetic imprinting of nuclear spins

FPP in the FM/GaAs also results in dynamic nuclear polarization via hyperfine interaction. The polarized electrons transfer their momentum to nuclei over time (on order of minutes), and the nuclei spins act back to the electron spin dynamics (FIG 2.11). The measurement geometry is exactly the same as TRFR with circularly polarized pump beam, where the circularly polarized pump beam is also used to generate initial electron spins that are perpendicular to the magnetic field and also for FPP spin polarization. At sufficiently low temperature, the nuclei spins build up and produce an effective magnetic

field to electrons, so the electron spin precession frequency $\nu_L = g\mu_B(B_{app} + B_{nuclear})/h$ changes as the nuclear field evolves. What we are interested is the deviation of the

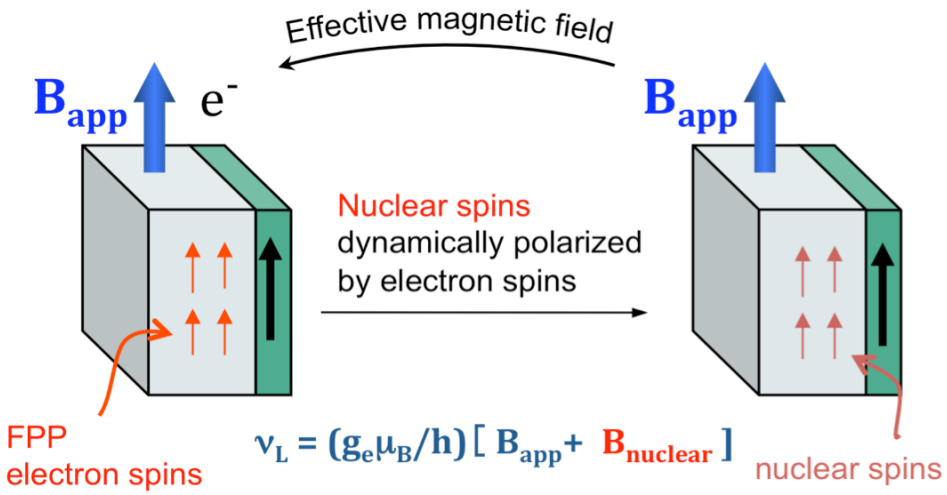

FIG 2.11 Dynamic nuclear polarization by FPP electron spins. In an applied external magnetic field, the optically injected electron get polarized by the ferromagnetic proximity polarization, and the spin momentum of these electrons transfers to nucleus through hyperfine interaction. The nuclear spins act back to electron spin dynamics in the form of an effective magnetic field, so the electron spin precession frequency has an extra term of $B_{nuclear}$.

precession frequency from the bare ν_L due to B_n. The measurement of B_n qualitatively reflects the strength of FPP effect, and it works better than the direct FPP measurement at low intensities.

To measure the nuclear field, we do the time-delay scan over and over, until the spin precession frequency saturates. Starting from the exposure of sample to laser beams, the spin dynamics evolves over lab time. A typical observed TRFR scan changing with

lab time is shown in FIG 2.12 (a), and two dimensional image plot of TRFR scans from

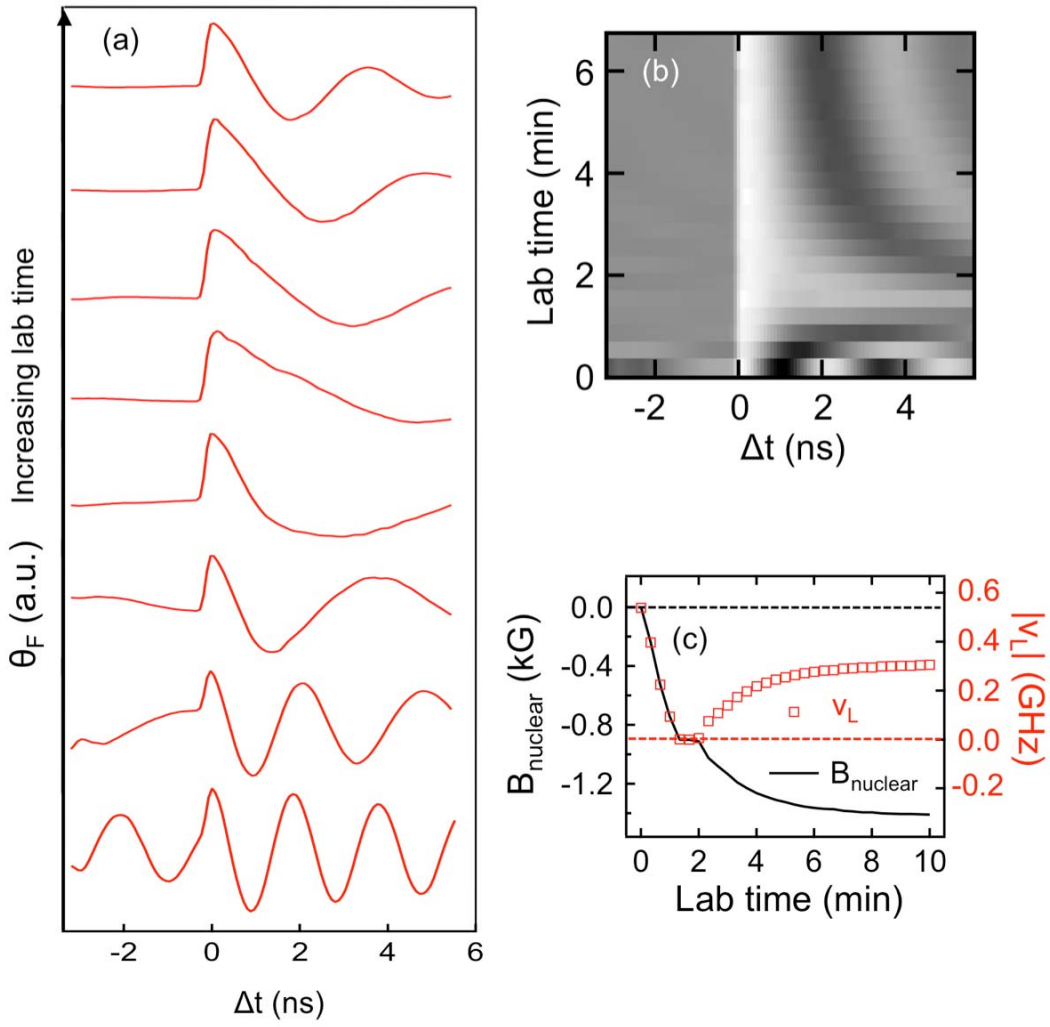

FIG 2.12 Measurement of nuclear field. (a) Time evolution of electron spin dynamics represented by the TRFR curves. (b) Two dimensional image plot of time-delay scans from zero time to 6.5 min. (c) Nuclear field and precession frequency vs. lab time. The nuclear field is proportional to the deviation of precession frequency from the black dashed line.

zero time to 7 min is shown in (b). After fitting each TRFR curves, the precession frequency vs. lab time is obtained, shown in FIG 2.12 (c). In this case, we can see that the

precession frequency first decreases, and increases again after it reaches zero. The according nuclear field B_n is negative to the applied field and keeps increasing with lab time. When B_n gets larger in amplitude than B_{app}, the precession changes direction, which explains the frequency increase after reaching zero.

The nuclear field has very strong intensity and temperature dependence, and it requires some amount of applied field [11]. The pump power we usually use is 1 to 4 mW for doing the wedge scan. Intensity dependence of B_n shows clear turn on (more discussion in Chapter 3 in the Fe/MgO/GaAs structures). The B_n could be very large at low temperatures, and we choose 5 K for our measurement for sufficient Bn but not too large saturation time. The measurement of B_n starts when the sample is exposed to pump and probe laser beams, by removing the beam block, or simply by turning on the applied magnetic field. After measuring B_n on one point on the sample, it takes same amount of time for the nuclear spins to relax. During a wedge scan, measurement of one point does not affect the measurement on next point so no wait time is needed, as long as the step size on sample is bigger than the laser spot size.

2.4 Molecular beam epitaxy (MBE)

Molecular beam epitaxy is a growth technique with monolayer precision in ultrahigh vacuum (~10^{-9} torr or better). The growth occurs on the surface of a crystalline substrate via the interaction of molecular or atomic beams with the substrate surface at an appropriate temperature. Molecular or atomic beams are created by heating up pure element materials in Knudsen cells or bombarding electron beams onto target materials (element or compounds). The cells are places towards the substrates and shutters in front

of the cells are used to precisely control the time of growth, thus thickness of the film and composition or doping of film. Ultrahigh vacuum is essential for MBE. It allows ballistic moving of the molecular beam from the cells, because the number of atoms in unit volume is low so that the mean free path of particles is long.

The system is usually equipped with in-situ reflection high-energy electron diffraction (RHEED), for monitoring quality of the film surface during growth. The energy of electron beams is on the order of 5-100 keV, and the according wave vectors are on the order of 100 Å-1, much larger than the reciprocal lattice vectors. The beam incidents on surface of the film at a glancing angle (< 5°), so the diffraction pattern is only sensitive to the top few layers. The specific RHEED pattern reflects the crystal structure and conditions of the surface. By constructing the Ewald's sphere (FIG 2.13 (a) and (b)), we can find the allowed diffraction conditions for kinematical scatterings. The reciprocal lattice of the surface (2D) is a series of rods extending infinitely particularly to the sample surface. The Ewald sphere is centered at the origin of the reciprocal lattice, with radius of $k_0 = \frac{2\pi}{\lambda}$, where λ is the wavelength of the incident electron beam. ($\lambda = \frac{hc}{E} = \frac{12400}{E}$, λ is in unit of Å, and E in unit of eV) Where the reciprocal lattice rods intersect with the Ewald sphere, the condition for constructive interference is fulfilled. The top view and side view are both illustrated in FIG 2.13. Ideally, the first order diffraction pattern is composed a set of dots on a circle. One can directly calculate the reciprocal lattice of the sample with the RHEED pattern, $b = k_0 \sin\theta \doteq k_0 \, l/D$, where b is

the reciprocal lattice constant, *l* is the spacing between the diffraction streaks, and *D* is

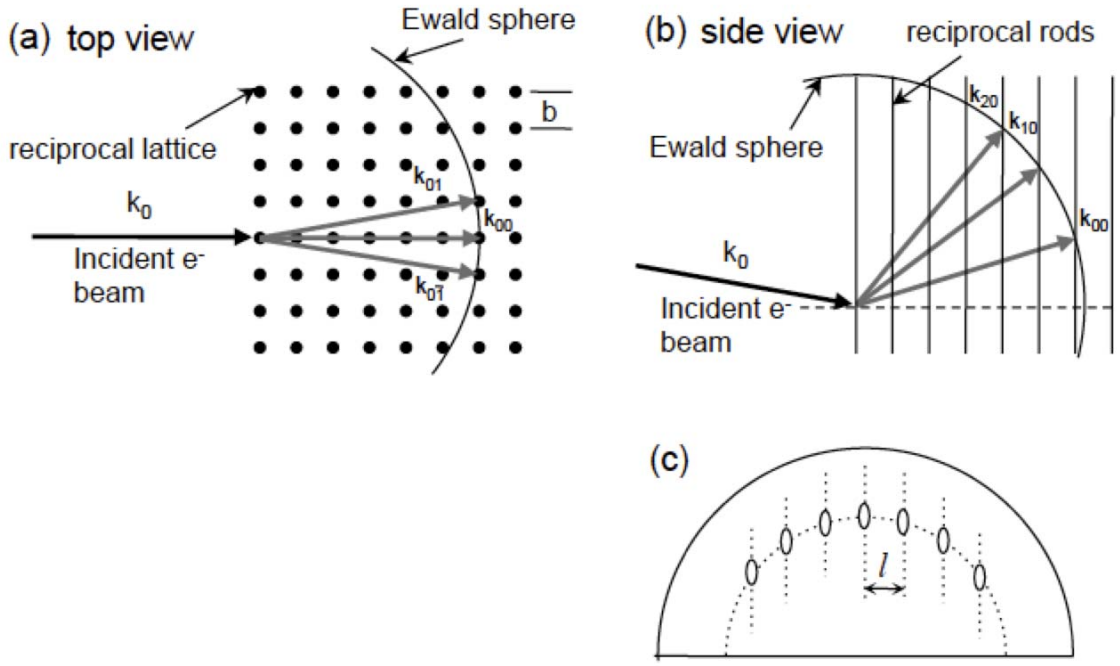

FIG 2.13 Construction of Ewald sphere (a) top view and (b) side view. (c) Typical RHEED pattern.

the distance from the sample to the receiving screen. The intensity of the specularly reflected electron beam depends on the state of the surface, in the sense of whether one monolayer is complete or partially formed. The RHEED intensity oscillates during film growth under when the growth mode is layer-by-layer, which is an indication of high quality epitaxial growth.

2.4.1 Our MBE system

The MBE chamber we use for the thesis work is customer designed, equipped with eight ports for thermal or e-beam evaporators and pure oxygen with precision leak

valve. The sources I use are Fe, Mg, Ag, Al, and they are all thermal evaporators. The typical evaporating temperatures for Fe, Mg, Ag, Al are 1180°C, 370°C, 900°C and 1200°C, respectively. The motion of the manipulator is computer controlled, being able to move in x, y, z, three directions and the temperature range is from RT to about 800°C. The base pressure of the chamber is below 5×10^{-10} torr. The deposition rate of each cell is calibrated with quartz crystal monitor at the position of sample pocket before growth. Then the cell is kept at the growth temperature and shutter is turned off for moving deposition monitor away and sample into the position. The shutter opening and closing is computer controlled for precise thickness.

The important technique for all the study is the wedge growth. As shown in FIG 2.14, it is achieved by translating the substrate behind a knife-edge shutter during growth.

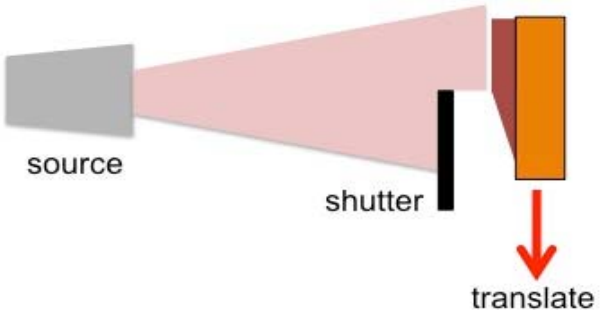

FIG 2.14 Wedge growth by molecular beam epitaxy.

The typical substrate size is 3mm×7mm, and the wedge length is 3mm or 2.5mm, with 2mm flat thickness on both sides. With the laser spot size of 40 μm, a reasonable lateral step size for measuring the wedge sample is 0.05 mm (50 μm). The wedge sample technique allows systematic study of thickness dependence, since on one sample, the

growth conditions are the same for the whole wedge, except for the thickness, and the optics measurement can be done with the same parameters (e.g. laser power, temperature) at once.

2.4.2 GaAs substrate preparation and characterization

For all the samples mentioning in this thesis, the template substrate is n-GaAs with the structure showing in FIG 2.15 (a). The active layer for the optics measurement is the top 123 nm GaAs. The doping concentration of 7×10^{16} /cm^3 is chosen for long spin coherence time in GaAs. The AlGaAs layer is a barrier for confining electrons close to

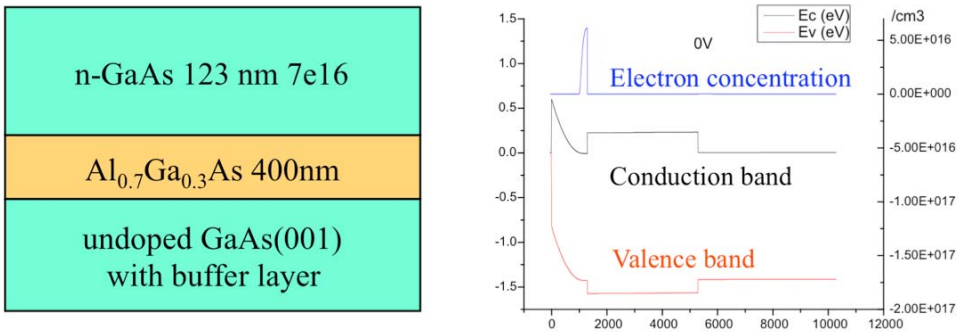

FIG 2.15 (a) Structure of the standard GaAs template. The doping concentration of 7 × 10^{16}/cm^3 for n-GaAs epilayer is chosen for long spin lifetime. (b) Electron concentration distribution in the GaAs template, assuming Schottky contact with Fe (barrier height of 0.6 eV), simulated by solving Poisson equation.

the Schottky barrier when in contact with ferromagnetic metal, and also serves as an etching stop during process for transmission measurement. The carrier distribution, band

alignment are simulated for Fe/GaAs/AlGaAs heterostructures, and the result is displayed in FIG 2.15 (b).

The procedure for preparing the GaAs substrate is the same for all the samples. A piece of GaAs (capped with thick As for protection), cleaved from the 2" template is mounted on the Ta sample holder at two corners with two pieces of Ta foil spot welded on the holder. The thermocouple is spot welded on the sample holder too, very close to the sample. For one series of sample, the same sample hole is used for consistent temperature reading. The thick As cap layer is desorbed in the buffer chamber (a separate chamber from the main MBE chamber) at substrate temperature of 380°C for 80 min. Then the substrate is transferred into the main MBE chamber, and heated up while monitoring the surface by RHEED. As the temperature increases, the RHEED pattern evolves from (1×1) to (4×4), (2×4), (4×6). We choose the (2×4) surface reconstruction, which is stable at about 430°C. (2×4) surface reconstruction is As rich surface, with the structure shown in, and the RHEED pattern along [110] and $[1\bar{1}0]$ directions are shown in FIG 2.16 (a) and (b), respectively.

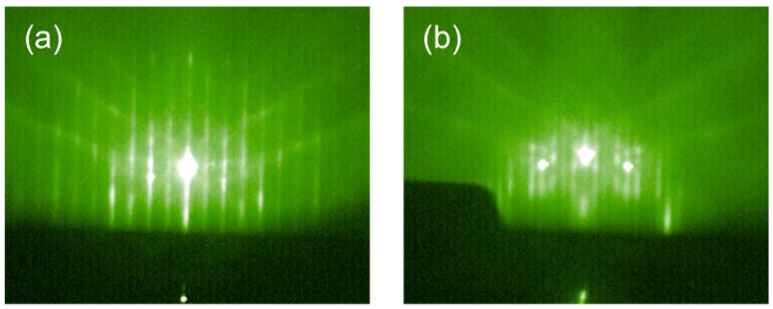

FIG 2.16 GaAs (2×4) surface reconstruction. RHEED pattern along (a) [110] and (b) $[1\bar{1}0]$.

2.4.3 Sample preparation for optical transmission measurement

After the whole heterostructures is finished in MBE chamber, the sample is etched before performing optics measurement. The whole procedure is the following: (FIG 2.17) 1. Glue the sample on a piece of sapphire, facing down, with transparent

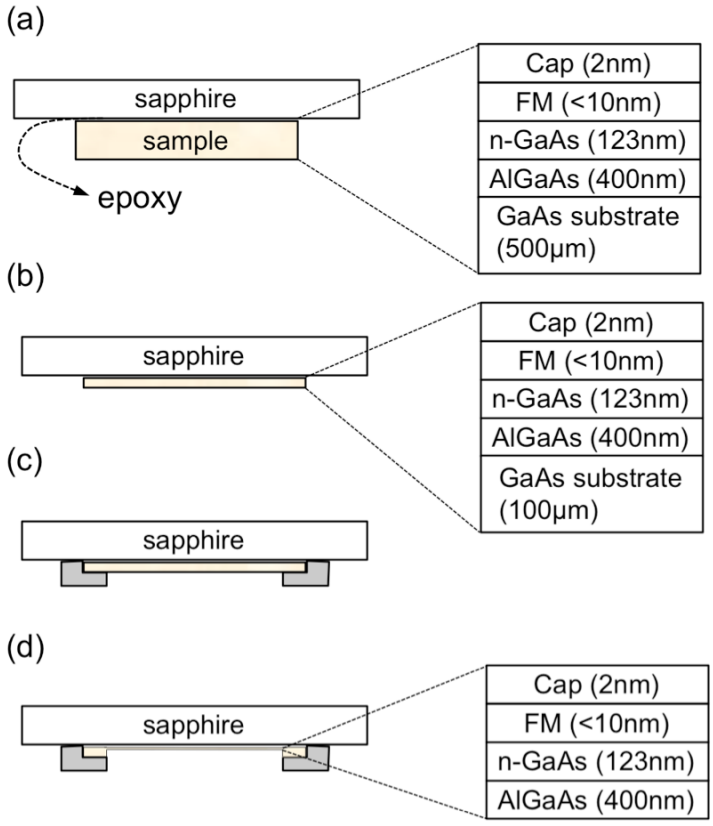

FIG 2.17 Process for preparing sample for transmission measurement.

epoxy. Wait until it dries. 2. Thin down the thick substrate to ~100μm with a polish fixture and lapping films on glass polishing pad. 3. Pattern the sample with a window open in the middle and the edges of the sample covered by photoresist or epoxy. 4. Spray etch the left ~100μm GaAs substrate. The apparatus will be illustrated in Appendix D.

The solution is $NH_4OH(29\%):H_2O_2(30\%)= 1:15$ (volume), and it takes about 20 minutes to etch away the when using nitrogen flow of 3 psi. The etching rate for AlGaAs is much lower, so it acts as an etching stopper. Once the etching finishes for the window area, flush the sample with IPA and dry it with nitrogen to prevent further etching. (The etching may not finish evenly on the sample due to uneven thickness of the film during polishing or uneven thickness of epoxy.) Sample prepared this way could last very long time (one year for sure) because the films of importance are sealed with the epoxy. More details about sample preparation are in Appendix D.

References:

[1] J. M. Kikkawa, and D. D. Awschalom, Phys. Rev. Lett. **80**, 4313 (1998).

[2] B. Beschoten *et al.*, Physical Review B **63**, 121202 (2001).

[3] J. A. Gupta *et al.*, Physical Review B **66**, 125307 (2002).

[4] S. Ghosh *et al.*, Applied Physics Letters **86**, 232507 (2005).

[5] T. Uenoyama, and L. J. Sham, Physical Review Letters **64**, 3070 (1990).

[6] F. Meier, and B. P. Zachachrenya, *Optical Orientation, Modern Problems in Condensed Matter Science* (North-Holland, Amsterdam, 1984), Vol. 8.

[7] S. A. Crooker, and D. L. Smith, Physical Review Letters **94**, 236601 (2005).

[8] C. Ciuti, J. P. McGuire, and L. J. Sham, Phys. Rev. Lett. **89**, 156601 (2002).

[9] G. E. Bauer *et al.*, Phys. Rev. Lett. **92**, 126601 (2004).

[10] J. P. McGuire, in *Physics* (University of California, San Diego, 2004), p. 99.

[11] R. K. Kawakami *et al.*, Science **294**, 131 (2001).

Chapter III

Inversion of Ferromagnetic Proximity Polarization by MgO Interlayers

3.1 Motivation

The Fe(bcc Co)/MgO(001) system with spin filtering properties were first developed theoretically [1] and experimentally [2, 3] in magnetic tunnel junctions (MTJs), and later utilized for spin injection into semiconductors [4]. Tunneling magnetoresistance of several hundreds percent at room temperature [5] has been demonstrated in MgO based MTJs, and the introduction of MgO barrier at ferromagnet/semiconductor interfaces (specifically CoFe/MgO/GaAs) also leads to greatly enhanced spin injection efficiencies. The spin filtering through MgO are due to symmetry filtering [1]. The Δ_1 states of Fe (or FeCo) only present for majority spin at the Fermi level and find matching states in MgO, leading to efficient majority spin tunneling. Other states, such as Δ_2 Δ_2' Δ_5, are low symmetry Bloch states, so contribute little in tunneling.

In principle, spin extraction (or accumulation) would also be more efficient with an extra ultrathin MgO layer, if spin extraction and spin injection experience the same scattering process. On the other hand, the details of the interfacial structure would largely affect the spin dependent reflection at the interface. Ferromagnetic proximity polarization is the optical analogue to spin extraction, and also powerful tool for characterizing the

properties of the interfaces. In this chapter, we apply FPP to study Fe/MgO/GaAs heterostructures. A naive anticipation would be that the FPP decays exponentially with MgO thickness, because MgO is an insulating barrier, and thick enough MgO would prevent the interaction of optically excited electrons interact with the Fe layer. It is also possible that due to spin filtering properties of MgO, the spin dependent reflection enhances for very thin MgO.

3.2 Growth of MgO thin film on GaAs(001) and characterization of Fe/MgO/GaAs

MgO is an often chosen buffer layer for growth of oxide films on GaAs, and there are well-documented literatures for epitaxial growth with pulsed laser deposition [6, 7], e-beam evaporation [8-10], sputtering [2], etc. The lattice constant is 4.212Å for MgO and 5.653Å for GaAs, so the lattice mismatch is 25.5%. With 45° rotation, the lattice mismatch is reduced to 5.4%. A lot of times, MgO grows cube-on-cube with GaAs(001) substrate, and the matching is 4×MgO vs. 3×GaAs (0.66%). We employ reactive MBE method for the growth of MgO [11, 12]. The starting substrate is GaAs(001) with (2×4) surface reconstruction [13]. Molecular oxygen is leaked into the MBE chamber with partial pressure of 3×10^{-7} torr, and Mg is thermally evaporated with rate of ~0.6 Å/min while the substrate is kept at room temperature. The oxidation of Mg leads to formation of MgO film, as verified by Auger spectrum [14].

The growth rate of Mg is found to be crucial for flatness of the film. With a growth rate of 1.8 Å/min, the film is very rough, as shown in FIG 3.1(a); with a reduced rate of 0.6 Å/min, the film is atomically flat as indicated in FIG 3.1(b) and (c). To oxidize

Mg sufficiently to form MgO, the growth rate should be low. Another important point is that the oxygen is leaked into the MBE chamber before shutter is open for Mg deposition.

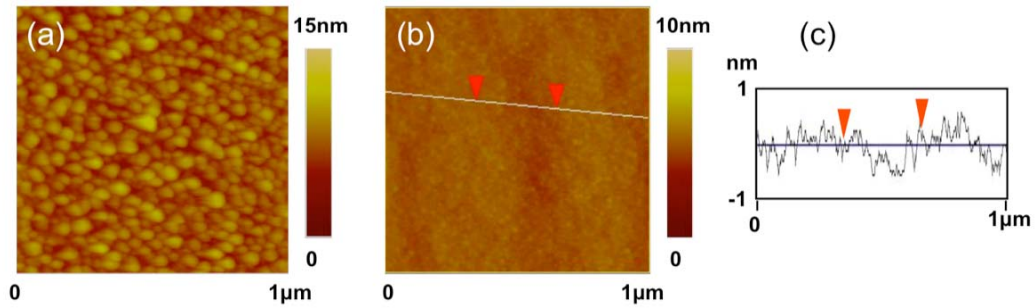

FIG 3.1 AFM images of MgO(3 nm)/GaAs(001) grown at Mg rate of (a) 1.8 Å/min and (b) 0.6 Å/min. (c) Line cut from (b).

The reason is that the initial growth of Mg on GaAs is three dimensional, due to smaller surface energy of Mg than GaAs. Leaking oxygen first assures that the Mg get oxidized as deposited, thus form flat film. The RHEED pattern of 1.5nm MgO film is shown in FIG 3.2 (a). It grows cube-on-cube on GaAs (001), concluded by comparing the line

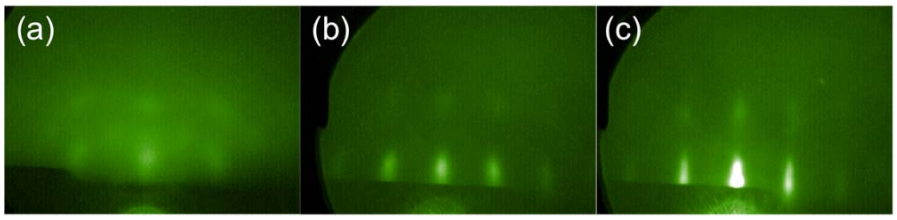

FIG 3.2 RHEED patterns of (a) 1nmMgO(1.5 nm)/GaAs(001) (b) Fe(2 nm)/MgO(1 nm)/GaAs(001) (c) Fe(2 nm)/GaAs(001) along [11bar0] direction of GaAs.

distances in the RHEED pattern of MgO with those of the GaAs RHEED pattern. Although the spots are fat, it still shows single crystalline characteristics. The RHEED pattern of Fe(2nm)/MgO(1nm)/GaAs(100) is shown in FIG 3.2 (b), and for comparison

the RHEED of Fe(2nm)/GaAs(001) is also shown as FIG 3.2 (c). These two RHEED patterns are very similar, indicating that the heterostructure is grown epitaxially.

The heterostructures are also characterized by atomic force microscopy (AFM) and longitudinal magneto-optic Kerr effect at room temperature. The AFM images of GaAs substrate, 0.5 nm MgO and 0.9 nm MgO are shown in FIG 3.3. 0.5 nm MgO film

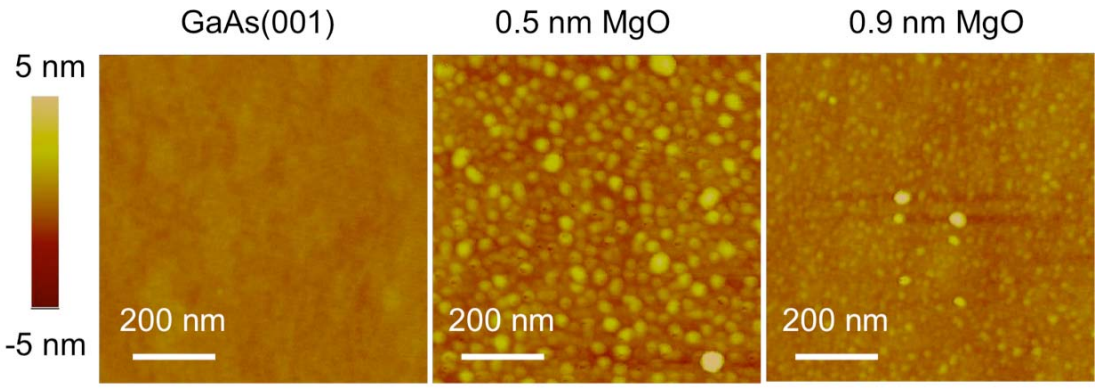

FIG 3.3 AFM images of MgO/GaAs001 with MgO thickness d = 0, 0.5, 0.9 nm, respectively.

produces relatively rough morphology, and thicker film smoothes out at 0.9 nm. This trend is consistent with the RHEED pattern evolution that the RHEED pattern disappears with initial growth and then recovers at about 1nm thickness. The hysteresis loops of the Fe film on MgO/GaAs are measured for three different thicknesses of MgO and three different in-plane orientations, shown in FIG 3.4 (a) – (c). Fe directly grown on GaAs exhibit uniaxial anisotropy, and the hard axis is along the $[1\bar{1}0]$ direction of GaAs. The deposition of MgO suppresses the magnetic anisotropy so that the hysteresis loops along all major directions are similar, and the coercivity is also smaller.

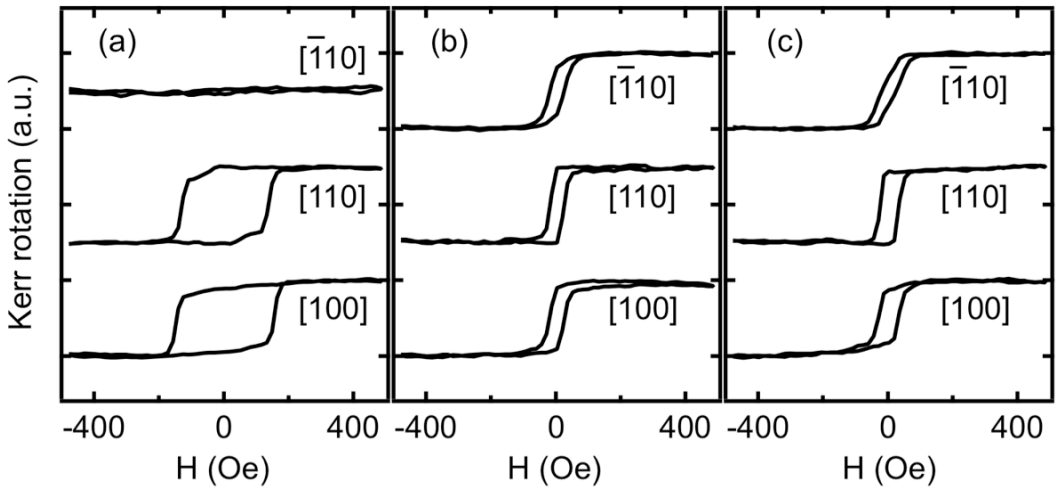

FIG 3.4 In –plane orientation dependence of longitudinal MOKE loops for Fe(2 nm)/MgO/GaAs(001) with MgO thickness (a) d = 0 nm (b) d = 0.5 nm, (c) d = 0.9 nm, respectively. Measurements are performed at room temperature and a linear background is subtracted.

3.3 FPP thickness dependence

Wedge samples with structure of Ag(2nm) cap/Fe (2nm)/MgO wedge/GaAs(001) are grown for systematic investigation of interlayer thickness dependence of FPP. All the data presented in this chapter are on two samples, A and B, with the same structure. To investigate the spin-dependent reflection in this structure, we utilize time-resolved Faraday rotation (TRFR) with unpolarized carrier excitation to directly measure the FPP.

FIG 3.5 shows representative TRFR delay scans for four different MgO thicknesses on Ag/Fe/MgO wedge/GaAs(001), sample A. The measurement is performed at T = 80 K, which provides sufficient spin lifetime while avoiding the effects of ferromagnetic imprinting of nuclear spins [15] and resonant spin amplification [16]. Here, the average pump intensity is 1000 W/cm^2. The data (open squares) and curve fits (solid

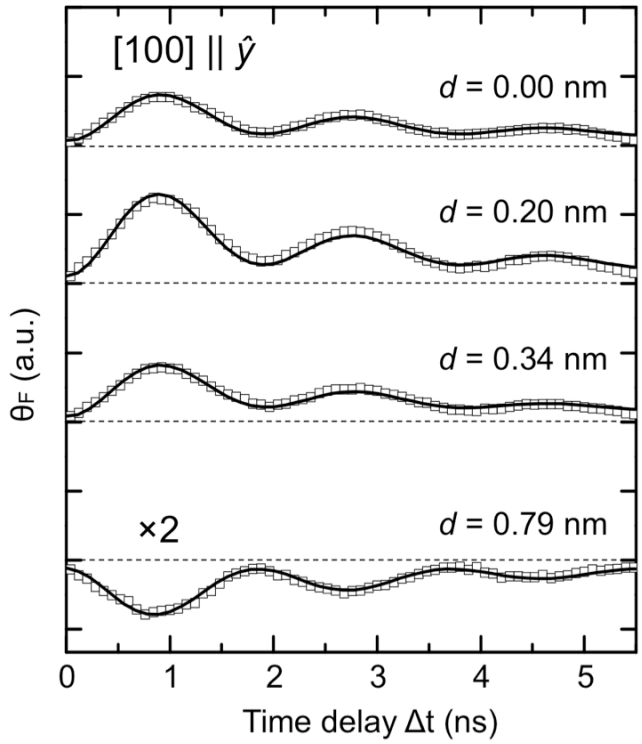

FIG 3.5 Representative TRFR delay scans for d = 0.00, 0.20, 0.34 and 0.79 nm, measured at 80 K. The open squared are the data and the solid lines are fitting curves by Eq. (2.1).

lines) exhibit oscillations in S_z that do not cross zero, consistent with the dynamics illustrated in previous chapter Section 2.2. In comparing the four curves, it is clearly seen that the FPP spin polarization is enhanced with 2.0 Å of MgO and has an opposite sign when the MgO thickness is 7.9 Å. The detailed thickness dependence is obtained by performing TRFR delay scans along the MgO wedge and fitting with equation 1. FIG 3.6 shows the thickness dependence of S_0^{FPP}, normalized by its magnitude at zero thickness.

As a function of *d*, S_0^{FPP} is initially enhanced for thickness up to ~2.0 Å, then decreases and crosses zero at ~5.0 Å. Following the sign reversal, the magnitude of S_0^{FPP} reaches its maximum at 7.0 Å, and finally vanishes above 14.0 Å. This unusual behavior has been observed consistently on four different samples.

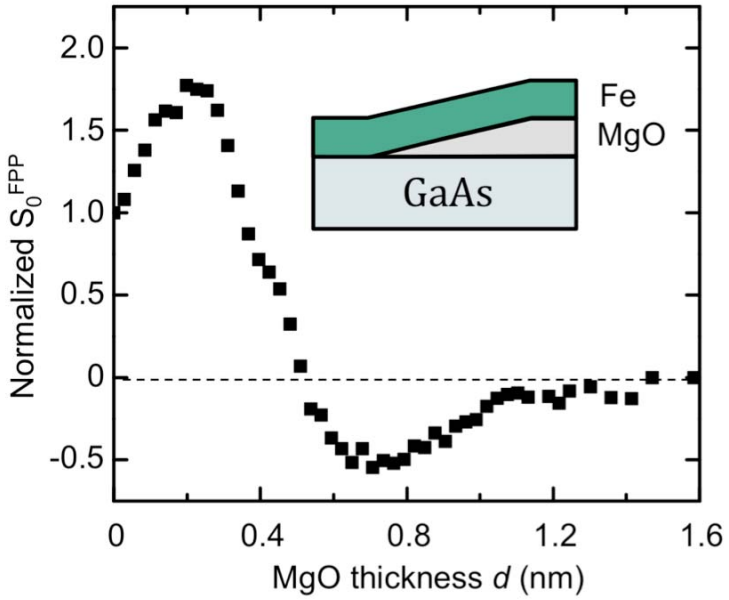

FIG 3.6 MgO thickness dependence of S_0^{FPP}, normalized by the magnitude at zero thickness. Inset: the wedge sample.

We also investigate the effect of magnetic anisotropy on the FPP signal. The sample is rotated so that the in-plane component of B_{app} aligns with the uniaxial hard axis ([$\bar{1}$10]||$\hat{y}$). In this case, the magnetization ***M*** can point away from the *y*-axis by an angle β (FIG 3.7a inset), and the TRFR signal is given by:

$$S_z = S_0^{FPP} \cos\beta \sin\alpha \cos\alpha \left[\exp(-\Delta t / T_1) - \cos(2\pi v \Delta t + \varphi_0) \exp(-\Delta t / T_2^*) / \cos\varphi_0 \right] \quad (3.1)$$

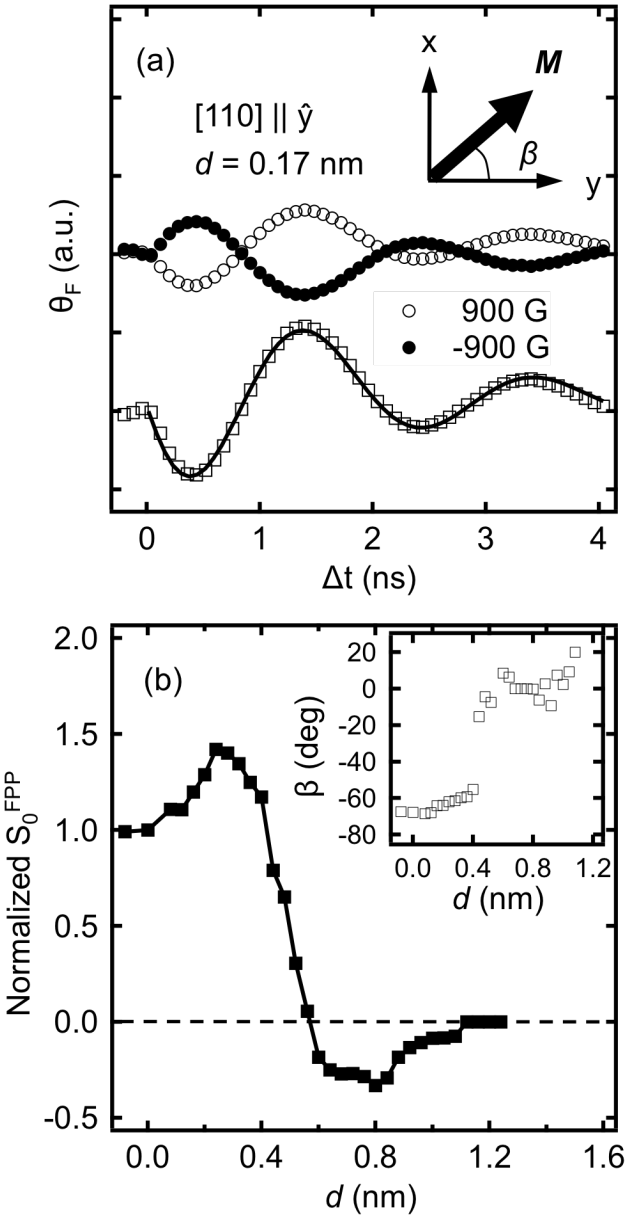

FIG 3.7 (a) TRFR curves in positive (open circle) and negative (filled circle) magnetic field. The difference of the two is represented underneath (open square). The solid lines are fitting curves. Inset: illustration of magnetization direction away from *y*-axis by an angle β. (b) S_0^{FPP} along the MgO wedge. Inset: the fitted in-plane magnetization direction β vs. MgO thickness *d*.

where φ_0 is defined by $\tan\varphi_0 = \tan\beta / \sin\alpha$. Ramping the field from B_{app} to $-B_{app}$ will reverse the longitudinal component of magnetization ($M_y \rightarrow -M_y$), and the transverse (easy axis) component can either remain the same ($M_x \rightarrow M_x$) or switch ($M_x \rightarrow -M_x$). In the former case, the quantities in equation 2 transform as ($\beta \rightarrow \pi - \beta$, $\varphi_0 \rightarrow \pi - \varphi_0$, $B_{app} \rightarrow -B_{app}$) to yield $S_z(\Delta t) \rightarrow -S_z(\Delta t)$. In the latter case, they transform as ($\beta \rightarrow \pi + \beta$, $\varphi_0 \rightarrow \pi + \varphi_0$, $B_{app} \rightarrow -B_{app}$) to yield an overall sign change and a relative phase shift. FIG 3.7 (a) shows TRFR delay scans for B_{app} = 900 G (open circles) and B_{app} = –900 G (filled circles) with d = 1.7 Å measured on sample B. Because the oscillations have opposite sign and there is no relative phase shift between the two curves, this indicates that there is no switching of the transverse magnetization ($M_x \rightarrow M_x$) and the two curves can be subtracted to eliminate background signals unrelated to FPP (open squares). Performing TRFR measurements along the MgO wedge and fitting with Eq. 3.1 determines the thickness dependence of S_0^{FPP} and β (FIG 3.7b). First, the normalized S_0^{FPP} vs. d is similar to the data for [100]$\|\hat{y}$ (FIG 3.6), even though the delay scans are rather different (i.e. S_z crossing zero in this case). Second, the magnetization angle β is ~ -60° for d < 4.0 Å and β abruptly changes to ~0° for d > 4.0 Å (FIG 3.7b inset). This result is consistent with the MOKE data (FIG 3.4) and demonstrates a new method for characterizing magnetic anisotropy in FM/GaAs systems.

3.4 Nuclear field measurement of FPP

FIGs 3.8 (a)-(c) show the lab time dependence of the TRFR delay scans at 6 K with B_{app} = 900 G on sample A for d = 0.17 nm, 0.48 nm, and 0.85 nm, respectively

(beams blocked before measurement). Because ν is proportional to $B_{app} + B_n$ and B_{app} is constant, the lab time dependence of ν (FIG 3.8d) is due to nuclear polarization, which

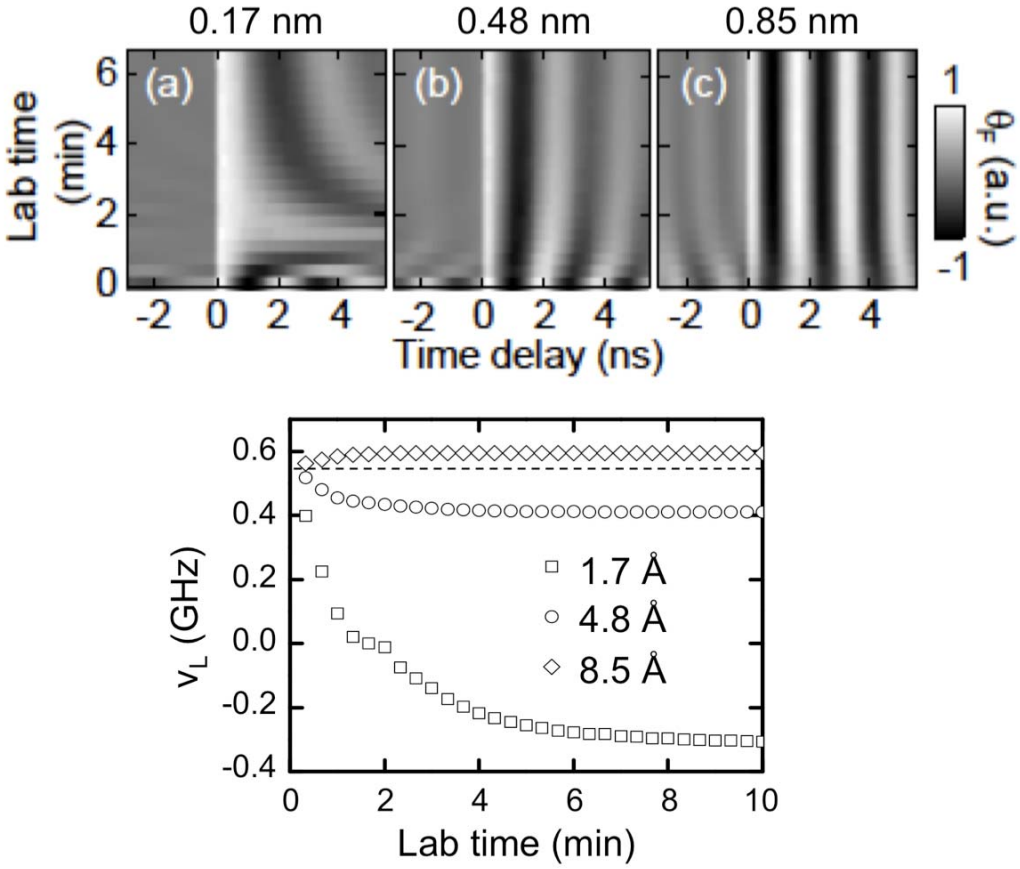

FIG 3.8 TRFR Larmor magnetometry of nuclear spin polarization, measured at 6 K. (a)-(c), Lab time dependence of the TRFR time delay scans for d = 0.17, 0.48, and 0.85 nm, respectively. (d) Spin precession frequency vs. lab time for the according thicknesses.

reaches steady-state after several minutes. FIG 3.9 shows the steady-state ν and corresponding B_n values as a function of MgO thickness. As a function of d, the nuclear field has an initial value of $B_n(0\ Å) = -770$ G, decreases to a minimum value of $B_n^{min} = -1400$ G at $d \sim 2.0$ Å, crosses zero to reach a maximum value of $B_n^{max} = 76$ G at $d \sim 9.0$ Å,

and vanishes above 14.0 Å. Because the g-factor of GaAs is negative, a positive S_0^{FPP} will generate a negative B_n. Thus, the nuclear field measurement, B_n vs. d, reflects the

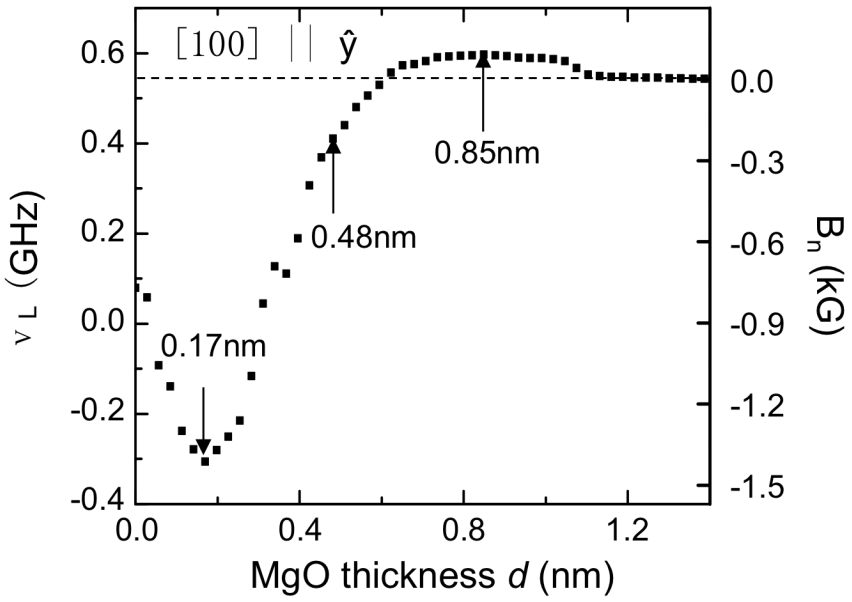

FIG 3.9 MgO thickness dependence of steady-state frequency and corresponding nuclear field B_n. The result is consistent with the direct FPP measurement.

same behavior as the direct measurement of S_0^{FPP} vs. d (FIG 3.6), namely an enhancement of FPP followed by a sign reversal. In our sample set, the observed values for the nuclear field parameters [B_n(0 Å), B_n^{min}, B_n^{max}] are [-770, -1400, 76], [-1555, -2726, 69], [-409, -770, 239] and [-257, -450, 167] in units of Gauss.

FIG 3.10 (a) shows the time delay scans after saturation at 6 K along the MgO wedge on sample B, with two dimensional image plot. The fitted frequency vs. MgO thickness curve is displayed in FIG 3.10 (b) (black curve). It is clearly seen that the result

is very similar to that on sample A. One thing to notice is that the spin lifetime has a correlation with nuclear field: spin lifetime is short (no negative time delay signal) when

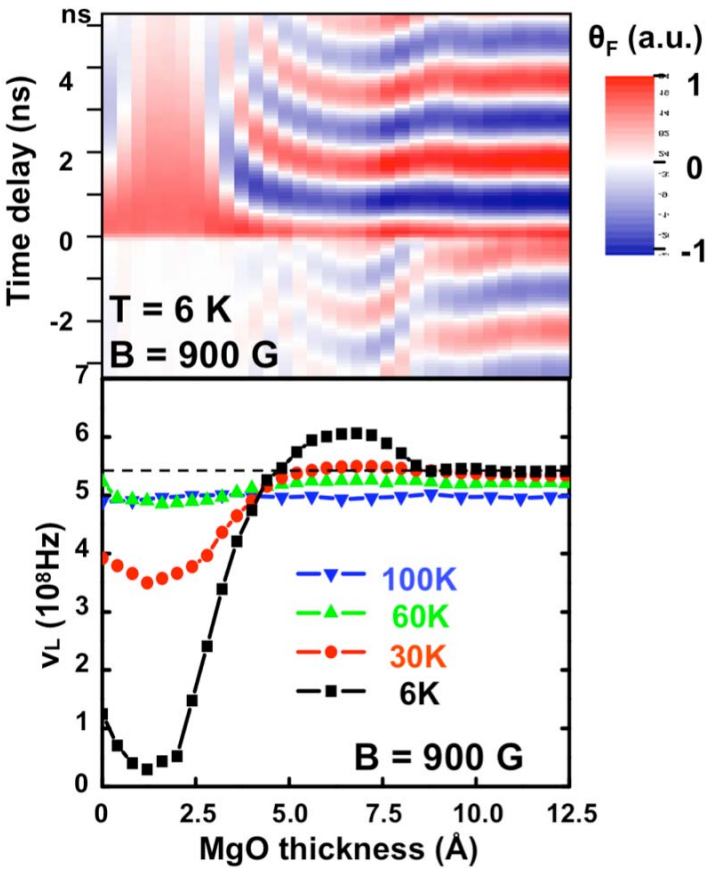

FIG 3.10 (a) TRFR scans along the MgO wedge at 6 K plotted as a function of time delay and and MgO thickness. (b) The steady state precession frequency as a function of MgO thickness at 6 K, 30 K, 60 K, and 100 K. The 6 K data is extracted from the TRFR scans shown in (a). The curves for other temperatures follows the same procedure.

large nuclear field is present. It is consistently observed all the time. We also measure the nuclear field change with temperature, curves for T = 30 K, 60 K, and 100 K are also shown in FIG 3.10 (b). The nuclear field decreases as temperature increases, and it is

almost zero at 100 K. Nevertheless, the shape of the MgO thickness dependence curve does not change, indicating that the thickness dependence is from nuclear field changing, other than artificial effect like strain in the wedge sample. The slight shifting of the Lamor frequency at high MgO thicknesses is due to the temperature dependence of the g-factor [17].

3.5 Intensity dependence

We employ the nuclear field measurement for laser intensity dependence study. FIG 3.11 shows the wedge scans on sample B with different pump powers, 0.4, 0.6, 4.0 and 7.5 mW. For low pump intensities (0.4 and 0.6 mW), the nuclear field is almost zero in higher MgO thickness region (0.5 ~ 0.8 nm), while it is non-zero in the low thickness

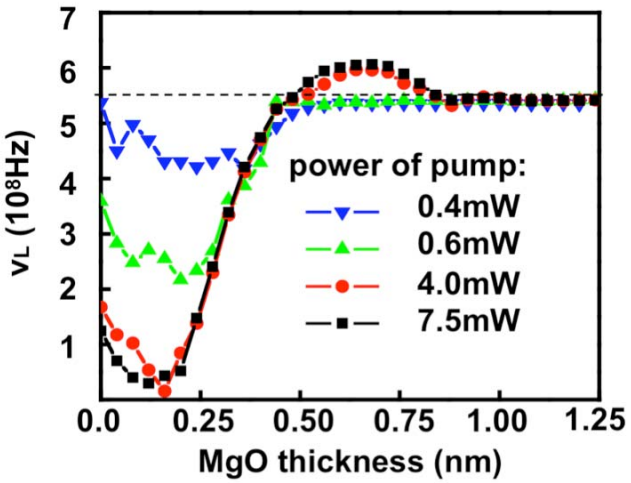

FIG 3.11 Intensity dependence of B_n for Fe(2 nm)/MgO wedge/GaAs.

region (< 0.5nm). This indicates that for different MgO thicknesses, the turn-on pump intensities are different. So we do intensity dependence measurement of the nuclear field

B_n at various MgO thicknesses on sample A (results on sample B are similar), shown in FIG 3.12. For d = 0.17 nm, a threshold for a strong negative contribution to B_n is

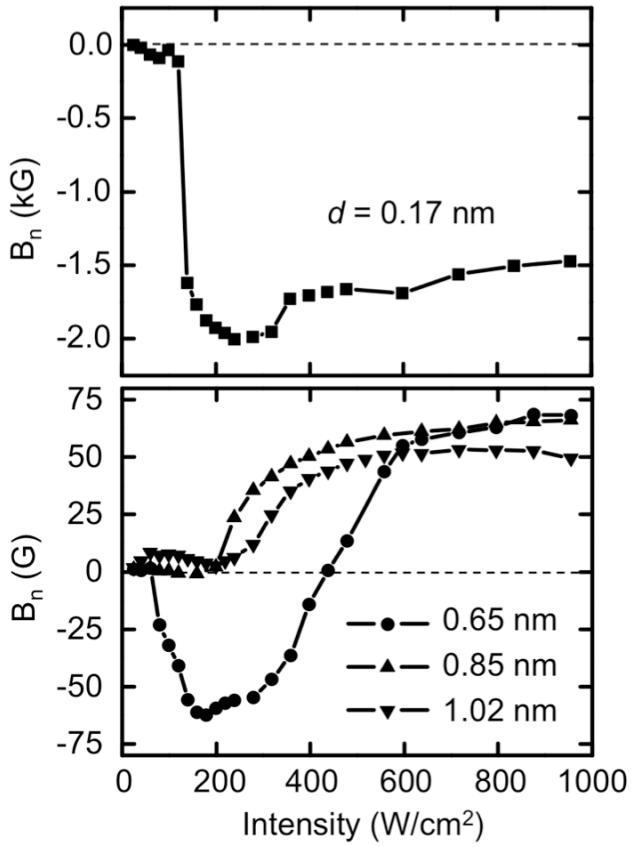

FIG 3.12 Intensity dependence of B_n for Fe(2 nm)/MgO/GaAs with MgO thickness d = 0.17, 0.65, 0.85 and 1.02 nm.

observed at ~120 W/cm^2 and a threshold for a weak positive contribution to B_n is observed at ~370 W/cm^2. For d = 0.65 nm, the two thresholds are observed again, but in this case the positive B_n contribution dominates at high intensities. For d = 0.85 nm and 1.02 nm, only the positive contribution to B_n is observed. Thus, the negative contribution

to B_n dominates for lower MgO thickness and the positive contribution to B_n dominates for higher MgO thickness. The presence of two thresholds suggests that the sign change in FPP is a result of two competing processes that yield opposite signs for FPP (e.g. low vs. high tunnel barrier, bulk vs. surface states) and not a result of oscillations due to quantum interference in the MgO layer.

3.6 Pure Mg sample

The sample leads to the origin of the sign reversal is the sample with pure Mg interlayer (i.e. Fe(20 Å)/Mg(5.0 Å)/GaAs), and the intensity dependence of B_n is shown in FIG 3.13 (a). B_n exhibits two thresholds, becoming slightly negative at low intensity and positive for intensity above 300 W/cm^2. The positive nuclear field is even much larger than the maximum value observed in Fe/MgO wedge/GaAs structures. Thus, the Mg plays an important role in producing the sign reversal of FPP. A wedge Mg sample is also made with the structure of Fe(2 nm)/Mg wedge/GaAs, the direct FPP measurement result is shown in FIG 3.13 (b). The dependence of FPP on Mg thickness increases shows a sign reversal at ~0.3 nm, but there is no initial enhancement near zero thickness as observed for the MgO wedge. The magnitude of the negative FPP is about half of the zero thickness FPP, a much higher ratio than that for the MgO wedge sample. Further investigation on uniform thickness MgO samples indicates that while the FPP inversion is reproduced, the initial enhancement of FPP for d = 0 – 0.2 nm is due to the wedge growth. During MgO wedge growth, regions of the sample with zero (or very low) MgO thickness have the GaAs surface exposed to oxygen gas during the entire growth, while the other regions are quickly covered by MgO to limit the oxidation of the GaAs. On

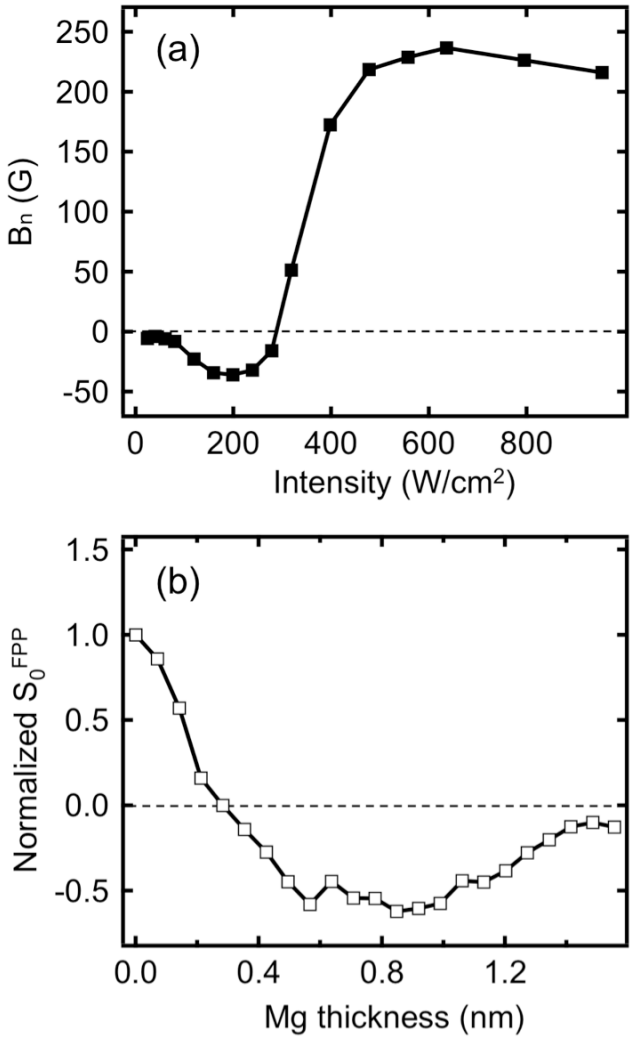

FIG 3.13 (a) Intensity dependence of nuclear field on Fe(2 nm)/Mg(0.5 nm)/GaAs. (b) FPP measurement on Fe(2 nm)/Mg wedge/GaAs.

Fe/GaAs samples, we find that the effect of GaAs surface oxidation is to reduce the FPP. Thus, the initial enhancement of FPP results from variations in GaAs surface oxidation along the MgO wedge. The nuclear field measurement on the same Mg wedge sample is shown in FIG 3.14 (a), which is consistent with the direct measurement. The little difference is that for small Mg thickness, the nuclear field is very small, whereas in the

FPP measurement it gradually decreases with Mg thickness.

Furthermore, additional Mg wedge samples, including bcc-Co(2 nm)/Mg/GaAs

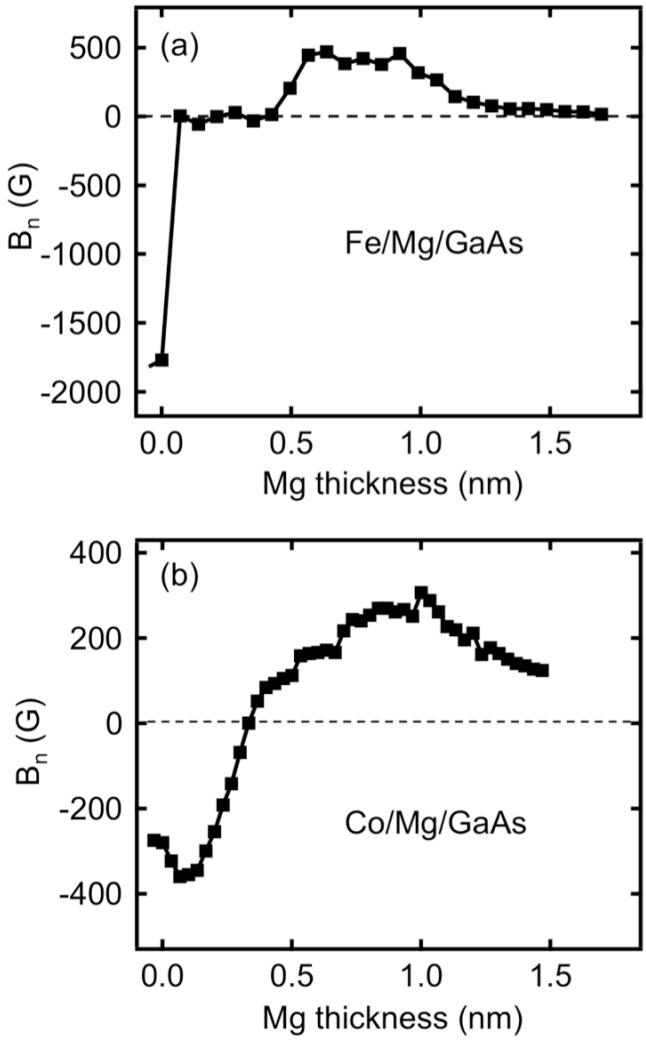

FIG 3.14 Nuclear field measurement on (a) Fe(2 nm)/Mg wedge/GaAs and (b) Co(2 nm)/Mg wedge/GaAs.

(FIG 3.14b) and Fe(2 nm)/Mg wedge/GaAs(with high surface doping) (not shown), all show FPP sign reversals with Mg thickness. In addition, the wedge sample of Fe(2 nm)/MgO wedge (e-beam grown, considered less oxygen deficiencies)/GaAs does not

show sign reversal, and the FPP just decays with MgO thickness and reaches zero in 1 nm thickness. These results points out unambiguously that Mg is the key factor that leads to the sign reversal in FPP.

3.7 Origin of sign change

Factors affecting the overall sign of FPP have been investigated theoretically [18, 19]. Sham and co-workers find that the sign of FPP can be changed by adjusting the Schottky barrier height [18]. Bauer and co-workers find that the sign of FPP depends on interfacial disorder [19, 20]. The FPP sign change may also be due to quantum interferences related to complex wavevectors in the MgO interlayers [1, 3]. In related studies on biased Fe/GaAs structures, a sign change in the spin accumulation has been observed as a function of bias voltage [21]. Two proposed explanations are: (1) localized vs. extended states in the GaAs layer [22], and (2) majority-spin bulk states of Fe vs. minority-spin surface states of Fe [23].

The results on Mg interlayer samples suggest that the inversion of FPP in the MgO structures is related to the interfacial bonding (i.e. Fe-GaAs, Fe-Mg), as opposed to MgO barrier height effects or quantum interferences in the MgO layer. We provide two hypothetic pictures with the same origin in this regard. First, Mg bonding with Fe could change the local polarization of Fe. With MgO/Mg interlayer, the interface is more disordered, leading to strong in-planar bonding between Fe and GaAs via d_{xy} orbital [22]. Thus it opens a transmission channel for $\Delta_{2'}$ band of the minority states. In principle, all the d_{z^2} orbital of Fe form σ-bond with GaAs *s* orbital, which leads to perfect spin

injection [24, 25]. In the real cases, the interface disorder is inevitable and the spin polarization drops dramatically. As Ref [22] pointed out, the Fe substitutes at the As-terminated monolayer may lead to strong d_{xy} bonding with GaAs, the ultrathin Mg layer could change the bonding between Fe and GaAs in the same manner. Recalling the analysis of FPP in Chapter 2, the FPP is positive when minority electrons are reflected more than majority electrons ($|r_-|^2 - |r_+|^2 > 0$). The transmission channel for $\Delta_{2'}$ band of the minority states would possibly change the spin reflection so that the minority electrons are mostly transmitted and $|r_-|^2 - |r_+|^2 < 0$, thus the FPP sign reversal.

Second, the interfacial bonding with Mg could be understood in the perspective of Schottky barrier height. The Schottky barrier height is determined by $\Phi_B = \phi_M - \chi_S$ (FIG 3.15), regardless of the Fermi level pinning [26, 27], where ϕ_M is the work function of

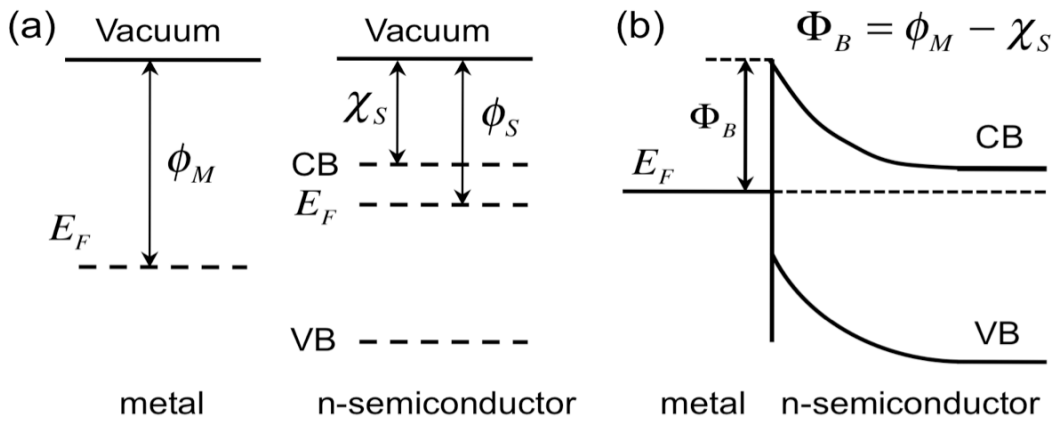

FIG 3.15 Schottky barrier at metal/n-semiconductor contact. (a) Work function of the metal (ϕ_M), electron affinity (χ_S) and work function (ϕ_S) of semiconductor before contact. (b) Schottky barrier (Φ_B).

the metal, and χ_S is the electron affinity of the semiconductor. The work functions for Fe and Mg are ϕ_{Fe} = 4.5 eV and ϕ_{Mg} = 3.7 eV, respectively. The much lower work function of Mg would possibly result in a low Schottky barrier height. As analyzed in Chapter 2, the low Schottky barrier (Fe/Mg/GaAs) has opposite sign of FPP comparing to high Schottky barrier height case (bare Fe/GaAs) for low doping region (7×10^{16}/cm^3). This picture could also explain the intensity dependence, where there is a sign change with pump intensity at medium MgO thickness. We consider that the excitation of the electron carriers can lower the Schottky barrier [19] in certain amount, and the effect is shown as sign change when the presence of Mg already reduces the Schottky barrier to a value close to the critical value for sign change.

Further studies are needed for a complete understanding of spin dependent processes, such as reflection and transmission, tunneling under bias, in the Fe/MgO(Mg)/GaAs heterostructures. The combination of MgO as a real spin filtering tunnel barrier and Mg as a low work function material to adjust the Schottky barrier height, should give a broad range of tunability in terms of resistance area product (RA product) for efficient spin injection and detection.

References:

[1] W. H. Butler *et al.*, Phys. Rev. B **63**, 054416 (2001).

[2] S. S. P. Parkin *et al.*, Nature Materials **3**, 862 (2004).

[3] S. Yuasa *et al.*, Nature Materials **3**, 868 (2004).

[4] X. Jiang *et al.*, Phys. Rev. Lett. **94**, 056601 (2005).

[5] S. Yuasa *et al.*, Appl. Phys. Lett. **89**, 042505 (2006).

[6] E. J. Tarsa *et al.*, Journal of Applied Physics **73**, 3276 (1993).

[7] C. MartÌnez Boubeta *et al.*, Journal of Crystal Growth **226**, 223 (2001).

[8] L. D. Chang *et al.*, Applied Physics Letters **60**, 1753 (1992).

[9] L. S. Hung, L. R. Zheng, and T. N. Blanton, Applied Physics Letters **60**, 3129 (1992).

[10] M. Hong *et al.*, in The 15th North American conference on molecular beam epitaxy (AVS, College Park, Maryland (USA), 1996), pp. 2297.

[11] S. Yadavalli, M. H. Yang, and C. P. Flynn, Physical Review B **41**, 7961 (1990).

[12] S. W. Robey, Journal of Vacuum Science & Technology A: Vacuum, Surfaces, and Films **16**, 2423 (1998).

[13] E. M. Kneedler *et al.*, Physical Review B **56**, 8163 (1997).

[14] Y.-F. Chiang, in *Physics* (University of California, Riverside, 2008), p. 104.

[15] R. K. Kawakami *et al.*, Science **294**, 131 (2001).

[16] J. M. Kikkawa, and D. D. Awschalom, Phys. Rev. Lett. **80**, 4313 (1998).

[17] M. Oestreich, uuml, and W. W. hle, Physical Review Letters **74**, 2315 (1995).

[18] C. Ciuti, J. P. McGuire, and L. J. Sham, Phys. Rev. Lett. **89**, 156601 (2002).

[19] G. E. Bauer *et al.*, Phys. Rev. Lett. **92**, 126601 (2004).

[20] G. E. W. Bauer *et al.*, Physical Review B **72**, 155304 (2005).

[21] X. Lou *et al.*, Nature Phys. **3**, 197 (2007).

[22] H. Dery, and L. J. Sham, Phys. Rev. Lett. **98**, 046602 (2007).

[23] A. N. Chantis *et al.*, Physical Review Letters **99**, 196603 (2007).

[24] J. M. MacLaren *et al.*, Physical Review B **59**, 5470 (1999).

[25] O. Wunnicke *et al.*, Physical Review B **65**, 241306 (2002).

[26] R. T. Tung, Physical Review Letters **84**, 6078 (2000).

[27] R. T. Tung, Physical Review B **64**, 205310 (2001).

Chapter IV

Oscillatory Spin Polarization and Magneto-optic Kerr Effect in Fe_3O_4 Thin Films on GaAs

4.1 Motivation

Magnetite (Fe_3O_4) is an attractive material for spin injection and detection, because theory predicts complete spin polarization at the Fermi level (i.e. half metal) at room temperature [1, 2]. The large negative spin polarization (55% - 80%) has been measured by spin-resolved photoemission experiment [3, 4] and confirmed by transport measurement based on magnetic tunnel junctions [5]. Following the successful growth of Fe_3O_4 thin films on GaAs [6], the recent demonstration of spin injection establishes Fe_3O_4 as an important material for semiconductor spintronics [7].

One interesting aspect of magnetic thin films and multilayers is the confinement of electron waves to form quantum well (QW) states. Because the QW states are spin-polarized, this produces oscillatory interlayer magnetic coupling [8, 9] and modulates magnetic properties such as the magnetic anisotropy[10] and magneto-optic Kerr effect (MOKE) [11, 12]. Fe_3O_4 is particularly appealing in this regard because its relatively low carrier density (~ 10^{21} cm^{-3}) compared to metals and large spin polarization should lead to strong modulation of spin dependent properties that could be tuned by electrostatic gates.

While evidence for quantum confinement in Fe_3O_4 has been reported for thin films [13] and nanoparticles [14], their effect on spin dependent properties has not been established.

4.2 Basic properties of Fe_3O_4

Magnetite is theoretically predicted to be a half metal [1, 2], with Curie temperature of 858K. The crystal structure of Fe_3O_4 is inverse spinel AB_2O_4 structure (FIG 4.1), and the lattice constant is 8.396 Å. The O^{2-} ions form an fcc sublattice with tetrahedral (A site) and octahedral (B site) interstitial sites. Fe^{3+} ions with $5\mu_B$ magnetic moment are located on A sites as well as half of the B sites, and the remaining half of B sites are occupies by Fe^{2+} with $4\,\mu_B$ magnetic moment. The A and B sites magnetic

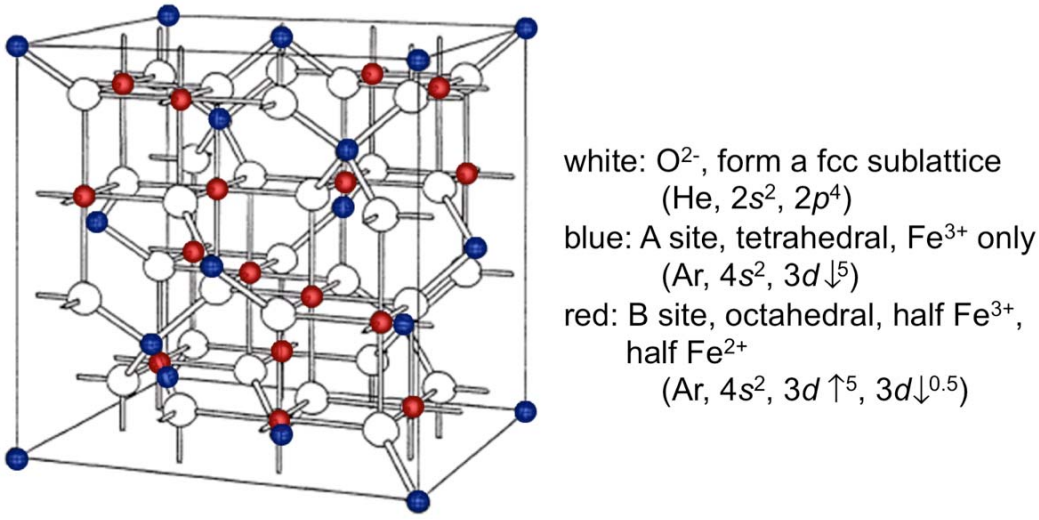

FIG 4.1 Crystal structure of Fe_3O_4: inverse spinel structure. Adapted from http://www.ruf.rice.edu/~natelson/research.html. On the right side, in the parenthesis are electron configuration of the according atoms.

moments show antiferromagnetic ordering, thus the total magnetic moment of Fe_3O_4 is $4\mu_B$/formula unit. The good conductivity (in order of $100(\Omega \bullet cm)^{-1}$) of Fe_3O_4 at RT is from hopping of the 'extra' electron of all Fe^{2+} ions at B sites [15, 16].

Density functional method with local spin density approximation is widely used for calculation of the electronic structure of magnetite [1, 2]. For the high temperature phase (above Verwey transition), only the minority states are present at the Fermi level. In the majority bands, the 3d states of B site Fe are completely filled and the 3d states of A site Fe are unoccupied. In the minority bands, the 3d states of A site are filled and the 3d states of B site are partially filled. So the states at the Fermi level are the t_{2g} states of B site Fe [2]. Experimentally, spin-resolved photoemission has been used to determine the spin polarization at the surface [3, 4, 17]. The spin polarization was found to depend on the orientation of the Fe_3O_4 surface. Negative (80±5)% spin polarization at the Fermi level has been measured on the Fe_3O_4 (111) surface, and only –(55±10)% was measured on the (100) surface [17]. The much lower spin polarization on the (100) surface was explained by changes in electronic states due to surface reconstruction (evidence from scanning tunneling microscopy), which was also supported by the density functional theory calculation [4, 17].

Magnetite is a highly correlated electronic material, exhibiting an interesting metal-insulator transition at temperature about 120K, called Verwey transition [15]. Upon cooling below 120K, the resistivity of bulk magnetite decreases by two orders of magnitude, accompanied with changing of the crystal structure from cubic to monoclinic symmetry [18] and decrease in magnetization [19, 20]. In early time, Verwey et al.

proposed that this transition is caused by charge ordering of B site Fe ions, with Fe^{2+} and Fe^{3+} ions forming (001) planes alternating in [001] direction [15, 16, 21]. Later the structure characterization by neutron scattering [18] and x-ray diffraction [22] disproved the Verwey charge ordering model. However, the experimental evidence for exactly displacement of atoms is still lacking so far, which has led to controversial models about the charge ordering [23-27]. In magnetite thin films (< 50 nm), it is commonly observed that the Verwey transition is suppressed [19, 28].

Other iron oxides include FeO (wüstite), α-Fe_2O_3 (hematite), γ-Fe_2O_3 (maghemite). α-Fe_2O_3 is antiferromagnetic, and γ-Fe_2O_3 is ferromagnetic [29].

4.3 Growth of Fe_3O_4 on GaAs(001)

There are usually two ways of MBE growth for Fe_3O_4, post oxidation of the Fe single crystal film [3, 6, 30, 31], and depositing Fe in oxygen environment [32-34]. We adopt the post oxidation method to avoid unnecessary oxidation of the substrate and the interface. Before the growth of Fe_3O_4, the As is desorbed to produce the standard (2×4) surface reconstruction. Fe single crystal film is obtained by thermal evaporation of Fe while keeping the substrate at RT, and chamber pressure is below 8e-10 torr. The RHEED patterns are shown in FIG 4.2 (a) and (b). Then the oxygen is leaked into the vacuum chamber until the chamber pressure reaches 5×10^{-7} torr, and the sample is heated up to 175 °C for the formation of Fe_3O_4. The RHEED pattern evolves from Fe streaks into a typical Fe_3O_4 RHEED pattern within 3 minutes after reaching 175 °C. FIGs 4.2 (c) and (d) show the corresponding RHEED patterns along the [110] and [010] in-plane directions of GaAs after 30 min of oxidation, indicating epitaxial growth of Fe_3O_4 (10 nm)

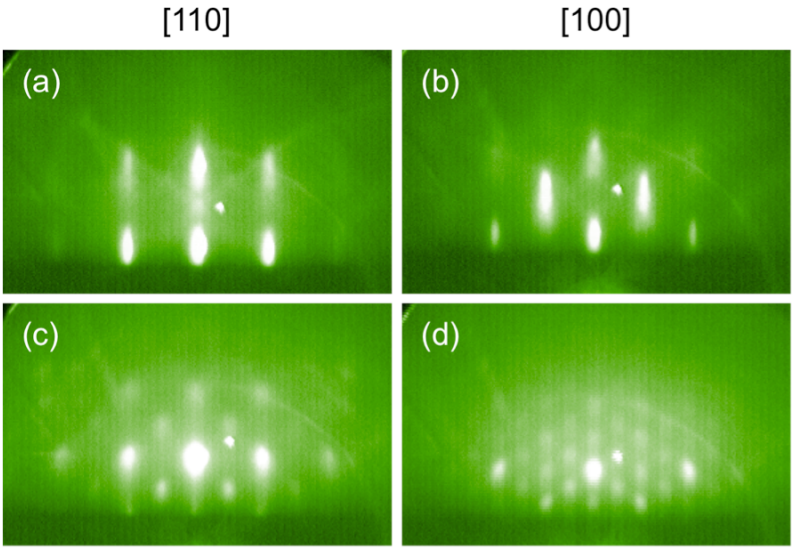

FIG 4.2 RHEED patterns of (a), (b) Fe(5 nm)/GaAs(001) and (c), (d) Fe_3O_4(10 nm)/GaAs(001), along directions of [110] and [100] of GaAs.

on GaAs. We assume the Fe is completely oxidized and 1 nm of Fe corresponds to 2.086 nm of Fe_3O_4.

Two important factors that determine the film quality and interface quality are oxygen pressure and oxidation temperature (growth temperature). We compare the two growth methods from literature. Post oxidation of Fe films to form Fe_3O_4 works very well for thin film (< 10 nm). The substrate temperature during oxidation is from 225°C [6] to 427°C [31], and higher temperature could mess up the interface. The oxygen pressure varies from one group to another, from 5×10^{-7} torr [30] to 5×10^{-5} torr [6]. With the latter method, thick Fe_3O_4 film could be achieved. Even for the depositing Fe in oxygen method, initial seed layer growth using the oxidation method was employed [33]. Regarding the oxygen pressure, almost every group got Fe_3O_4, not Fe_2O_3, even with

oxygen pressure of 5×10^{-5} torr using the post oxidation method, where the identification of Fe_3O_4 is usually X-ray photoelectron spectroscopy (XPS). One group showed that high oxygen pressure, 4×10^{-6} torr, leads to the formation of γ-Fe_2O_3, with the method of depositing Fe in oxygen at 300°C. It is possible that the post oxidation is not as reactive as evaporating Fe in oxygen, so the pressure or temperature could go higher and it still forms Fe_3O_4. We choose 5×10^{-7} torr, a relatively low pressure, so the growth of Fe_3O_4 is assured. The magnetization of $4.1\mu_B/Fe_3O_4$ and suppressed Verwey transition also proves that the film we grow is Fe_3O_4, not other forms of iron oxides (FIG 4.4).

To study how the temperature affects the film quality, we make Fe_3O_4 films at several temperatures, 100°C, 175°C, 225°C and 275°C. The RHEED patterns are shown in FIG 4.3. The 100°C one resemble the RHEED of the Fe/GaAs, so the oxidation is not

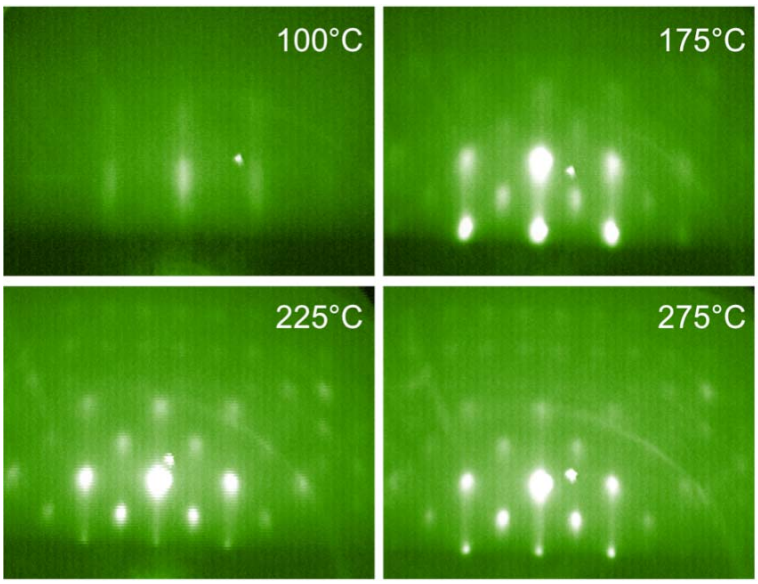

FIG 4.3 RHEED patterns of Fe_3O_4(10 nm)/GaAs(001) oxidized at different temperatures, along [110] direction of GaAs.

effective enough. When the temperature is above 175°C, the RHEED pattern are typical Fe_3O_4 RHEED patterns. Higher temperature gives a little sharper RHEED pattern. The growth temperature we use (175°C) is low comparing to other work, and low temperature is generally good for achieving sharp interface. Later in the FPP measurement, we will see that the quality of the interface is highly sensitive to the oxidation temperature, which is not necessarily reflected in the RHEED pattern.

We also try growing Fe_3O_4 film by depositing Fe in oxygen. It does not work without Fe seed layer. It is likely that for growing Fe_3O_4 film on oxide substrates such as MgO, $BaTiO_3$, the Fe seed layer is not necessary; growing on GaAs (InAs) requires Fe seed layer for preventing oxidation of the substrate or formation of other phases. We also tried the method of Fe + O_2 following initial growth by post oxidation, and the RHEED pattern keeps the sharp features as the film grows thicker (up to 20 nm). So in this way, it is possible to grow very thick Fe_3O_4 film. Another issue very common for Fe_3O_4 growth is the formation of antiphase boundary [35, 36]. When the growth material has crystal structure of lower symmetry than the substrate (i.e. Fe_3O_4 on MgO substrate), the antiphase boundaries are formed when two neighboring islands coalesce. This is not an issue for GaAs substrate, because the surface reconstruction lowers the symmetry of the surface.

We also noticed that the order of leaking oxygen and increasing the substrate temperature has an effect on the quality of the film. Leaking oxygen first and then increase the temperature results in better quality in terms of RHEED pattern and magnetization value close to $4\mu_B/Fe_3O_4$. Leaking oxygen takes about 30 sec, and right

after the oxygen pressure reaches the desired value, we set the substrate temperature to 175°C, with ramping rate of 15°C/min. The oxidation time we refer starts after the substrate temperature reaches the set value.

4.4 Magnetic characterization of Fe_3O_4 thin film on GaAs(001)

The magnetic properties of the Fe_3O_4 films are characterized by longitudinal MOKE and vibrating sample magnetometry (VSM). FIG 4.4 (a) shows the hysteresis loop of Fe_3O_4 (10 nm) measured at 80 K along the [110] in-plane direction of GaAs, and other directions show almost identical magnetic behavior. The magnetization measured by VSM at RT is 4.1±0.1 Bohr magnetons (μ_B) per Fe_3O_4 formula unit (FIG 4.4 (a) inset). The square hysteresis loop with magnetization value close to the ideal value of $4\mu_B/Fe_3O_4$ [1, 2] indicates the high quality of the film, large magnetic domains, and the absence of antiphase boundaries [35, 36]. FIG 4.4 (b) shows the temperature dependence of the remanent magnetization as determined by the MOKE measurement. Upon cooling from RT to 4 K, the magnetization increases slightly as typical of ferrimagnetic behavior. There is a small decrease in magnetization as the sample is cooled below 120 K, which is an indication of Verwey transition. This largely suppressed Verwey transition has also been observed in previous studies of ultrathin Fe_3O_4 films (< 50 nm) [19, 28].

From the hysteresis loops measured at different temperatures (FIG 4.5a), we also notice a little antiferromagnetic shifting of the hysteresis loop at low temperatures (below 80 K). This is probably due to the formation of very thin antiferromagnetic α-Fe_2O_3 on the top of Fe_3O_4 film. Films grown at higher temperatures are also measured with MOKE.

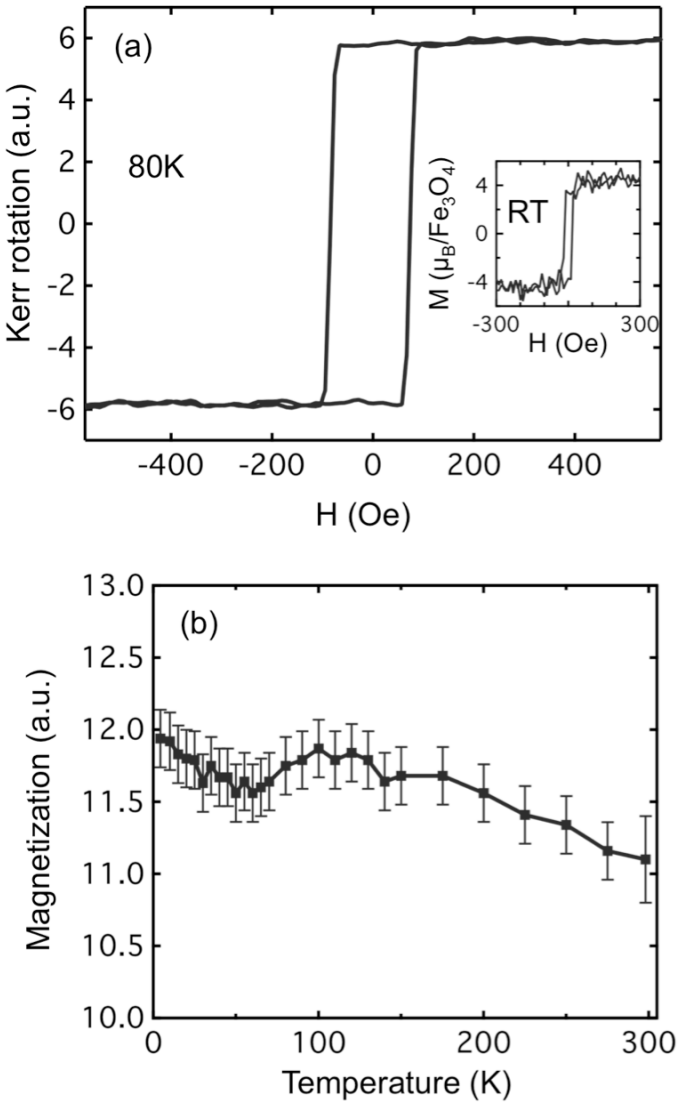

FIG 4.4 (a) Hysteresis loop measured by longitudinal MOKE at 80 K. inset: VSM. (b) Remanent MOKE vs. temperature.

The hysteresis loop of the Fe_3O_4 film grown at 275°C (FIG 4.5b) is not square, and the magnetization value is much less than $4\mu_B/Fe_3O_4$. If we choose $4\mu_B/Fe_3O_4$ as a criterion for best quality film, it is obvious that the 175°C is the best growth temperature.

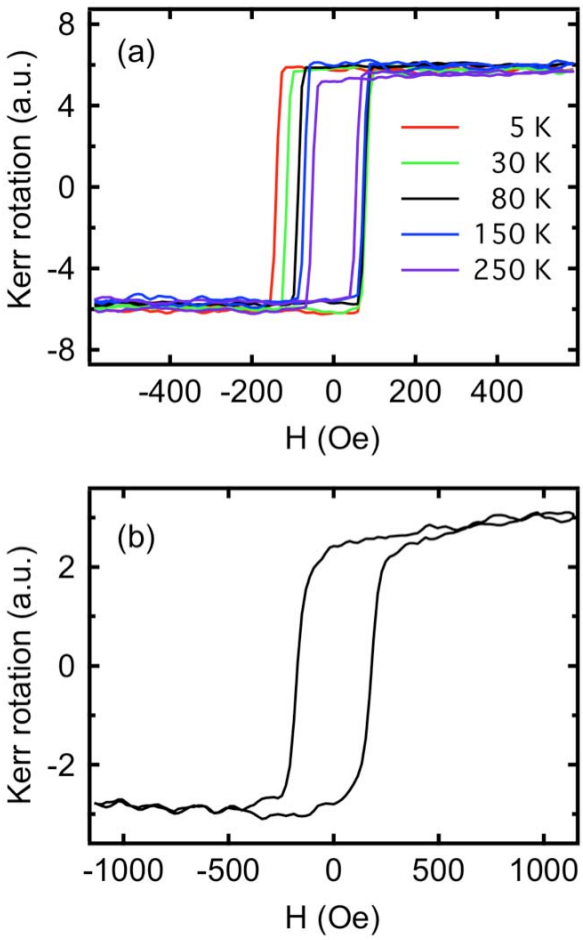

FIG 4.5 (a) Hysteresis loop measured by longitudinal MOKE on Fe_3O_4 grown at 175°C, at different temperatures. (b) Hysteresis loop measured on Fe_3O_4 film grown at 275°C, at room temperature.

4.5 Ferromagnetic proximity polarization on Fe_3O_4/GaAs heterostructures and the influence of oxidation temperature

FIGs 4.6 (a) and (b) show TRFR curves on Fe(4 nm)/GaAs and Fe_3O_4(8 nm)/GaAs prepared by oxidation at 175 °C for 60 min. The oscillatory TRFR on the Fe(4 nm)/GaAs hybrid structures show positive spin polarization, consistent with previous

study [37]. On the other hand, the spin polarization for Fe_3O_4/GaAs is negative (S_{FPP} = -73 μrad) and has a larger magnitude than for the Fe/GaAs sample (S_{FPP} = 28 μrad). The

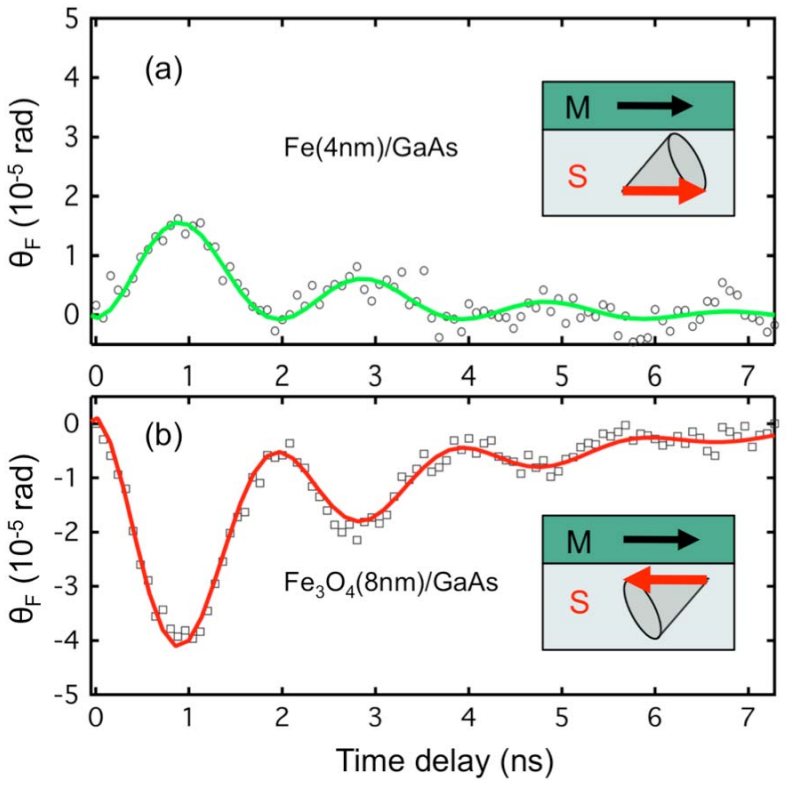

FIG 4.6 Time delay scans for (a) Fe(4 nm)/GaAs and (b) Fe_3O_4(8 nm)/GaAs.

opposite spin polarization in Fe_3O_4/GaAs compared to Fe/GaAs is expected because the density of states (DOS) at the Fermi level in bcc Fe has a positive spin polarization (majority spin) while the Fermi level DOS of Fe_3O_4 is theoretically predicted to have 100% negative spin polarization. This result demonstrates the generation of spin polarization by spin reflection in Fe_3O_4/GaAs and the sign and magnitude are consistent with theoretical expectations.

We now take advantage of the FPP measurement to investigate the influence of

growth conditions on spin-dependent properties of Fe_3O_4/GaAs interfaces. Measuring the spin dynamics of the reflected electrons (time after 50 ps) by time-resolved Faraday rotation (TRFR) reveals the initial electron spin S_{FPP}, which is the quantity of the most interest. Specifically, we study the effect of oxidation temperature, because it is a key factor in the reaction of Fe and oxygen for forming Fe_3O_4. The post-growth oxidation is expected to penetrate into the Fe film with a characteristic depth that should depend on the oxidation temperature and time. Roughly, for fixed oxidation time (e.g. 30 min), the oxidation depth increases exponentially with growth temperature (in the range of 50 °C to 275 °C), as verified by a series of wedge samples. The oxidation rate is the highest in the first few minutes, and drops dramatically with increasing time [38].

FIG 4.7 shows S_{FPP} as a function of thickness for a series of wedge samples oxidized for 60 min at different temperatures. For oxidation temperatures at 150 °C, 175 °C and 225 °C, FPP effect is observed, with varies in the thickness dependence. In terms of S_{FPP} amplitude, the sample oxidized at 175 °C shows the maximum signal. Both 150 °C and 225 °C samples show a moderate S_{FPP}, and the former is due to under oxidation (the RHEED pattern shows some characteristics of Fe_3O_4 film, but more blurry than that for the film oxidized at 175 °C) while the latter is due to degradation of the interface. For oxidation at 275 °C, no spin polarization is observed for any thickness. These features are likely due to two effects that diminish the spin polarization. First is the over-oxidation of the Fe/GaAs interface, which leads to a suppression of spin polarization. This effect is most important at low thickness and produces an increasingly large zero spin-polarization regime with increasing oxidation temperature. Second is the interdiffusion at the Fe/GaAs

interface, which reduces the spin polarization across the entire wedge.

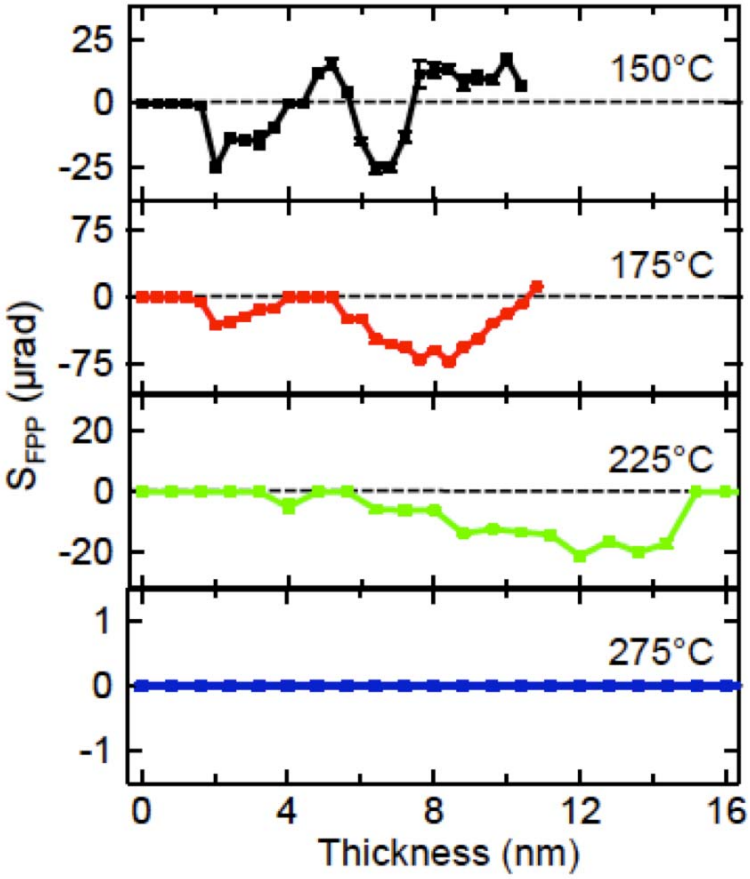

Figure 4.7 S_{FPP} as a function of thickness for wedge samples oxidized at 150 °C, 175 °C, 225 °C and 275 °C, respectively. Error bars for all the data points are displayed, or smaller than the size of the data points.

The importance of the FPP measurement as a probe of the spin dependent properties of Fe_3O_4/GaAs hybrid structures is further highlighted by considering RHEED patterns for samples oxidized 175 ºC, 225 ºC and 275 ºC (FIGs 4.3). The RHEED patterns, at these three temperatures, all indicate the formation of Fe_3O_4 films with slightly sharper patterns at higher temperatures. Comparing the RHEED patterns with the

FPP data shows that RHEED is not an adequate characterization tool for optimizing the spin-dependent properties of Fe_3O_4/GaAs interfaces. While the RHEED patterns suggest similar quality across the 175 °C – 275 °C temperature window, the FPP measurement clearly shows that that 175 °C oxidation temperature is much better than 275 °C. The main difference is that RHEED probes the vacuum/Fe_3O_4 interface, whereas the FPP measurement probes the buried Fe_3O_4/GaAs interface, which is the most important for spintronic devices. Our results verify that interface quality is crucial for spin generation in FM/semiconductor hybrid structures and establish FPP as an effective characterization tool to optimize FM/GaAs hybrid structures.

4.6 Oscillatory FPP with Fe_3O_4 thickness

We now focus on the oscillatory features of the FPP thickness dependence curves. In FIG 4.7, the RHEED patterns of all samples are characteristic of Fe_3O_4 (shown in FIG 4.3). Interestingly, the curves for 150 °C and 175 °C exhibit oscillations in the FPP amplitude as a function of film thickness. For the 150 °C sample, S_{FPP} oscillates between negative and positive values through nearly two oscillations with a period of ~4.2 nm. For the 175 °C sample, the FPP amplitude oscillates mainly between a negative value and zero with a period of ~5.0 nm. These oscillations have been observed consistently on several samples prepared in this temperature regime. For oxidation at 225 °C, the spin polarization is negative and the oscillations are no longer present. At the higher oxidation temperature of 275 °C, no FPP signal is observed.

To verify that the oscillations are real effect, we measure one of the wedge samples by nuclear field at 5 K. FIG 4.8 shows the nuclear field B_n as a function of Fe_3O_4 thickness on the sample prepared at 175 °C, which exhibit the same oscillatory features in

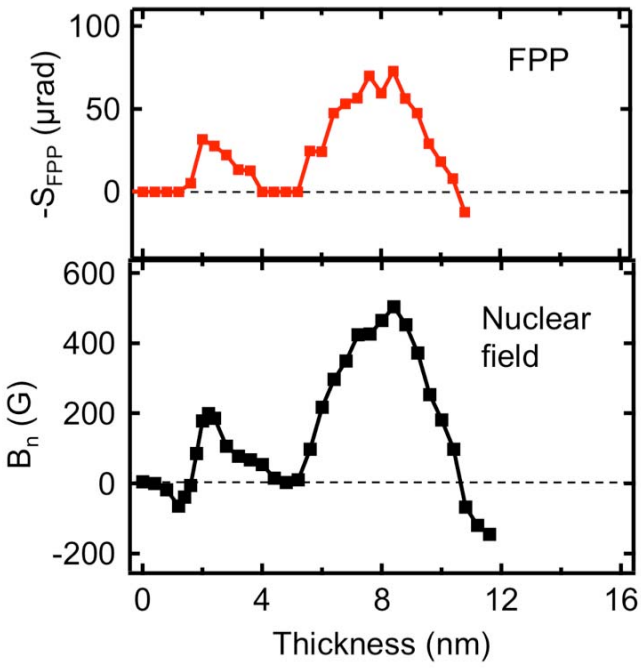

FIG 4.8 Nuclear field measurement on the Fe_3O_4 wedge grown at 175°C. The FPP data is shown for comparison.

the FPP thickness dependence. We also checked the thickness dependence along $[1\bar{1}0]$ direction of GaAs, and it shows the same oscillations, so the possibility of magnetic anisotropy is excluded.

4.6.1 Spin polarized quantum well

Electron waves confined in an ultrathin film experience multiple reflections at the film boundaries and give rise to quantum well (QW) states [39]. QW states in

semiconductors are utilized for two-dimensional transport and quantized optical transitions for lasers [40]. In metallic magnetic multilayers, the formation of spin-polarized QW states in the non-magnetic (NM) layers produces oscillatory interlayer magnetic coupling [8, 9], oscillatory magneto-optic effect [41] and spin-polarized resonant tunneling [42]. Magnetic QWs in principle provide more freedom since the two spin species could have different wavelengths to produce spin-split QW states. Experimentally, QW states have been observed in ferromagnetic metal thin films (Fe and Co) [43, 44] and result in the modulation of spin-dependent properties (e.g. magneto-optic Kerr effect [11, 12], magnetic anisotropy [10], tunneling magnetoresistance [45]).

4.6.2 Explanation of the oscillatory FPP

The oscillations in the FPP as a function of Fe_3O_4 thickness could be explained by the formation of spin-polarized QW states in the Fe_3O_4 film, which causes the Fermi level spin polarization to oscillate between positive and negative values. In principle, there are two distinct wavelengths for spin up and spin down electrons in magnetic films and QW states form according to the quantization condition

$$2k_{\uparrow,\downarrow}d + \phi_{\uparrow,\downarrow} = 2\pi n \qquad (4.1)$$

where n is an integer, d is the film thickness, and $k_{\uparrow}$ ($k_{\downarrow}$) and $\phi_{\uparrow}$ ($\phi_{\downarrow}$) are the wavevector and the phase accumulated for spin up (down) electrons upon reflection at the boundaries, respectively. This produces oscillations in the Fermi level (ε_F) DOS as a function of thickness with periods of $\pi / k_{\uparrow}(\varepsilon_F)$ and $\pi / k_{\downarrow}(\varepsilon_F)$. Theoretically, Fe_3O_4 is predicted to be a half-metal with only spin down electrons, but spin-polarized photoemission

experiments find spin polarization below 80% [3, 4]. Therefore, we consider both spin polarizations at the Fermi level. For the 150 °C sample, the sign of the FPP signal oscillates between positive and negative values, indicating that both spin states are present at the Fermi level. The oscillation could be due to quantum confinement of one spin species or both spin species. For the 175 °C sample, the FPP signal oscillates between zero and negative values, so it is possible that there are only spin down states confined at ε_F. The oscillation period of 4-5 nm is longer than typical periods observed in metallic QWs (less than 1 nm), which could result from smaller Fermi wavevectors associated with the lower electron density of Fe_3O_4 (~10^{21} cm^{-3} [46, 47]) compared to metals (~10^{23} cm^{-3}). Furthermore, earlier work on QW states in Fe_3O_4 [13], suggests a de Broglie wavelength ($2p/k_F$) of ~10 nm (i.e. QW oscillation period of ~5 nm), which is consistent with our data. A quantitative investigation of the oscillatory period would require a direct comparison of the Fermi surface and QW states via angle-resolved photoemission spectroscopy (ARPES) [39]. At higher temperatures, the interface is expected to degrade through interdiffusion or over-oxidation and therefore the QW states would be destroyed. Apart from the spin polarization of the Fermi level DOS of the Fe_3O_4 film, there are other factors that could affect the sign of the FPP signal such as the Schottky barrier height and carrier concentration of the GaAs [48, 49]. However, these effects are ruled out as the origin of the FPP oscillations as discussed below.

4.7 Oscillatory MOKE

To further explore the origin of the oscillations, we measure the magnetic properties of the Fe_3O_4/GaAs hybrid structure along the wedge by MOKE (835 nm at RT and 80K), which depends only on the properties of the Fe_3O_4 layer. FIG 4.9 (a)-(c) shows

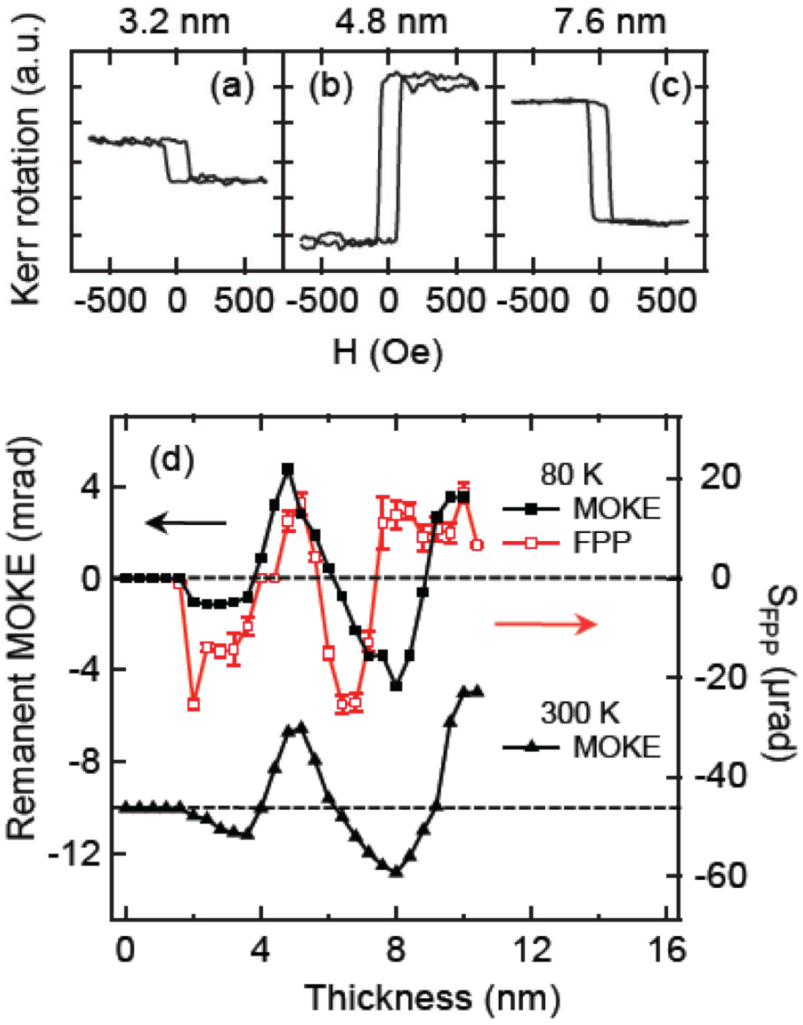

Figure 4.9 (a) – (c) MOKE hysteresis loops on Fe3O4 thicknesses at 3.2 nm, 4.8 nm and 7.6 nm, respectively. (d) Remanent MOKE (Kerr rotation) along the wedge sample oxidized at 150 °C, measured at 80 K (black squares) and 300 K (black triangles, offset by -10 mrad), and SFPP (red/grey square) is plotted for comparison. The errors of the data points are within the size of the data points.

the MOKE hysteresis loops taken on the 150 °C sample at different film thicknesses at 80 K. Interestingly, the sign of the MOKE also depends on the film thickness. A more detailed scan of the remanent MOKE signal as a function of thickness (FIG 4.9d) displays oscillations at 80 K and 300 K with similar shape as the FPP thickness dependence. This implies that the oscillations in both FPP and MOKE are related to the properties of Fe_3O_4 layer, as opposed to Schottky barrier or parameters of GaAs.

While the quantitative calculation of the MOKE coefficient in magnetic metals is rather complicated [50-52], it is known that the photoexcitation process is determined by Fermi's golden rule, with $h\nu = \varepsilon_f(k) - \varepsilon_i(k)$, where $\varepsilon_i(k)$ and $\varepsilon_f(k)$ are initial and final states of photoexcitation, respectively. Modulating the density of the initial or final states by quantum confinement should induce oscillations in the MOKE. Theoretically, the Kerr rotation in Fe_3O_4 for 1.49 eV photon energy (835 nm) involves the minority t_{2g} states [51, 52]. Because the t_{2g} states are also responsible for the spin polarization at the Fermi level [1, 2], quantum confinement of the t_{2g} bands can account for the oscillations in both the MOKE and FPP signals. Moreover, this explains why two experiments that rely on different physical processes (optical transitions for MOKE, electron reflection for FPP) exhibit similar oscillatory behavior. The differences in the oscillation periods of MOKE and FPP are likely due to the fact that the MOKE not only depends on the states at the Fermi level but also states away from the Fermi level, which can produce different periods because of the energy dispersion of the wavevector [39].

4.8 Discussion

We also consider the possibility of different mechanisms for the observed MOKE oscillations. It is known that the Kerr rotation changes sign as a function of the photon energy in the range of 1-2 eV [50-52], so a change in the film quality or stoichiometry along the wedge could shift the Kerr rotation vs. photon energy curve to induce a sign change. However, it would be expected that the materials quality would change monotonically and only one zero crossing should appear. The fact that the MOKE signal crosses zero three times makes this possibility highly unlikely.

4.8.1 Interference effect in multilayer thin films

The sample for transmission and reflection measurement is consisted of Fe_3O_4/GaAs(123 nm)/AlGaAs(400 nm). Considering the fact that both FPP and MOKE measurements are optics measurement of magneto-optical effect, one concern is whether the interference could produce the observed oscillations. An intuitive answer is no, because for film interference to happen the thickness of the film times index of refraction has to be comparable with the wavelength, which is 812 nm or 835 nm. However, in the whole structure, only the thickness of Fe_3O_4 changes, and the product of the film thickness (< 10 nm) and the refraction index (2.5) is much less than 812 nm. We also perform the MOKE calculation for multilayers following the method of Zak et al and we find that the sign change in MOKE is not from an interference effect (FIG E.3a). A sign change from an interference effect would occur at Fe_3O_4 thickness of ~100 nm (FIG E.3b), which is much thicker than our film thickness. Even if the thickness of AlGaAs is not uniform along the wedge (i.e. from spray etching), the interference in the AlGaAs

film layer does not produce sign change, only some resonant peaks when the interference is constructive (FIG E.4). In Appendix E, we explain the analysis using Zak's method [53].

References:

[1] A. Yanase, and N. Hamada, J. Phys. Soc. Jpn. **68**, 1607 (1999).

[2] Z. Zhang, and S. Satpathy, Phys. Rev. B **44**, 13319 (1991).

[3] Y. S. Dedkov, U. Rudiger, and G. Guntherodt, Phys. Rev. B **65**, 064417 (2002).

[4] M. Fonin *et al.*, Phys. Rev. B **72**, 104436 (2005).

[5] G. Hu, and Y. Suzuki, Phys. Rev. Lett. **89**, 276601 (2002).

[6] Y. X. Lu *et al.*, Phys. Rev. B **70**, 233304 (2004).

[7] E. Wada *et al.*, App. Phys. Lett. **96**, 102410 (2010).

[8] S. S. P. Parkin, R. Bhadra, and K. P. Roche, Phys. Rev. Lett. **66**, 2152 (1991).

[9] R. K. Kawakami *et al.*, Phys. Rev. Lett. **82**, 4098 (1999).

[10] J. Li *et al.*, Phys. Rev. Lett. **102**, 207206 (2009).

[11] F. J. Himpsel, Phys. Rev. B **44**, 5966 (1991).

[12] W. Geerts *et al.*, Phys. Rev. B **50**, 12581 (1994).

[13] E. V. Babkin, N. G. Cherkunova, and S. G. Ovchinnikov, Solid State Commun. **52**, 735 (1984).

[14] S. Taketomi *et al.*, J. Phys. Soc. Jpn. **60**, 3426 (1991).

[15] E. J. Verwey, Nature **144**, 327 (1939).

[16] E. J. Verwey, P. W. Haayman, and F. C. Romeijn, J. Chem. Phys. **15**, 181 (1947).

[17] M. Fonin *et al.*, J. Phys.: Condens. Matter **19**, 315217 (2007).

[18] E. J. Samuelsen *et al.*, Journal of Applied Physics **39**, 1114 (1968).

[19] M. G. Chapline, and S. X. Wang, J. App. Phys. **97**, 123901 (2005).

[20] M. Fonin *et al.*, J. Phys.: Condens. Matter **20**, 142201 (2008).

[21] E. J. W. Verwey, and P. W. Haayman, Physica **8**, 979 (1941).

[22] J. Yoshida, and S. Iida, J. Phys. Soc. Jpn. **47**, 1627 (1979).

[23] J. R. Cullen, and E. Callen, Physical Review Letters **26**, 236 (1971).

[24] D. Ihle, and B. Lorenz, J. Phys. C **19**, 5239 (1986).

[25] J. M. Zuo, J. C. H. Spence, and W. Petuskey, Physical Review B **42**, 8451 (1990).

[26] J. P. Wright, J. P. Attfield, and P. G. Radaelli, Physical Review Letters **87**, 266401 (2001).

[27] H. Seo, M. Ogata, and H. Fukuyama, Physical Review B **65**, 085107 (2002).

[28] W. Eerenstein, T. T. M. Palstra, and T. Hibma, Phys. Rev. B **66**, 201101(R) (2002).

[29] S. Parkin *et al.*, Proceedings of the IEEE **91**, 661 (2003).

[30] H. J. Kim, J. H. Park, and E. Vescovo, Physical Review B **61**, 15284 (2000).

[31] M. Paul *et al.*, Phys. Rev. B **79**, 233101 (2009).

[32] M. Ferhat, and K. Yoh, App. Phys. Lett. **90**, 112501 (2007).

[33] T. Taniyama *et al.*, Journal of Applied Physics **103**, 07D705 (2008).

[34] S. K. Arora *et al.*, Phys. Rev. B **77**, 134443 (2008).

[35] D. T. Margulies *et al.*, Physical Review Letters **79**, 5162 (1997).

[36] W. Eerenstein *et al.*, Physical Review Letters **88**, 247204 (2002).

[37] R. J. Epstein *et al.*, Phys. Rev. B **65**, 121202 (2002).

[38] P. C. J. Graat *et al.*, Journal of Applied Physics **82**, 1416 (1997).

[39] T.-C. Chiang, Surface Science Reports **39**, 181 (2000).

[40] J. H. Davies, *The Physics of Low-Dimensional Semiconductors: An Introduction* (Cambridge University Press, Cambridge, UK, 1998).

[41] Y. Suzuki *et al.*, Phys. Rev. Lett. **80**, 5200 (1998).

[42] S. Yuasa, T. Nagahama, and Y. Suzuki, Science **297**, 234 (2002).

[43] R. Zdyb, and E. Bauer, Phys. Rev. Lett. **88**, 166403 (2002).

[44] D. H. Yu *et al.*, Phys. Rev. B **68**, 155415 (2003).

[45] T. Nozaki, N. Tezuka, and K. Inomata, Phys. Rev. Lett. **96**, 027208 (2006).

[46] W. J. Siemons, IBM J. Res. Develop. **14**, 245 (1970).

[47] D. Reisinger *et al.*, App. Phys. Lett. **85**, 4980 (2004).

[48] C. Ciuti, J. P. McGuire, and L. J. Sham, Phys. Rev. Lett. **89**, 156601 (2002).

[49] G. E. Bauer *et al.*, Phys. Rev. Lett. **92**, 126601 (2004).

[50] X. Zhang, J. Schoenes, and P. Wachter, Solid State Commun. **39**, 189 (1981).

[51] W. F. J. Fontijn *et al.*, Phys Rev. B **56**, 5432 (1997).

[52] I. Leonov *et al.*, Phys Rev. B **74**, 165117 (2006).

[53] J. Zak *et al.*, J. Magn. Magn. Mater. **89**, 107 (1990).

Chapter 5

Conclusions

In this dissertation, I have presented the study of spin dependent reflection at ferromagnet/GaAs interfaces. The spontaneous spin polarization of optically injected electrons upon reflection is called the ferromagnetic proximity (FPP) effect. FPP is proven to a powerful too for characterizing the FM/GaAs interfaces, because it directly probe the properties of interest, and it provides information about engineering the interfaces for best performance in electronic applications. In general, the sign of FPP depends on the following factors: (1) Barrier height and thickness. (2) Interfacial (local) density of states of the FM. (3) Tunnel barrier material. (4) Interfacial bonding depending on details of the structure. (disorder). These are what we learned from the FPP measurement, which could be applied electrical transport through FM/semiconductor interfaces.

The two systems we studied are Fe/MgO/GaAs [1] and Fe_3O_4/GaAs heterostructures. We observed inversion of FPP by MgO or Mg interlayers in Fe/MgO(Mg)/GaAs system, and the origin of the sign reversal is the interfacial bonding with Mg, inducing changes in Schottky barrier height or density of states at the Fermi level. In this system, we also demonstrated the tuning of spin dependent reflection by interface modification, i.e. interlayer material. For Fe_3O_4 on GaAs, we observed

oscillatory spin polarization and magneto-optic Kerr effect as a function of Fe_3O_4 thickness, which we attributed to the formation of spin polarized quantum wells. The quality of the interface, related to spin selective reflection, is highly sensitive the growth conditions. This experiment demonstrates the tuning of spin dependent reflection and also the spin polarization of the magnetite film by quantum well modulations. Both studies provide new perspectives on tuning of spin dependent properties of the FM/semiconductor heterostructure, which are important to spin injection, manipulation and detection in electrical devices.

References:

[1] Y. Li *et al.*, Phys. Rev. Lett. **100**, 237205 (2008).

Appendices

A. Setup of the TRFR measurement

Equipment and optics components used are: flow cryostat (Janis), 2 lock-in amplifiers (Signal recovery 7265, or Stanford SR830), voltage amplifier (Stanford SR560) connection, photodiode bridge (Appendix B), beam splitter, retroreflection mirror and delay line, 2 mechanical choppers, polarcor linear polarizer, photoelastic modulator (PEM)/variable waveplate, Glan-Thompson linear polarizer, half waveplate, quarter waveplate, polarizing beam splitter, lenses, mirrors, high power pinhole (75 μm diameter). For assistance in setup, the following tools are needed: infrared (IR) viewer, (and/or IR viewing card, IR sensitive CCD camera with television), a viewing plate with grids for alignment. The setup procedure follows FIG 2.1. Try to make the beam always aligned with the holes on the optics table, then the 45° incidence on mirrors and delay line alignment will be easier. The output of the photodiode bridge is amplified again by SR560. The output from SR560 goes to the input of the first lock-in, which receives reference signal from the PEM or the chopper in the pump line at frequency f_1. The output of the first lock-in goes to the input of the second lock-in, which receives reference signal from the chopper in the probe line at frequency f_2. The time constant on the first lock-in should be $1/f_1 < TC_1 < 1/f_2$. The time constant on the second lock-in

should be longer than $1/f_2$. Longer time constant gives more average over time and cleaner signal. Here I list some useful details or tips in actual setting up.

PEM or variable waveplate. The fast axis of PEM or variable waveplate is 45° rotated from the horizontal direction. PEM changes its retard at specific frequency, 41 kHz for the PEM we got. The retard of the variable waveplat is also tunable with the applied voltage, and the retard is set when you set the voltage. We basically use PEM as a fast chopper for the pump beam. The fast The PEM changes it retard from $+\lambda/4$ to $-\lambda/4$ at 41 kHz, so the pump beam changes between right circularly polarized light and left circularly polarized light at this frequency. For nuclear field measurement, we usually use PEM and mechanical chopper could be removed from the pump beam. Alternatively, we can use $\lambda/4$ waveplate instead of PEM and a mechanical chopper. For the ferromagnetic proximity polarization (FPP) measurement, the pump beam is linearly polarized, and the Faraday rotation signal is zero at zero time delay. In order to check for the overlapping of pump and probe beams, the regular TRFR measurement should be done with circularly polarized pump before the FPP measurement. So for the FPP measurement, we use variable waveplate so that the pump beam does not move when changing its polarization from circular to linear. We first set the variable waveplate as a $\lambda/4$ (circular polarized pump), and get the pump and probe beam overlapped and signal optimized. Then we change the retard to $\lambda/2$ or full waveplate (linearly polarized pump) for the FPP measurement.

Delay line alignment. The criterion for delay line aliment is: the pump beam does not move when the delay line mirror (the retroreflection mirror) moves back and forth. A

good tool for better viewing the laser spot is CCD camera with television for display; IR viewer would be fine too. The easy procedure should be: (1) Adjust the mirror M1 to guide the beam to the retroreflection mirror and roughly straight. Both the position and the orientation of mirror should be adjusted. (2) Place the viewing plate in the beam after it gets reflected from the delay line mirror. (3) Move the delay line mirror back and forth and adjust the knobs of M1 to satisfy the above mentioned criterion. Adjust the mirror when the delay line is moving back (towards negative time delay). Turn the knobs in the direction, which makes the laser spot not moving on the viewing plate while the delay line is moving back. Repeat this for several times and do horizontal and vertical direction one by one, until you get to the criterion.

Pump beam or probe beam directly incident on the sample (FIG A.1). After the pump or probe beam is already setup as a linearly polarized beam, reflection from mirrors could introduce imperfections, i.e. circular component. With the setup of FIG A.1 (a), the linear polarization of the probe beam is best conserved, and it benefits the Faraday rotation detection. However, in the FPP measurement, we need to make sure that the pump beam is completely linear polarized, so we use the setup shown in FIG A.1 (b).

Getting signal. Before cooling down using liquid helium, the pump and probe beams should be pre-overlapped. Two ways of overlapping are usually used. (1) Reflect the two beams far away and check the distance between the two beams at various places (near and far), until the distance does not change. (2) Pinhole check. Let the pump and probe beam pass through the focusing lens and out the pinhole at the focusing point (mounted on a xyz-stage). Both beams should pass through the pinhole, and the two beam

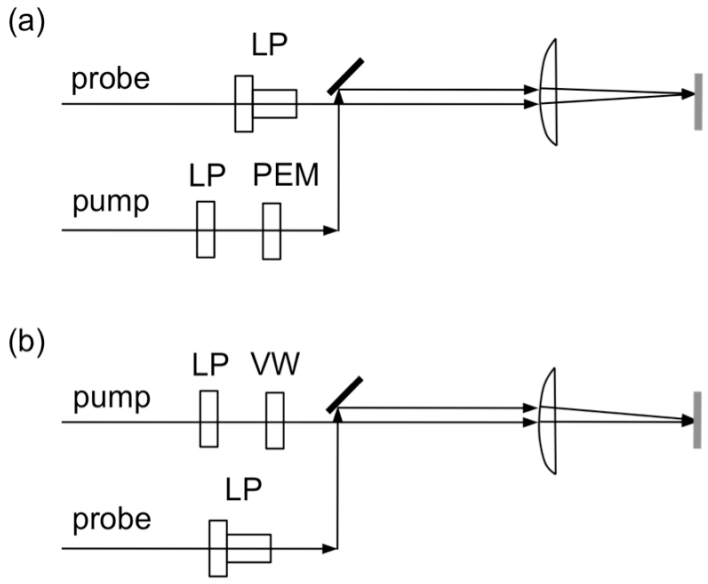

FIG A.1 Two schemes of setting up the pump and probe beams. (a) The probe beam directly goes to the focusing lens after it passes through the linear polarizer, thus reserve its linear polarity. (b) The polarization of the pump beam gets better reserved without reflection by mirrors before focusing onto the sample.

spot should appear and disappear at the same time when you move the pinhole up-and-down or lefe-and-right. If the first method is used and a long reflection distance is used, the pinhole check could be skipped. After cooling down the sample to low temperature, adjust mirror M4 with care for further overlapping. The important factors for getting the signal are, wavelength of the laser (812 nm or 818 nm), overlapping of the pump and probe, z-position of the sample. Make sure that the delay line is at a positive time delay. Remove the stopper for the transmitted pump beam after so that it also gets detected by the photodiodes, and then auto phase the first lock-in. Try to block the transmitted pump using a plate piece with a sharp edge, but do not get into the probe beam. A clear signal

should show up on the second lock-in. Auto phase the second lock-in. Optimize the signal by adjusting the wavelength, mirror M4, the z-position of the sample.

Double delay line. In some cases, longer time delay range is very useful for determining the spin dynamics, especially when the precession frequency is very low due to the presence of negative nuclear field. We modify the setup of mechanical delay line so that the pump beam goes through the delay twice. The setup employs a polarizing beam splitter (pass p-polarization and reflect s-polarization) and a quarter waveplate, as shown in FIG A.2. In this setup, the initial beam is p-polarized, and changes to s-polarized after it goes through the delay line. When the beam first gets to the beam

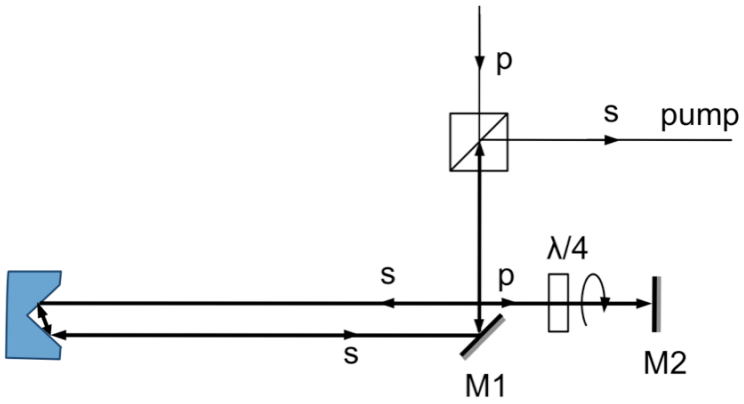

FIG A.2 Double delay line setup. “s” or “p” next to each arrow indicates the polarization of light propagating in that direction. The path where the light goes through twice has double weight in size.

splitter, it passes through because it is p-polarized. Then it goes through the delay line once and turns into right circularly polarized light after passing through the quarter waveplate. The right circularly polarized light changes to left circularly polarized light by reflection of the end mirror. The left circularly polarized light go through the 3λ/4

waveplate (passing the opposite direction) and turns to linearly polarized light in perpendicular direction as s-polarized. The s-polarized light beam goes though the delay line once more, and gets reflected at the polarizing beam splitter. The alignment for overlapping in the double delay line is same as the single delay line. First, adjust mirror 1 as the regular single delay line by checking the beam spot in front of the end mirror. After that, M1 is not touched any more. Second, adjust the end mirror M2 and check the beam spot after the polarizing beam splitter. The method is the same as adjusting M1.

A.1 Analysis of Faraday rotation and photodiode bridge circuit

The Faraday rotation (θ_F) is a small quantity, 10^{-6} to 10^{-4} rad in our measurement, thus require careful technique for recovering the signal. The incident probe beam is p-polarized, and after pass through the sample with spin polarization along the beam path, it has a small s component, which is the quantity related to θ_F. A most direct way of measuring the rotation is to pass the beam through a polarizing beam splitter, and analyze the s component and p component. We can imagine that any noise from other sources of light contributes to the small s component. A very clever method is the following: rotates the plane of polarization by 45° using a half waveplate (FIG A.3), and then measures the

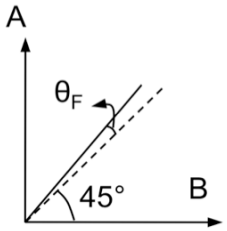

FIG A.3 Analysis of Faraday rotation.

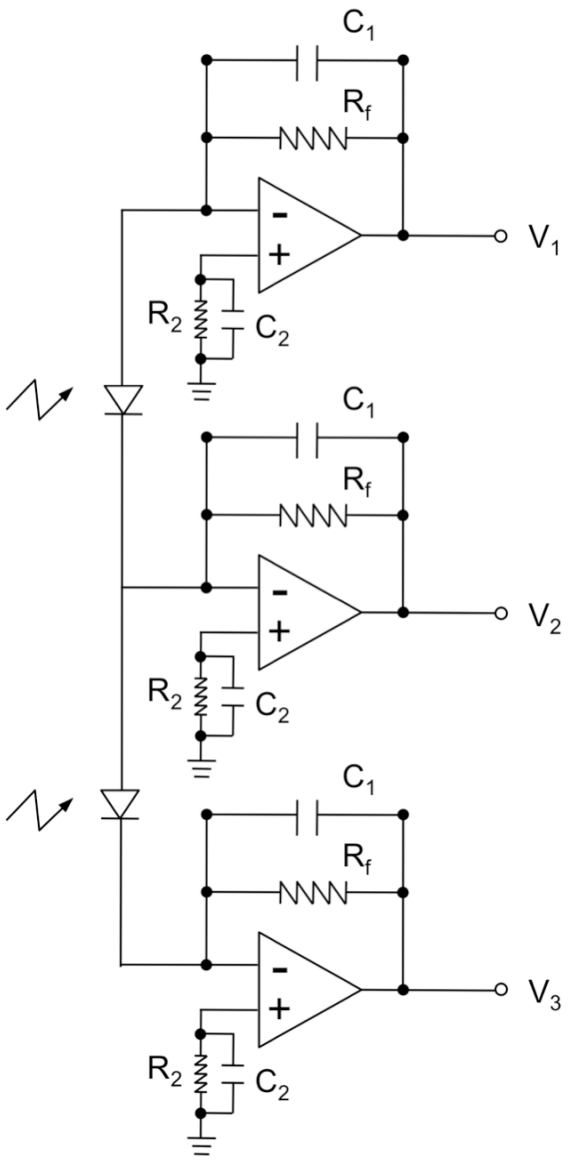

FIG A.4 Photodiode bridge circuit. $R_f = R_2 = 100$ kΩ, $C_1 = 10$ pF, $C_2 = 0.1$ μF.

difference of *s* and *p* components by photodiode bridge with Opamp circuit (FIG A.4). In this way, any noise related to changes in the environment is canceled off by subtracting "A" and "B" components. The θ_F is proportional to the intensity difference of A and B, as

shown below. In FIG A.3, the θ_F is shown to be the plane of polarization away from the 45° direction and the intensity of A and B are expressed as:

$$I_A = \left[E\sin(45^\circ + \theta_F)\right]^2,\ I_B = \left[E\cos(45^\circ + \theta_F)\right]^2$$

$$\begin{aligned} I_A - I_B &= \left[E\sin(45^\circ + \theta_F)\right]^2 - \left[E\cos(45^\circ + \theta_F)\right]^2 \\ &= E^2\left[(\sin 45^\circ\cos\theta_F + \cos 45^\circ\sin\theta_F)^2 - (\cos 45^\circ\cos\theta_F - \sin 45^\circ\sin\theta_F)^2\right] \\ &= \frac{1}{2}E^2\left[(\cos\theta_F + \sin\theta_F)^2 - (\cos\theta_F - \sin\theta_F)^2\right] \\ &= 2E^2\sin\theta_F\cos\theta_F \\ &\doteq 2E^2\theta_F \qquad (\theta_F \ll 1,\ \cos\theta_F \doteq 1,\ \sin\theta_F \doteq \theta_F) \end{aligned}$$

$$\theta_F = \frac{I_A - I_B}{2(I_A + I_B)}.$$

The photodiode bridge measures the difference of intensities of A and B components. The circuit is shown in FIG A.4. The photodiodes used are Silicon PIN photodiodes from Hamamatsu and the Opamps are OPA627. The output voltages are $V_1 = I_A R_f$, $V_3 = -I_B R_f$, and $V_2 = (I_A - I_B)R_f$.

B. Calculation of excitation density N_{ex}

The typical pump intensity we use is 1 mW, which is the average power measured by a Coherent™ laser power meter. The laser spot size on the sample is about 40 μm in diameter. The absorption coefficient α I use is 10^4/cm, for 5 K and energy of 1.52 eV.

Total energy in one pump pulse = power (1 mW) / repetition rate (76 MHz)

$= 1.3\times10^{-11}$ J

# of photons in one pump pulse = total energy / 1.5 eV (1.6×10^{-19} J) = 8.1×10^7

# of photons absorbed = # of photons incident * α * thickness

$= 8.1\times10^{7} \times 10^{4}/\text{cm} \times 123\ \text{nm}$

$= 1.0\times10^{7}$

$\boldsymbol{N_{ex}}$ = # of photons absorbed / volume

$= 1.0\times10^{7} / [(40\ \mu\text{m})^2 \times 123\ \text{nm}]$

$= 5.1\times10^{16}/\text{cm}^3$

C. Spin dependent reflection coefficients in FPP

This is a one dimensional square tunnel barrier problem. The potential function is shown in FIG C.1, where the barrier thickness is a, and the barrier height is U_b. The

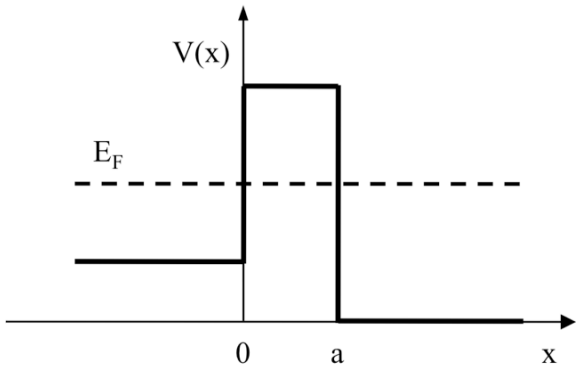

FIG C.1 One dimensional tunnel barrier, a simple model for spin dependent reflection.

wave function is constructed as the following, as the solution for Schrödinger equation:

$$\psi(x) = \begin{cases} e^{ik_x x} + r_{\pm}\, e^{-ik_x x} & (x < 0) \\ Ae^{k_b x} + Be^{-k_b x} & (0 < x < a) \\ Se^{ik_{\text{fm}} x} & (x > a) \end{cases} \qquad \text{(C.1)}$$

We can solve for the coefficients by matching the boundary conditions, which are continuity of $\psi(x)$ and $\psi'(x)$. The $R_{\pm}$ are the spin dependent reflection coefficients which are of primary interest. At $x = 0$, the continuity of $\psi(x)$ and $\psi'(x)$ gives:

$$\begin{cases} 1 + R_{\pm} = A + B \\ i\dfrac{k_x}{k_b}(1 - R_{\pm}) = A - B \end{cases} \qquad \text{(C.2)-(C.3)}$$

Solve the above two equations and we get

$$\begin{cases} A = \dfrac{1}{2}\left[\left(1 + i\dfrac{k_x}{k_b}\right) + R_{\pm}\left(1 - i\dfrac{k_x}{k_b}\right)\right] \\ B = \dfrac{1}{2}\left[\left(1 - i\dfrac{k_x}{k_b}\right) + R_{\pm}\left(1 + i\dfrac{k_x}{k_b}\right)\right] \end{cases} \qquad \text{(C.4)-(C.5)}$$

Similarly at $x = a$, the continuity condition gives

$$\begin{cases} Ae^{k_b a} + Be^{-k_b a} = Se^{ik_{\pm}^{\mathrm{fm}} x} \\ Ae^{k_b a} - Be^{-k_b a} = i\dfrac{k_{\pm}^{\mathrm{fm}}}{k_b} Se^{ik_{\pm}^{\mathrm{fm}} x} \end{cases} \rightarrow \begin{cases} A = \dfrac{S}{2}\left(1 + i\dfrac{k_{\pm}^{\mathrm{fm}}}{k_b}\right) e^{ik_{\pm}^{\mathrm{fm}} a - k_b a} \\ B = \dfrac{S}{2}\left(1 - i\dfrac{k_{\pm}^{\mathrm{fm}}}{k_b}\right) e^{ik_{\pm}^{\mathrm{fm}} a + k_b a} \end{cases} \qquad \text{(C.6)-(C.7)}$$

Comparing Eq. C.4 with Eq. C.6, and Eq. C.5 with Eq. C.7, we can get the flowing two equations:

$$\begin{cases} \left(1 + i\dfrac{k_x}{k_b}\right) + R_{\pm}\left(1 - i\dfrac{k_x}{k_b}\right) = S\left(1 + i\dfrac{k_{\pm}}{k_b}\right) e^{ik_{\pm}^{\mathrm{fm}} a - k_b a} \\ \left(1 - i\dfrac{k_x}{k_b}\right) + R_{\pm}\left(1 + i\dfrac{k_x}{k_b}\right) = S\left(1 - i\dfrac{k_{\pm}}{k_b}\right) e^{ik_{\pm}^{\mathrm{fm}} a + k_b a} \end{cases} \qquad \text{(C.8)-(C.9)}$$

Canceling off *S*, we get the value for $R_{\pm}$:

$$R_{\pm} = \frac{(1 - ik_x / k_b)(1 + ik_{\pm}^{\mathrm{fm}} / k_b)e^{-k_b a} - (1 + ik_x / k_b)(1 - ik_{\pm}^{\mathrm{fm}} / k_b)e^{k_b a}}{(1 - ik_x / k_b)(1 - ik_{\pm}^{\mathrm{fm}} / k_b)e^{k_b a} - (1 + ik_x / k_b)(1 + ik_{\pm}^{\mathrm{fm}} / k_b)e^{-k_b a}}$$
$$= \frac{(ik_{\pm}^{\mathrm{fm}} - k_b)(ik_x + k_b)e^{2k_b a} - (ik_{\pm}^{\mathrm{fm}} + k_b)(ik_x - k_b)}{(ik_{\pm}^{\mathrm{fm}} - k_b)(ik_x - k_b)e^{2k_b a} - (ik_{\pm}^{\mathrm{fm}} + k_b)(ik_x + k_b)} \qquad \text{(C.10)}$$

D. Sample preparation

The procedure is described in Chapter 2. Here we give more details of the flowing steps:

Polishing: (1) The sample (GaAs sample glued on a piece of sapphire) is mounted on the metal plate of the polishing tool (shown in FIG D.1) using wax. Place a small

FIG D.1 Sample polishing with the pad.

amount of the solid wax on the metal plate and heat up the metal plate to 130 °C, and the wax melts. Then place the sample (sapphire side) on the wax and press it evenly with tweezers. Transfer the hot metal plate to a cool place and let it cool down. After it cools

down to room temperature, the sample is mounted on the metal plate. (2) Polishing. Wet the glass pad with water, and then place the lapping film of 5 μm roughness on the polishing pad without trapping air bubbles underneath. Install the metal plate onto the polishing tool, spray water on the lapping film and start polishing. Thickness of the film should be checked frequently to avoid breaking the GaAs sample. Stop until get down to 100 μm. (3) Take off the metal plate and heat it up to 130 °C, and then remove the sample after the wax melts. (4) Clean the sample with acetone.

Spray etching: (1) Mount the polished sample with patterned widow onto the sample holder (FIG D.2). (2) Prepare the solution and mix it in a 500 ml beaker. The

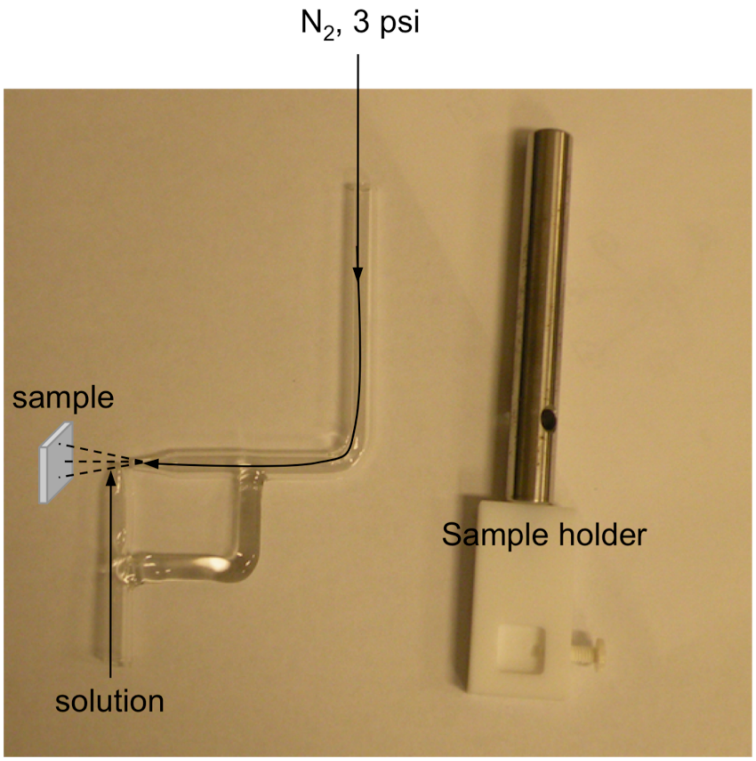

FIG D.2 Spray etching tools. The bottom end of the glass tube is immersed into the etching solution, and the sample is held in a holder made of Teflon.

solution should be prepared each time and right before the etching. (3) Prepare an empty beaker and get the IPA squirting bottle ready for washing the sample after etching. (4) Connect the nitrogen and adjust the flow (~ 3 psi) to get a good volume for the blowing out solution. (5) Place the sample into the spraying out solution. Watch the sample until see it gets transparent. Sometimes the thickness of the sample is not the same over the window area, and usually a wedge. Wait until the whole window area is etched. (6) Once the etching stops, wash the sample immediately with IPA a few times and dry with nitrogen. The sample before and after etching is shown in FIG D. 3.

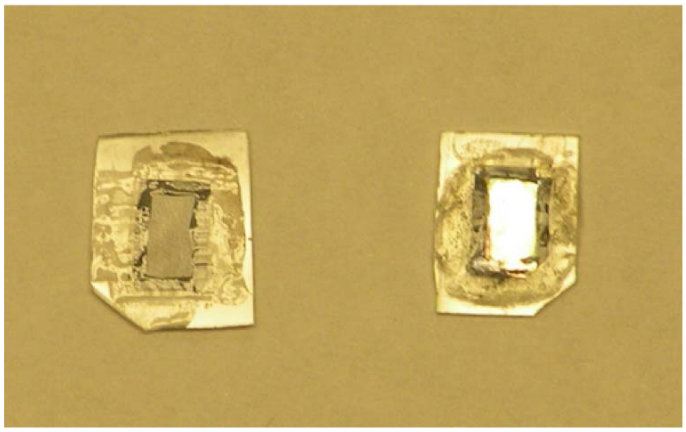

FIG D.3 Sample before etching (left) and after etching (right). The sample is transparent with yellowish color after etching.

E. Principle of MOKE

The MOKE is macroscopically the interaction of electrical magnetic field with electrons in the solid. The Kerr effect is related to the off-diagonal elements in the dielectric tensor. The Zak's method represents the medium boundary and the medium propagation in matrices, and the magneto optic coefficients are also given by means of

the matrices. At each boundary, one medium boundary matrix is used, basically satisfying the Snell's law. For s and p polarization the magneto optic coefficients satisfy linear inhomogeneous equations. The method is a universal method, for which the same type of medium boundary matrix is applicable to all types of boundary: magnetic/magnetic, magnetic/non-magnetic, or non-magnetic/non-magnetic.

E.1 Two media

First thing to define is the medium boundary matrix using the case of two mediums only (FIG E.1). The boundary conditions are basically the conservation of the

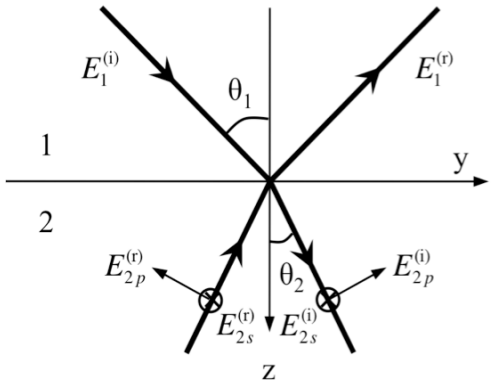

FIG E.1 Definition of *P*, illustration in the two media one boundary system. Waves going in the positive *z*-direction are denoted by $E^{(i)}$, and those going in the negative *z*-direction are denoted by $E^{(r)}$. θ_1 and θ_2 are the angles in Snell's law.

electric and magnetic fields in tangential directions (E_x, E_y, H_x, H_y), and the *xy*-plane is the boundary plane. The following two sets of fields are connected by the medium boundary matrix *A* by $F = AP$.

$$F = \begin{pmatrix} E_x \\ E_y \\ H_x \\ H_y \end{pmatrix}, \qquad P = \begin{pmatrix} E_s^{(i)} \\ E_p^{(i)} \\ E_s^{(r)} \\ E_p^{(r)} \end{pmatrix}$$

where *s* and *p* denote the perpendicular and the parallel (to the plane of incidence) components of the electric field, *i* and *r* denote the incident and reflected wave, respectively. *F* is consisted of fields that matter for boundary conditions and *P* is consisted of fields that are directly related to magneto optic effects and interface transmission and reflection; F is in the coodinate whose z direction is perpendicular the the boundary plane and P is in the local coordinate whose z direction is the light propagation direction (different for different medium). The magneto-optic effect enters into the expression because for the magnetic medium, *D*-vector has the relation with *E* by: $D_j = \sum_{j'} \varepsilon_{jj'} E_{j'}$, and the dielectric tensor has non-zero off-diagonal component (for longitudinal case):

$$\varepsilon_{jj'} = N^2 \begin{pmatrix} 1 & 0 & -iQ \\ 0 & 1 & 0 \\ iQ & 0 & 1 \end{pmatrix}$$

The derivation of matrix A for the magnetic medium is in Ref. [1], and here we just use the result for the longitudinal case:

$$A^{(\mathrm{LON})} = \begin{pmatrix} 1 & 0 & 1 & 0 \\ -\frac{i}{2}\frac{\alpha_y}{\alpha_z}\left(1+\alpha_z^2\right)Q & \alpha_z & \frac{i}{2}\frac{\alpha_y}{\alpha_z}\left(1+\alpha_z^2\right)Q & -\alpha_z \\ \frac{i}{2}\alpha_y QN & -N & \frac{i}{2}\alpha_y QN & -N \\ \alpha_z N & \frac{i}{2}\frac{\alpha_y}{\alpha_z}QN & -\alpha_z N & -\frac{i}{2}\frac{\alpha_y}{\alpha_z}QN \end{pmatrix},$$

where $\alpha_z = \cos\theta$ and $\alpha_y = \sin\theta$, N is the index of refraction. And for non-magnetic medium, the matrix is the same except for $Q = 0$.

The boundary conditions are expressed in this notation as $F_1 = F_2$ or $A_1P_1 = A_2P_2$ at the boundary of medium 1 and medium 2. For the p-polarized initial wave ($E_{1s}^{(\mathrm{i})} = 0$),

$$A_1\begin{pmatrix} 0 \\ 1 \\ r_{sp} \\ r_{pp} \end{pmatrix} = A_2\begin{pmatrix} t_{sp} \\ t_{pp} \\ 0 \\ 0 \end{pmatrix},$$

where the definition of the magento-optic coefficients are $r_{pp} = \frac{E_{1p}^{(\mathrm{r})}}{E_{1p}^{(\mathrm{i})}}$, $r_{sp} = \frac{E_{1s}^{(\mathrm{r})}}{E_{1p}^{(\mathrm{i})}}$, $t_{sp} = \frac{E_{2s}^{(\mathrm{i})}}{E_{1p}^{(\mathrm{i})}}$, $t_{pp} = \frac{E_{2p}^{(\mathrm{i})}}{E_{1p}^{(\mathrm{i})}}$. By solving the set of linear equations given by Eq. A., these coefficients are determined.

E.2 Multifilm systems

The boundary conditions are the same as the above two medium case, and we also need to consider the propagation of the electric magnetic wave, which is represented by the medium propagation matrix $\bar{D}$. The matrix $\bar{D}$ is defined in the way so that

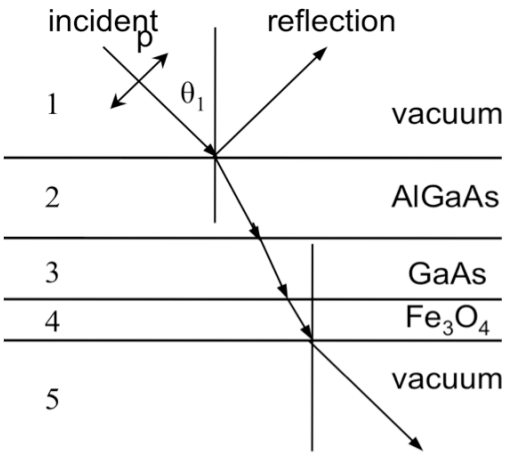

FIG E.2 Schematic structure of the multifilm sample and the geometry of the measurement. The θ's in the films are determined by Snell's law.

$P(0) = \bar{D}P(d)$, where d is the thickness of the film. $\bar{D}$ in the longitudinal case is derived in Ref. [1] as

$$\bar{D} = \begin{pmatrix} U\cos\sigma & U\sin\sigma & 0 & 0 \\ -U\sin\sigma & U\cos\sigma & 0 & 0 \\ 0 & 0 & U^{-1}\cos\sigma & -U^{-1}\sin\sigma \\ 0 & 0 & U^{-1}\sin\sigma & U^{-1}\cos\sigma \end{pmatrix}$$

where $U = \exp\left[-i(2\pi/\lambda)N\alpha_z d\right]$, $\sigma = (\pi/\lambda)NQd\alpha_y/\alpha_z$, and λ is the wavelength. By matching boundary conditions, we can get

$$A_1P_1 = A_2P_2(0) = A_2\bar{D}_2P_2(d_2) = A_2\bar{D}_2A_2^{-1}A_2P_2(d_2)$$

$$= A_2\bar{D}_2A_2^{-1}A_3P_3(d_2) = A_2\bar{D}_2A_2^{-1}A_3\bar{D}_3P_3(d_2+d_3) = \ldots$$

$$= \prod_{j=2}^{4} A_j\bar{D}_jA_j^{-1}A_5P_5(d_2+d_3+d_4)$$

j denotes one film in the multifilm system, and d_j is the thickness of that film (FIG E.2). From 1 to 5, the media are vacuum, AlGaAs (d_2 = 400 nm), GaAs (d_1 = 123nm), Fe_3O_4 (d_3 = 0 ~ 10 nm) and vacuum. For the longitudinal MOKE, we have

$$A_1\begin{pmatrix}0\\1\\r_{sp}\\r_{pp}\end{pmatrix}=\prod_{j=2}^{4}A_j\bar{D}_jA_j^{-1}A_5\begin{pmatrix}t_{sp}\\t_{pp}\\0\\0\end{pmatrix}.$$

Define $A_1^{-1}\prod_{j=2}^{4}A_j\bar{D}_jA_j^{-1}A_5\equiv M$, then the magneto-optic coefficients could be calculated from the elements of matrix M. Briefly, M is a 4×4 matrix, and can be written in 2×2 block matrices

$$M=\begin{pmatrix}G & H\\ I & J\end{pmatrix}.\ \text{And}\ \begin{pmatrix}t_{ss} & t_{sp}\\ t_{ps} & t_{pp}\end{pmatrix}=G^{-1},\ \begin{pmatrix}r_{ss} & r_{sp}\\ r_{ps} & r_{pp}\end{pmatrix}=IG^{-1},$$

Kerr rotation $\phi_p=\frac{r_{sp}}{r_{pp}}=-\phi_p'+\mathrm{i}\phi_p''$, and ϕ' and ϕ'' are the rotations and the ellipticities, respectively. So the calculation is mostly the calculation of matrix M. The calculation of M, and Kerr rotation ϕ' as a function of Fe_3O_4 thickness (d_4) is done in Mathematica for the longitudinal MOKE with initial polarization of only p component. The parameters we use are the following: $Q_1 = Q_2 = Q_3 = Q_5 = 0$, $Q_4 = 0.01$, $N_1 = N_5 = 1$, N_2 =3.45, N_3 =3.65, N_4 =2.5, $\theta_1 = \theta_5 = 45°$, $\sin 45° = N_2\sin\theta_2 = N_3\sin\theta_3 = N_4\sin\theta_4$, d_2 = 400 nm, d_3 = 123 nm, d_4 is the variable. The result is plotted in FIG E.3. In the range of 0 to 20 nm, the Kerr rotation scales linearly with the Fe_3O_4 thickness, has no sign change with thickness (FIG E.3a). In a large range of 0 to 1000 nm, we can see that there are interference peaks with

negative value appearing at every ~160 nm (FIG E.3b). The value for Q_4 is not the real

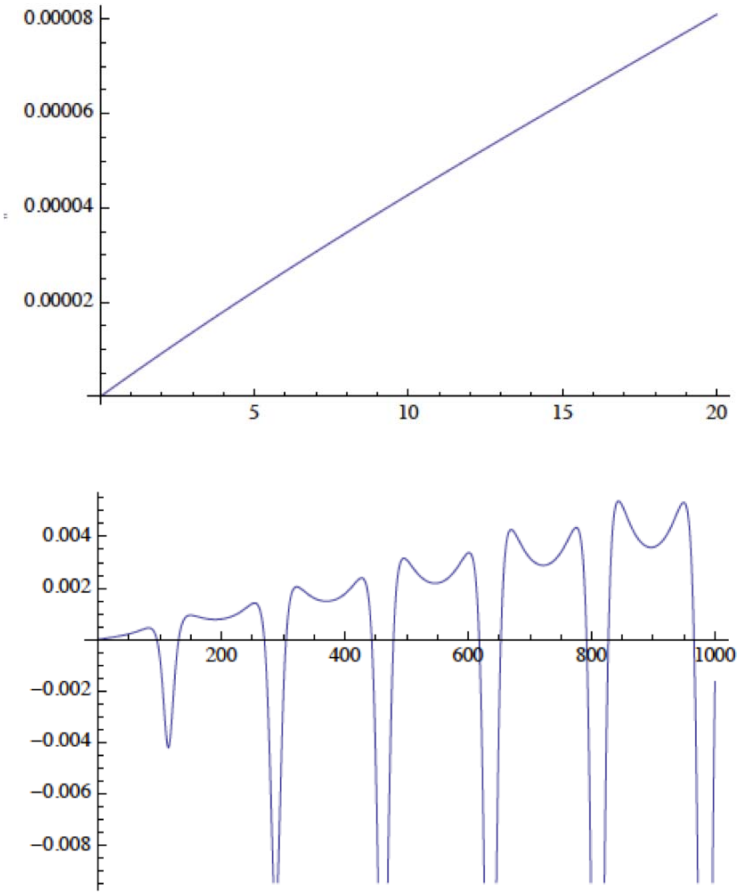

FIG E.3 Kerr rotation as a function of Fe_3O_4 thickness for Fe_3O_4/GaAs(123 nm)/AlGaAs(400 nm). (a) Thickness range: 0 to 20 nm. (b) Thickness range: 0 to 1000 nm.

value obtained from experiment. If we give $Q_4 = 0.1$, the result is the same, but the Kerr rotation is about 10 times.

Although the thickness of GaAs does not change, we also calculate the result for

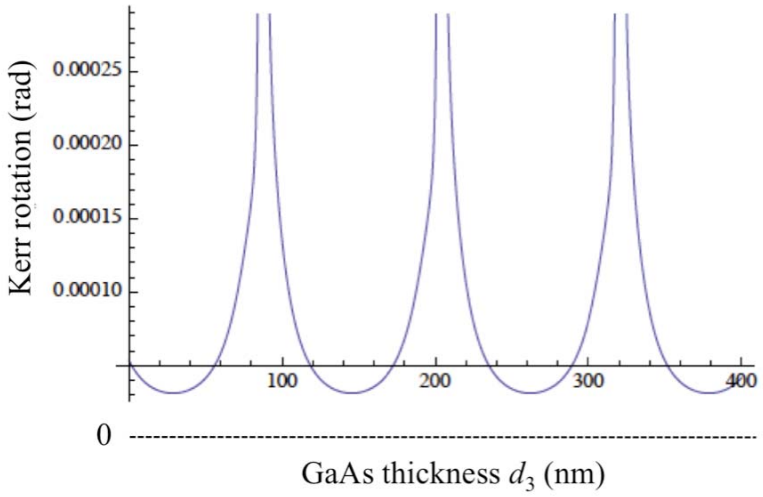

FIG C.4 Kerr rotation as a function of GaAs thickness for Fe_3O_4(10 nm)/GaAs/AlGaAs(400 nm). The dash line indicates the zero Kerr rotation, so there is no sign change. The resonant peaks are at thicknesses where the constructive interference happen in the GaAs layer.

GaAs thickness dependence to see the effect. The thickness of Fe_3O_4 is fixed to d_4 = 10 nm, and d_3 is the variable in this case. The result is plotted in FIG E.4, and the dash line in the figure indicates the zero level. It is clearly seen that the Kerr rotation does not change sign with GaAs thickness. The sharp peaks appear at thicknesses satisfying $N_3 d_3 = (n + 3/4)\lambda$, where the constructive interference happens.

References:

[1] J. Zak *et al.*, J. Magn. Magn. Mater. **89**, 107 (1990).